Ministério da
Ciência e Tecnologia

INPE-15305-TDI/1356

THREE DIMENSIONAL MAGNETOHYDRODYNAMIC SIMULATIONS OF SOLAR BRIGHT POINTS

Jean Carlo Santos

Tese de Doutorado do Curso de Pós-Graduação em Geofísica Espacial, orientada pelos Drs. Maria Virginia Alves e Jörg Büchner, aprovada em 27de fevereiro de 2008

Registro do documento original:
<http://urlib.net/sid.inpe.br/mtc-m17@80/2008/06.16.16.09>

INPE
São José dos Campos
2008

PUBLICADO POR:

Instituto Nacional de Pesquisas Espaciais - INPE
Gabinete do Diretor (GB)
Serviço de Informação e Documentação (SID)
Caixa Postal 515 - CEP 12.245-970
São José dos Campos - SP - Brasil
Tel.:(012) 3945-6911/6923
Fax: (012) 3945-6919
E-mail: pubtc@sid.inpe.br

Ministério da
Ciência e Tecnologia

INPE-15305-TDI/1356

THREE DIMENSIONAL MAGNETOHYDRODYNAMIC SIMULATIONS OF SOLAR BRIGHT POINTS

Jean Carlo Santos

Tese de Doutorado do Curso de Pós-Graduação em Geofísica Espacial, orientada pelos Drs. Maria Virginia Alves e Jörg Büchner, aprovada em 27de fevereiro de 2008

Registro do documento original:
<http://urlib.net/sid.inpe.br/mtc-m17@80/2008/06.16.16.09>

INPE
São José dos Campos
2008

Dados Internacionais de Catalogação na Publicação (CIP)

S59t Santos, Jean Carlo.
Three dimensional magnetohydrodynamic simulations of solar bright points/ Jean Carlo Santos. – São José dos Campos: INPE, 2008.
177p. ; (INPE-15305-TDI/1356)

1. Simulação magneto-hidrodinâmica. 2. Sol. 3. Pontos brilhantes. 4. Aquecimento coronal. 5. Campo magnético. I. Título.

CDU (533.95)

Aprovado (a) pela Banca Examinadora em cumprimento ao requisito exigido para obtenção do Título de Doutor(a) em

Geofísica Espacial

Dr. Delano Gobbi

Presidente / INPE / SJCampos - SP

Dra. Maria Virgínia Alves

Orientador(a) / INPE / SJCampos - SP

Dr. José Augusto Bittencourt

Membro da Banca / INPE / SJCampos - SP

Dra. Inez Staciarini Batista

Membro da Banca / INPE / SJCampos - SP

Dr. Gerson Otto Ludwig

Membro da Banca / INPE / São José dos Campos - SP

Dr. Jorg Buchner

Convidado(a) / Orientador / MAX Planck / Katlenburg-Lindau -

Dr. Artour Elfimov

Convidado(a) / USP / São Paulo - SP

Aluno (a): Jean Carlo Santos

São José dos Campos, 27 de Fevereiro de 2008

ACKNOWLEDGEMENTS

I would like to thank my grandparents (Alfredo Bassaco and Layne P. B. Bassaco) and my mother (Valda A. Bassaco) for helping me to give the first steps toward the present life.

I would like to thank my supervisors Prof. Dr. Jörg Büchner and Prof. Dr. Maria V. Alves for giving me the opportunity to work in such a wonderful topic and believing in my capacity to do this work.

I would like to thank Dr. Antonius Otto and Dr. Bernd Nikutowski for the helpful discussions about the model and for the disponibility to answer my questions and help to solve the problems.

I would like to thank Dr. Brian Welsch and Dr. Hardi Peter for the discussions during conferences and for giving valuable hints about the work with numerical simulations.

I would like to thank the International Max-Planck Research School - IMPRS, in the person of Dr. Dieter Schmitt, for the three years fellowship and for the wonderful environment offered for the PhD students to develop themselves.

I would like to thank my colleagues from the IMPRS and from INPE for the support and for the exciting discussions, about science or about life, that we had during this period.

At last, but not the least, I would like to thank the person that was by my side during the good and bad moments of the last two years (Silvia Protopapa), and that I believe is the second half of my orange, for the love and the attention given during this period.

ABSTRACT

Horizontal and vertical motions of the plasma in the solar photosphere have an important role in the build-up of electric currents in the solar atmosphere. These electric currents could dissipate and heat the corona, generate Extreme-Ultraviolet and X-ray Bright Points or trigger flares. We study the effects of different types of horizontal photospheric plasma motion for the generation of electric currents in the solar atmosphere and the location of these currents. To perform this study we use a 'data driven' three dimensional magnetohydrodynamic model. The model solves an appropriate set of magnetohydrodynamic equations and uses the magnetic field extrapolated from the line-of-sight component of the photospheric magnetic field, observed by the Michelson Doppler Imager (MDI/SOHO), as initial condition. The different types of horizontal photospheric plasma motion, derived from the temporal evolution of the magnetic structures in the photospheric line-of-sight magnetograms, are used as boundary condition of the model.

SIMULAÇÃO MAGNETOHIDRODINÂMICA EM TRÊS DIMENSÕES DE PEQUENAS EXPLOSÕES SOLARES (SOLAR BRIGHT POINTS)

RESUMO

Movimentos horizontais e verticais do plasma na fotosfera têm um papel importante na formação de correntes elétricas na atmosfera do Sol. Essas correntes podem ser dissipadas e aquecer a coroa solar, gerar pequenas explosões solares (bright points) vistas em extremo ultravioleta ou em raios X ou desencadear grandes explosões solares (solar flares). Neste trabalho estudam-se os efeitos de diferentes tipos de movimentos horizontais na fotosfera do Sol na formação de correntes elétricas na atmosfera solar e a localização dessas correntes. Para realizar esse estudo utilizou-se um modelo magnetohidrodinâmico em três dimensões. O modelo resolve um conjunto apropriado de equações magnetohidrodinâmicas e usa o campo magnetico extrapolado a partir do campo magnetico de linha de visada, medido pelo Michelson Doppler Imager (MDI/SOHO) abordo do satélite Solar and Heliospheric Observatory (SOHO), como condição inicial do modelo. Os diferentes tipos de movimento horizontal presentes na fotosfera são determinados a partir da evolução temporal das estruturas magnéticas presentes nas medidas do campo magnético fotosférico. Esses movimentos são inseridos na condição de contorno aplicada na base do volume de simulação.

CONTENTS

Pág.

LIST OF FIGURES

Pág.

LIST OF TABLES

Pág.

1 INTRODUCTION

The object of study of this dissertation is the Sun. More specifically the heating activity of the solar atmosphere which causes an increase in Extreme-UltraViolet (EUV) and X-ray radiation, associated to small scale bipolar magnetic features in the solar photosphere. The 'small scale' heating activity is thought to contribute significantly to the temperature increase in the solar outer atmosphere (solar corona) and to its maintenance during the minimum of solar activity, in the so called quiet Sun. However, the physical mechanisms that connects the observed small scale magnetic features and the solar coronal heating are not fully understood, yet.

This introduction starts with a description of the general properties of the Sun and gradually reaches the specific topic of this dissertation: coronal Bright Points (BPs). The objective of this chapter is to give to the reader a general view at the problem and to summarize what is known and which are the main open questions about this amazing and intriguing subject.

1.1 General properties of the Sun

The Sun is the star at the center of the Solar System. As a star, the Sun has a spectral class of G2V. G2 is because it has a surface temperature of approximately 5,780 K, and V indicates that it is a main sequence star. Compared to the other stars the Sun is not special. For us, however, it is important since its energy, in the form of sunlight, supports almost all life on Earth, and drives the Earth's climate and weather. Also, the proximity to our planet allows to study the phenomena occurring in the solar atmosphere in detail, in order to generalize them to other stars.

The solar energy is produced in the solar core by nuclear fusion through a series of steps called the p–p (proton–proton) chain. This process converts hydrogen into helium and releases energy in the form of electromagnetic radiation. Adjacent to the core, in the radiative zone, the high-energy photons released in the fusion reactions are absorbed by the solar plasma and then re-emitted again in random directions, and at slightly lower energy. In this way, it takes a long time for radiation to reach the Sun's surface. In the outer layer of the Sun, the increase of the opacity of the solar plasma inhibits the energy transport by radiation. This gives rise to temperature gradients. As a result, thermal convection occurs and thermal columns carry hot material to the surface of the Sun. Once the material cools off at the surface, it moves downward again, to receive more heat from the top of the radiative zone. The thermal columns in the convection zone form an imprint on the surface of the Sun in the form of the observable solar granulation and

supergranulation. These three regions (core, radiative zone and convection zone) compose what is called the solar interior.

At the top of the convection zone the opacity of the solar plasma sharply decreases, and energy is again free to propagate by means of electromagnetic radiation. The region where this occurs is called the photosphere, and it is the visible surface of the Sun. The parts of the Sun above the photosphere are referred to as the solar atmosphere. They can be viewed with telescopes operating across the electromagnetic spectrum, from radio through visible light to gamma rays, and comprise five principal zones: the temperature minimum, the chromosphere, the transition region, the corona, and the heliosphere. The coolest layer of the Sun is a temperature minimum region located about 500 km above the photosphere, with a temperature of about 4,000 K. Above the temperature minimum layer is a thin layer about 2,000 km thick, dominated by a spectrum of emission and absorption lines, called the chromosphere. The temperature in the chromosphere increases gradually with altitude, ranging up to around 100,000 K near the top. Above the chromosphere is a transition region in which the temperature rises rapidly from around 100,000 K to coronal temperatures closer to one million K. The corona is the extended outer atmosphere of the Sun, which is much larger in volume than the Sun itself. The corona merges into the solar wind that fills the solar system and heliosphere.

The motion of the conductive plasma in the convection zone gives rise to magnetic fields by means of a dynamo mechanism. The fact that the Sun rotates faster in the equator than near the poles makes the magnetic field wound around the Sun generating long flux rope structures. Due to a plasma instability these flux ropes emerge to the solar surface appearing in the photosphere as large regions of magnetic field concentration, called active regions. Observations show that the coronal activity is associated with active regions, and consequently to regions of strong magnetic field concentration. High spatial resolution observations of the solar photosphere demonstrated that the magnetic field does not appear at the solar surface only in the form of large active regions. The solar surface is covered by small scale bipoles that interact with each other and due to the convective motions in the solar surface accumulate in the intergranular regions. These small scale magnetic bipoles are probably generated by turbulent convection, which can give rise to ”small-scale” dynamos that produce magnetic north and south poles all over the surface of the Sun. The number of active regions visible at the Sun’s surface is not constant, but varies over an 11-year cycle known as the solar cycle. During a typical solar minimum few active regions are visible at the surface of the Sun, appearing usually at high latitudes. As the solar cycle progresses, the number of active regions increases and they move closer to the equator of the Sun. Since the coronal activity is associated with the magnetic field,

the solar corona is more dynamic during the solar maximum than in the solar minimum. However, the small scale magnetic field seems to be anti-correlated to the solar cycle and can have an important role to the maintenance of the coronal activity during the solar cycle minimum.

1.2 Coronal bright points

Coronal BPs are defined as small (30"–40") coronal features of enhanced X-ray and EUV emission. They are part of the small scale range of the solar activity. Coronal BPs, from here after called only BPs, are considered a directly observable phenomena of the solar corona heating and their understanding might provide a key to answer other questions like: what is heating the solar corona? Which is the mechanism that triggers flares and Coronal Mass Ejections (CMEs)? Which is the mechanism responsible for the acceleration of the solar wind?

Nowadays, high spatial and temporal resolution observations of the Sun are available. They can help to characterize and understand the BP phenomenon. However, theory and modeling are a fundamental step to their complete understanding. In the following sections the basic properties and the first qualitative models used to describe the BPs are presented. They represent the first steps of a long journey to the understanding of the solar coronal BPs.

1.2.1 Bright Point properties

X-ray BPs were first observed in rocket X-ray telescope images in 1969 (Vaiana et al., 1970). After that, a series of papers was published describing the statistical properties of X-ray BPs based on the analysis of the photographs from the S-054 X-ray telescope aboard Skylab spacecraft (Golub et al., 1974; Golub et al., 1975; Golub et al., 1976a; Golub et al., 1976b; Golub et al., 1977; Golub et al., 1979). In (Golub et al., 1974), for the first time the general properties of X-ray BPs were described in detail. Figure 1.1 presents a histogram showing the number of bright points versus their lifetimes. The lifetime distribution is fitted by a Poisson distribution with a mean lifetime of 8 hours. It is biased toward longer lifetimes. The investigation of the sizes of X-ray BPs shows that the average maximum diameter a point with a mean lifetime value of 8 hours attains is 20 ± 5 arcsec^2. The lifetimes are proportional to the BP area, with larger BPs living longer, as shown in Figure 1.2. One interesting characteristics of X-ray BPs is that they are not concentrated in belts of activity as the active regions are. Figure 1.3 shows the BP distribution as a function of latitude. The solid curve is a cosine function . It corresponds to the projection of an uniform surface area on the Sun. The curve generally fits the data, with the exception of the active-region

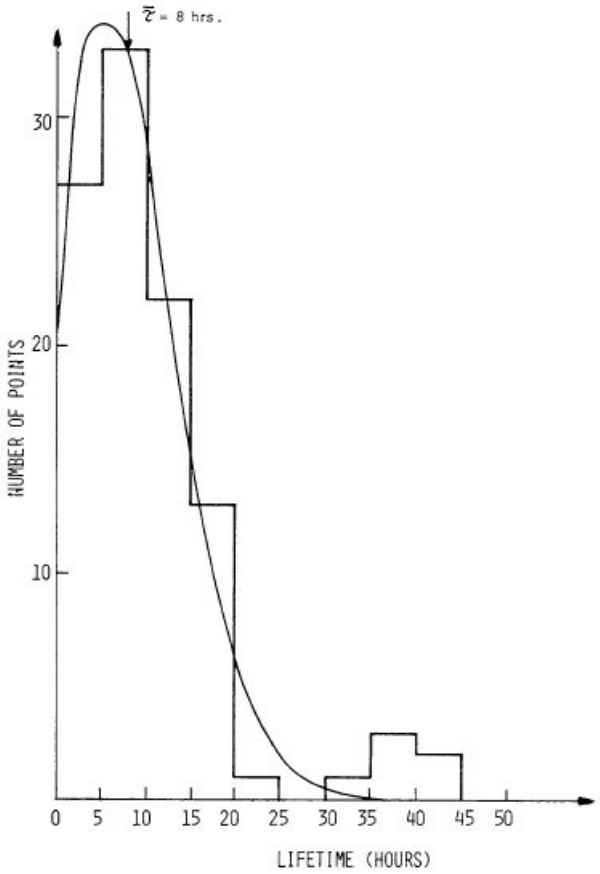

FIGURE 1.1 - Histogram showing number of bright points versus lifetime. (Golub et al., 1974)

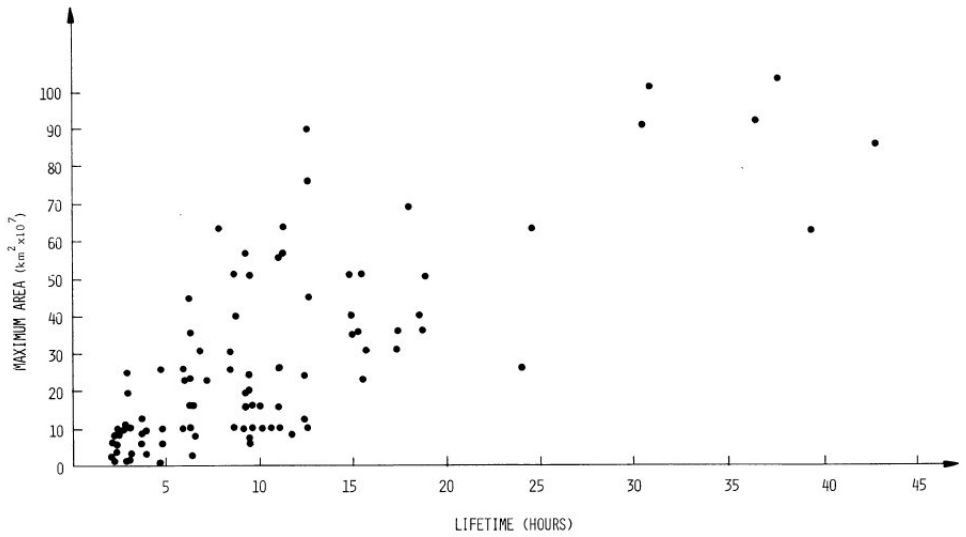

FIGURE 1.2 - Maximum area of a X-ray BP plotted against its lifetime. (Golub et al., 1974)

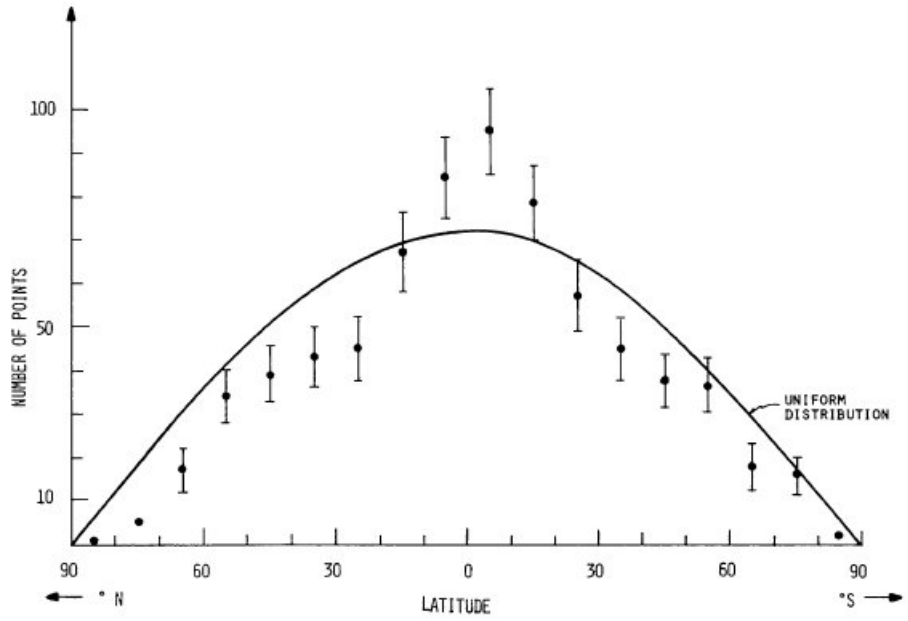

FIGURE 1.3 - Latitude distribution of BPs. (Golub et al., 1974)

latitudes at which BPs cannot be seen because of the brightness of the active region. The total number of BPs at the Sun at any time is at least 200. Approximately 1500 X-ray BPs 'emerge' per day. Estimates of the BP temperature gives $T \approx 1.3 - 1.7 \times 10^6$ K and densities 2-4 times the average coronal density. The Skylab spacecraft observations have shown that BPs present sudden variations in the intensity, characterizing a flaring behavior. Another interesting detail of BPs is that with an estimated average magnetic field of ≈ 10 G and an area of $\approx 10^{18}$ cm^2, the 1500 BPs emerging per day are associated to a flux in the surface of $\approx 10^{22}$ Mx. If the BPs would be caused only by emerging magnetic features they would contribute more to the emergence of magnetic flux than active regions.

(Golub et al., 1975) found that the longitudinal distribution of BPs is not uniform (Figure 1.4). Further examination of the latitudinal distribution of the BPs suggests that it can be interpreted as having two components: a uniformly distributed component and one having a distribution similar to that of active regions, occurring mostly within $\pm 30^o$ of the equator (Figure 1.5). Figure 1.5a shows the latitudinal distribution of the BPs and Figure 1.5b shows the same distribution after subtraction of a uniformly distributed component fit to the high latitude data, shown by the solid line in Figure 1.5a. After the subtraction, the latitudinal distribution shows a clear excess at the active region latitudes. A plot of the longitudinal distribution of BPs for the two different groups of Figure 1.5 makes evident the presence of the two groups also in the longitudinal distribution (Figure 1.6).

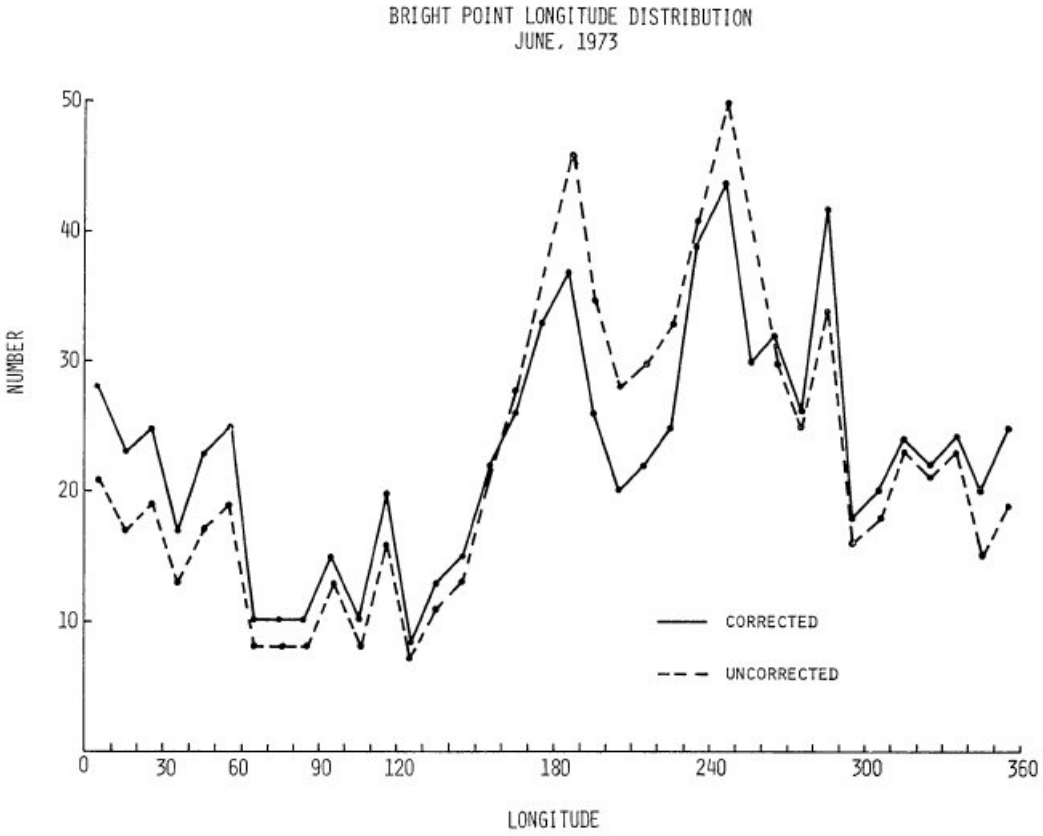

FIGURE 1.4 - Distribution in Carrington longitude of BPs during the period 28 May–19 June 1973. The correction is made for the relative observing time. (Golub et al., 1975)

The longitudinal variation of the BPs at latitudes $> 30^o$ is less than that observed at low latitudes.

(Golub et al., 1976a) described the number of remaining BPs after a time t by the function

$$N(t) = N_S e^{-t/\tau_S} + N_L e^{-t/\tau_L}, \tag{1.1}$$

where N_S is the number of short lived BPs, N_L is the number of long lived BPs, τ_S is the average lifetime of the short lived BPs and τ_L is the average lifetime of the long lived BPs. The first term is associated to a short lifetime component, with average lifetime of 8 hours, and the second term to a long lifetime component, with an average lifetime of 1.5 days. The number of long lived BPs is assumed to be 24% of the total number of BPs in the solar disc at one moment. Figure 1.7 shows a histogram of the number of X-ray BPs on 20 August 1973 having the lifetimes indicated in the abscissa. The solid curve shows a predicted fit using the two-lifetime fit.

The longitudinal distribution of the average number density and the full disk average

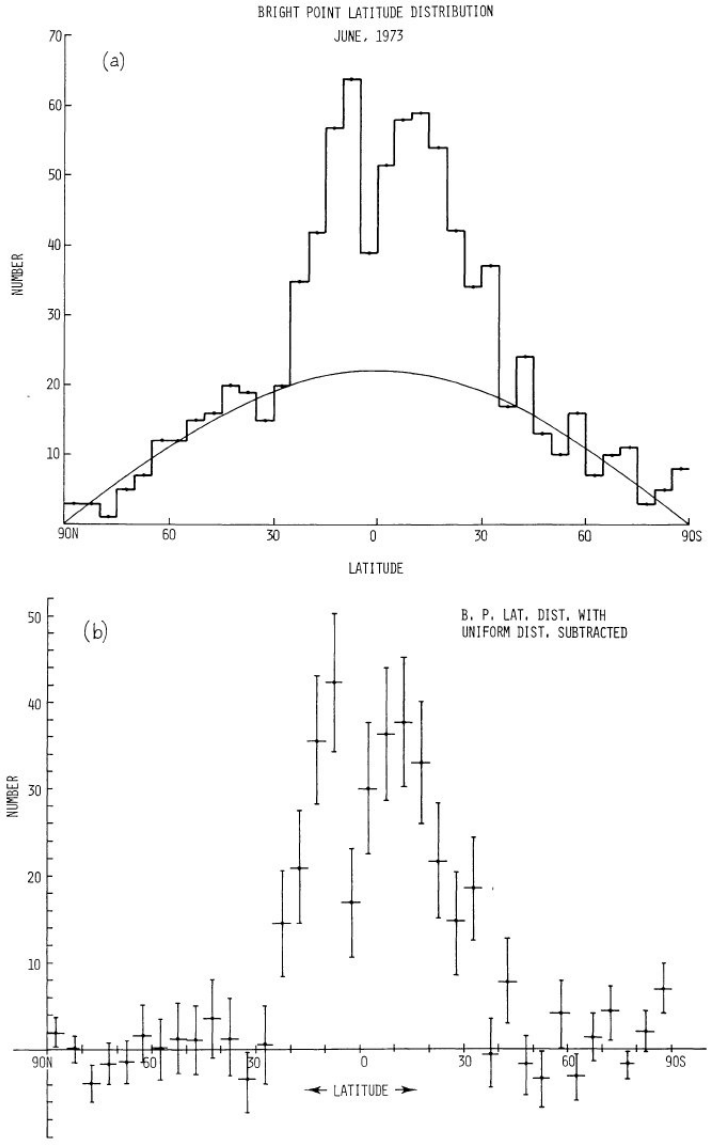

FIGURE 1.5 - Two components nature of the BPs latitudinal distribution. (Golub et al., 1975)

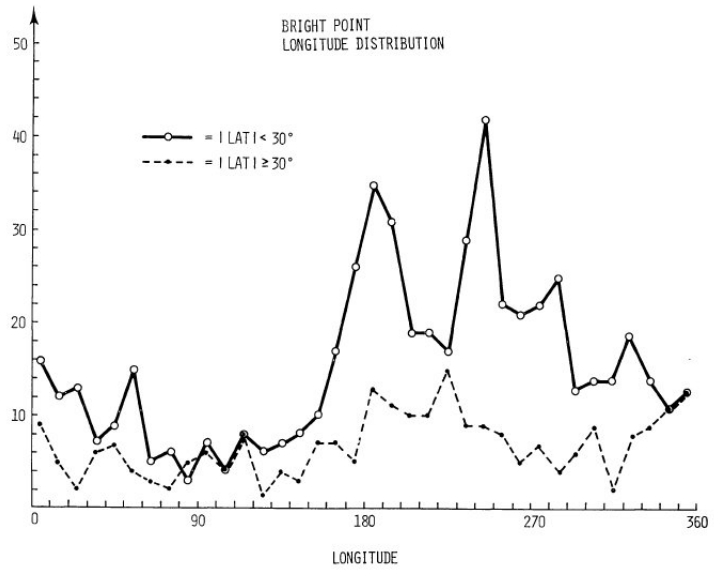

FIGURE 1.6 - Longitudinal distribution of the BPs divided in two categories. (Golub et al., 1975)

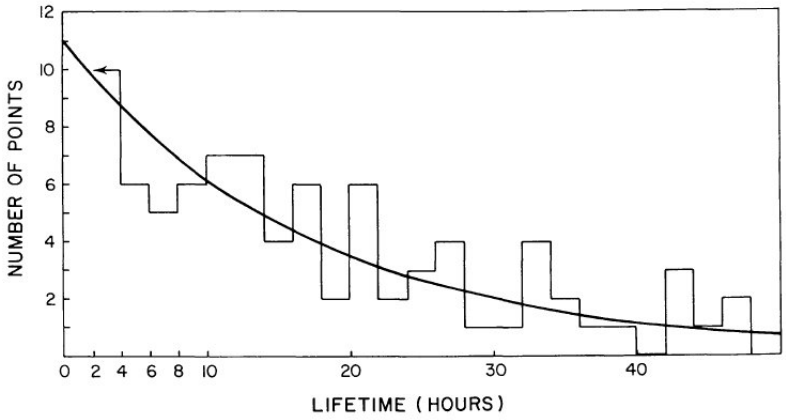

FIGURE 1.7 - Histogram and two-lifetime fit of the BPs observed in 20 August 1973. (Golub et al., 1976a)

number of X-ray BPs from 28 May to 27 November 1973 is examined in (Golub et al., 1976b). Figure 1.8 shows statistically significant variation in the longitude distribution and major variations from one rotation to the next throughout the six-month interval. The average number of observations is given in 20^o longitudinal intervals. The average number of X-ray BPs observed on full disk images is shown in Figure 1.9. This number presents significant and non-random variations. The variations are also visible when high latitude and low latitude BPs are separated and an averaging per rotation is performed (Figure 1.10). The high latitude points show a systematic up and down behavior, with the values changing by a factor of two. The low latitude variation can be explained as change in the uniform component alone, while the AR-like component remains constant to within the statistical uncertainties of the data. The peak of the averaged number of BPs coincided with a major outbreak of activity. In (Golub et al., 1976b) an estimative of the quantity of magnetic flux emerging per day in the form of X-ray BPs produced values ranging between 1.2×10^{22} and 3.6×10^{22} Mx, which correspond more or less to 1–4 times the flux an emerging active region brings to the surface.

The magnetic properties of X-ray BPs were studied in (Krieger et al., 1971; Harvey et al., 1975; Golub et al., 1977). It was found that X-ray BPs are usually associated with bipolar magnetic features. The cases where no bipoles were associated to the BPs were the cases where the BPs were too young or too old, and, probably, the magnetic bipoles were small or faint and could not be resolved in the magnetograms. The bipolar magnetic features have some characteristics that indicate that they might be related to emerging magnetic fluxes: the distance between bipoles is an increasing function of the age of the X-ray BPs and the total magnetic flux contained in the bipole show similar relation. Another characteristic of the bipoles associated to the X-ray BPs is that they present an initial rapid emergence followed by a more gradual dispersal of the magnetic fields, like in the large and long-lived active regions. The characteristic value of total magnetic flux for an X-ray BP is $2 - 3 \times 10^{19}$ Mx and the lifetime of a X-ray BP is proportional to its total magnetic flux, with proportionality constant $\approx 10^{20}$ Mx day^{-1}.

The relation of the numbers of X-ray BPs and the solar cycle is presented in (Golub et al., 1979). Using soft X-ray observations of the solar corona over the period 1970–1978 they show that the number of X-ray BPs varies inversely with the sunspot index. Figure 1.11 shows the number of sunspots and the X-ray BP count normalized to maximum value of 100, as functions of time for the sunspot cycle 20. It is apparent from the figure that the variation in X-ray BP count is close to 180^o out of phase with the sunspot number. This indicates that the X-ray BPs are independent of the larger active regions. If they would be associated with the emergence of the large active regions, then their number

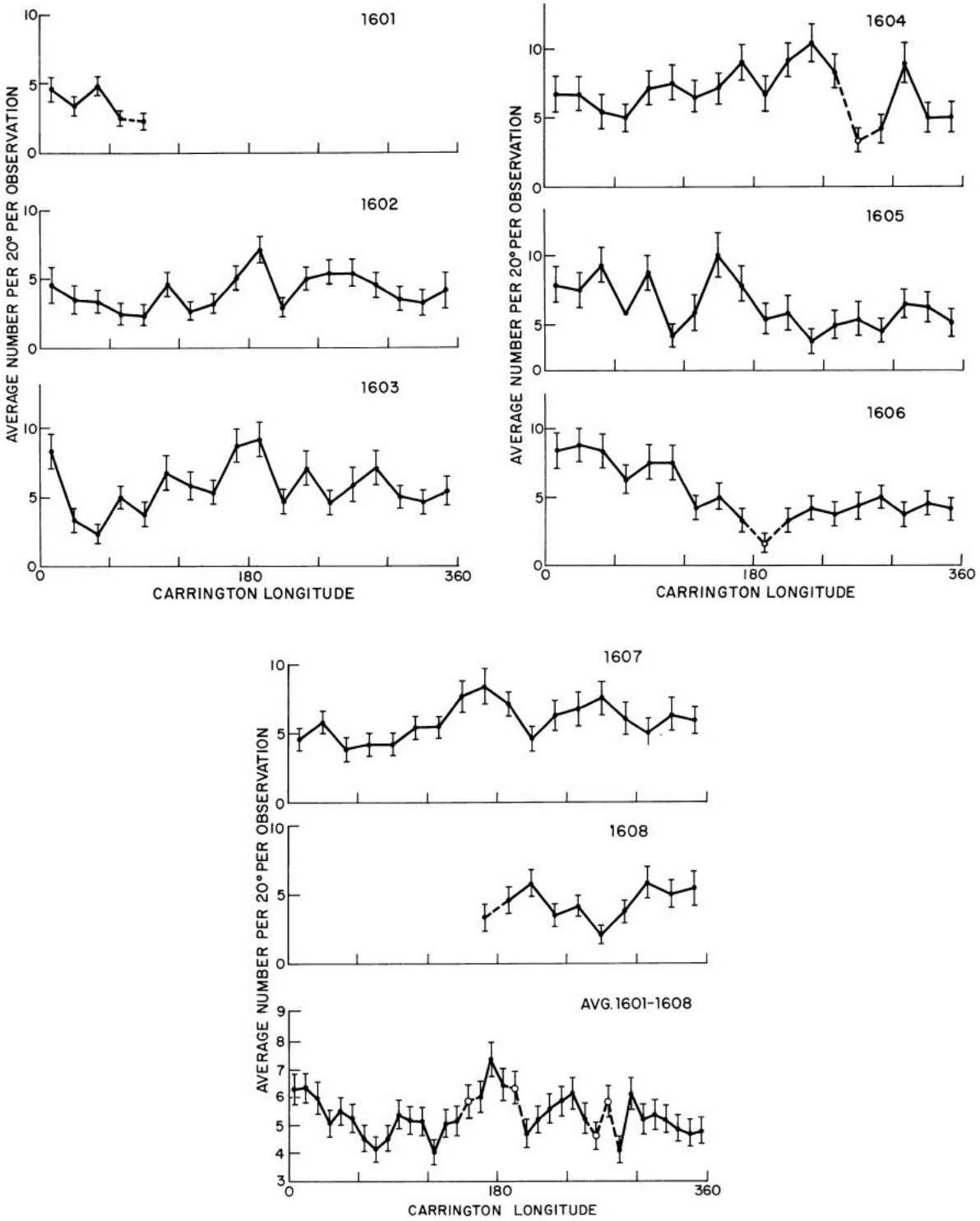

FIGURE 1.8 - Average number density of X-ray BPs as a function of longitude for Carrington rotations 1601–1608. (Golub et al., 1976b)

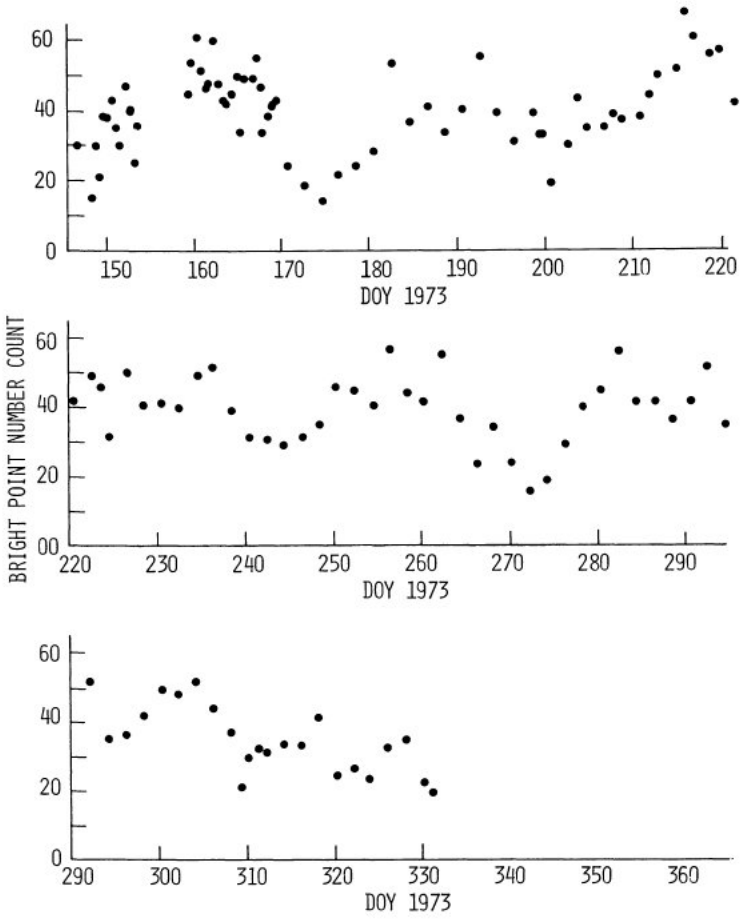

FIGURE 1.9 - Average number of X-ray BPs observed on full disk images from 28 May to 27 November, 1973. (Golub et al., 1976b)

could not lead or lag the sunspot number by much more than the characteristic lifetimes of the flux associated with the active regions ($\approx$ 6 months). The plot of the X-ray BP counts as a function of sunspot number (Figure 1.12) makes the inverse relation between the two more clear. The solid line shows a least-square fit of the form $R_z = AN_x^b$, with $A = (1.1 \pm 0.4) \times 10^4$ and $b = (-1.54 \pm 0.12)$. The relation between solar cycle and X-ray BP number is extended to solar cycle 21 in (Davis, 1983). Additional data obtained by rocket flights in 1979 and 1981 confirm the anticorrelation between sunspot number and the X-ray BP number. Figure 1.13 shows both sets of measurements after they have been normalized to their greatest values. Two interesting explanations for the anticorrelation between the X-ray BPs and the solar cycle are given in (Yoshimura, 1983) and (Schuessler, 1980). Both models assume that BPs are associated to small scale flux ropes that derive from main flux tubes generated deeper in the convection zone. In (Yoshimura, 1983) the depth of the roots of the flux ropes that generate sunspots and X-ray BPs are supposed to change with the solar cycle. At the beginning and during the maximum phase of the cycle

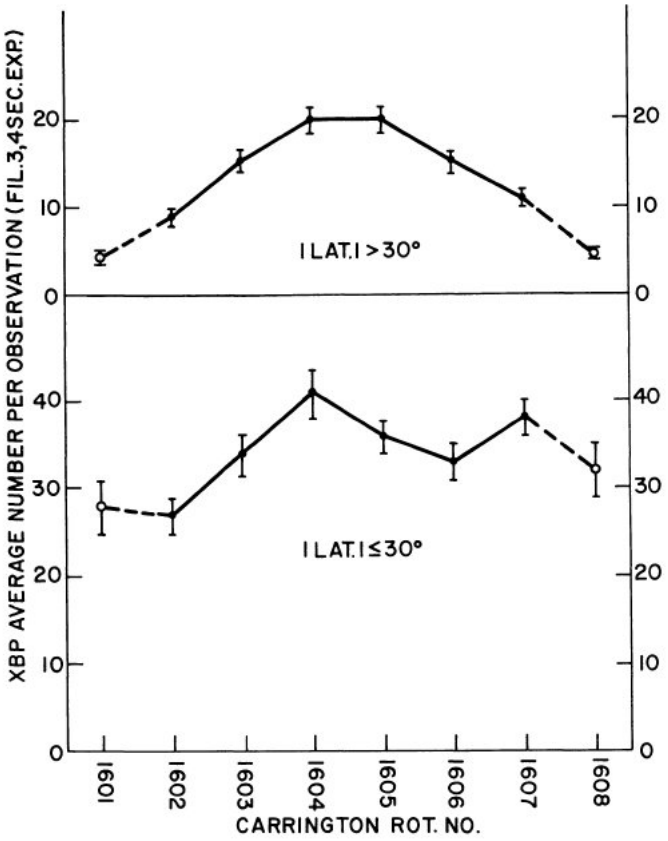

FIGURE 1.10 - Average number of X-ray BPs when high latitude and low latitude BPs are separated and an average per Carrington rotation is performed. (Golub et al., 1976b)

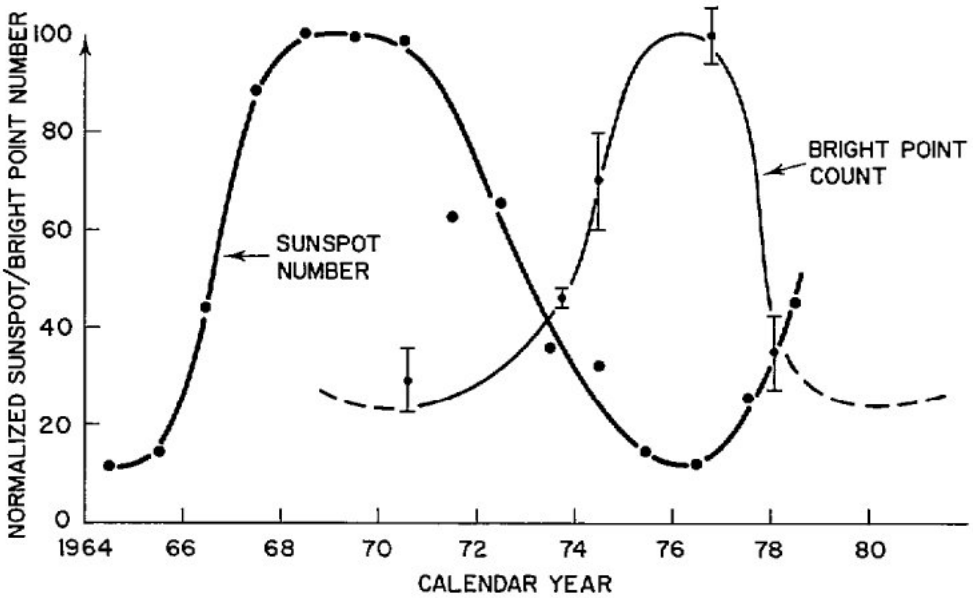

FIGURE 1.11 - Variation of the number of X-ray BPs with the solar cycle. (Golub et al., 1979)

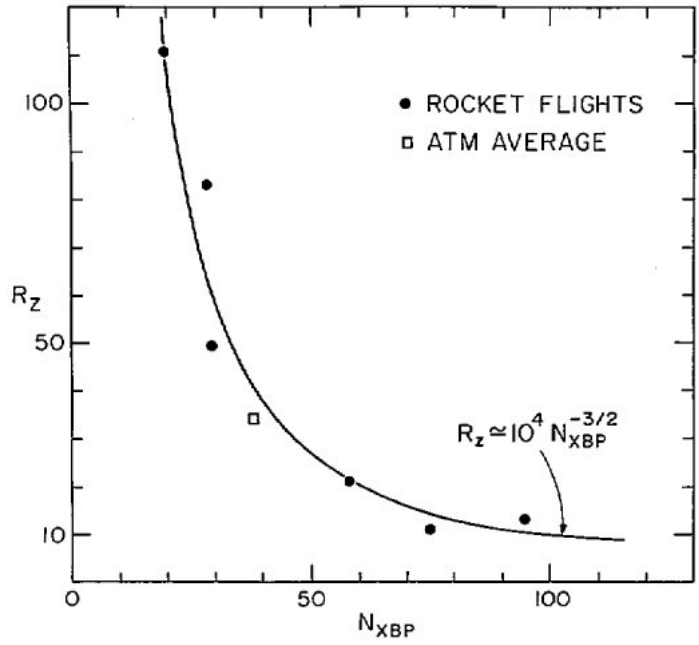

FIGURE 1.12 - Plot of Zurich relative sunspot number R_Z versus corrected X-ray BP number. (Golub et al., 1979)

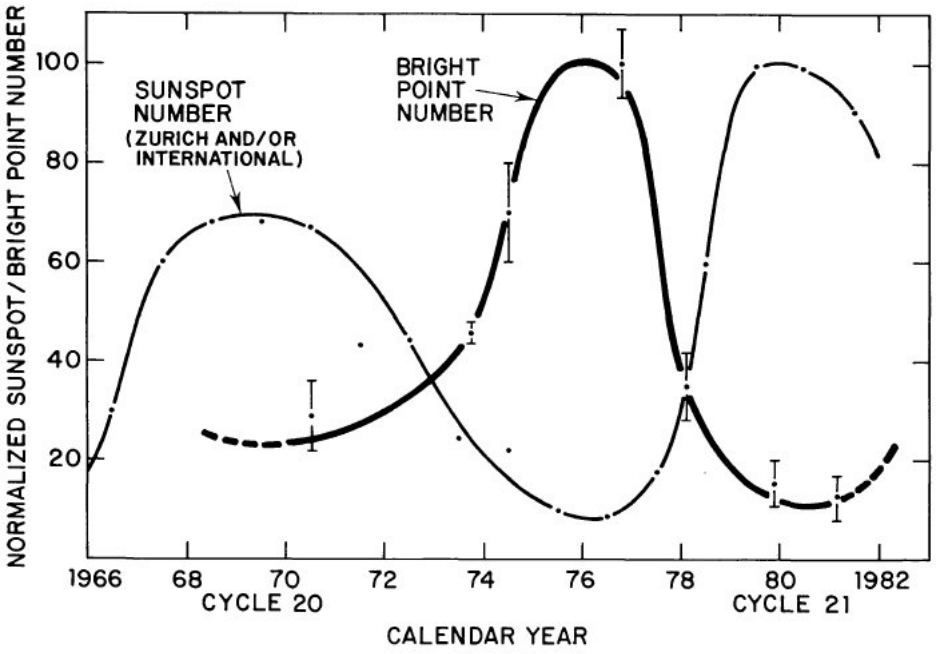

FIGURE 1.13 - Variation of the number of X-ray BPs over sunspot cycles 20 and 21. (Davis, 1983)

the main flux tubes are locate deep in the convection zone, what makes difficult for small scale flux ropes to appear on the solar surface. At the end and during the minimum phases of the solar cycle the main flux tubes are concentrated in shallow layers in the convection zone and relatively small scale flux ropes can erupt on the surface giving rise to BPs. In (Schuessler, 1980) the field generating regions are at a fixed layer near the base of the convection zone. After being generated, magnetic field flux tubes become unstable and erupt leaving the generating regions. When the field is strong in the generating regions the ropes reach the surface faster, giving rise to darker sunspots. Weaker fields take longer to reach the surface and in their path they become shredded to be the BPs. Thus the solar cycle is associated to a variation of the poloidal field strength, which gives rise to the toroidal component on the base of the convection zone.

The detailed evolution of the fine structure of individual BPs was studied in (Sheeley JR.; Golub, 1979). They used a sequence of high-quality NRL Skylab/ATM spectroheliograms obtained during a 1.5-days interval on January 19-20, 1974. The spatial resolution of the measurements was 2 arcsec and the time resolution varied from 30 seconds to 3 hours. In the observations, a BP is resolved into a emission pattern which consists of 2 or 3 miniature loops. The individual loops evolved at a time scale of approximately 6 minutes. The observed lifetime of the individual loops was comparable to the cooling time for the plasma.

Radio emissions and absorptions in the HeI λ10830 line were detected in the quiet Sun and suggested as being related to coronal BPs (Harvey, 1985; Habbal; Harvey, 1988; Marsh et al., 1980). The investigation of the temporal evolution of the magnetic features associated to the absorptions in HeI showed for the first time that BPs could be associated to 'casual' encounters of opposite magnetic polarities in the solar photosphere. The approaching of the magnetic features associated to BPs was observed by (Webb et al., 1993) when comparing X-ray observations made during rocket flights with BBSO and NSO photospheric magnetograms. Later studies (Harvey et al., 1994) have shown that the motion of magnetic features associated to X-ray BPs can be much more complicated than imagined before (emerging, canceling and static magnetic features).

Figure 1.14 shows a histogram of the number of X-ray BPs with a given lifetime for 518 BPs detected using the Soft X-ray Telescope (SXT) onboard Yohkoh satellite (Harvey et al., 1993). The measurements revealed an increase in the average lifetime of BPs from 8 hours to 12 hours.

A comparison between BPs in a coronal hole and a quiet sun region was performed by (Habbal et al., 1990). Their main conclusion is that the similarity of the morphological

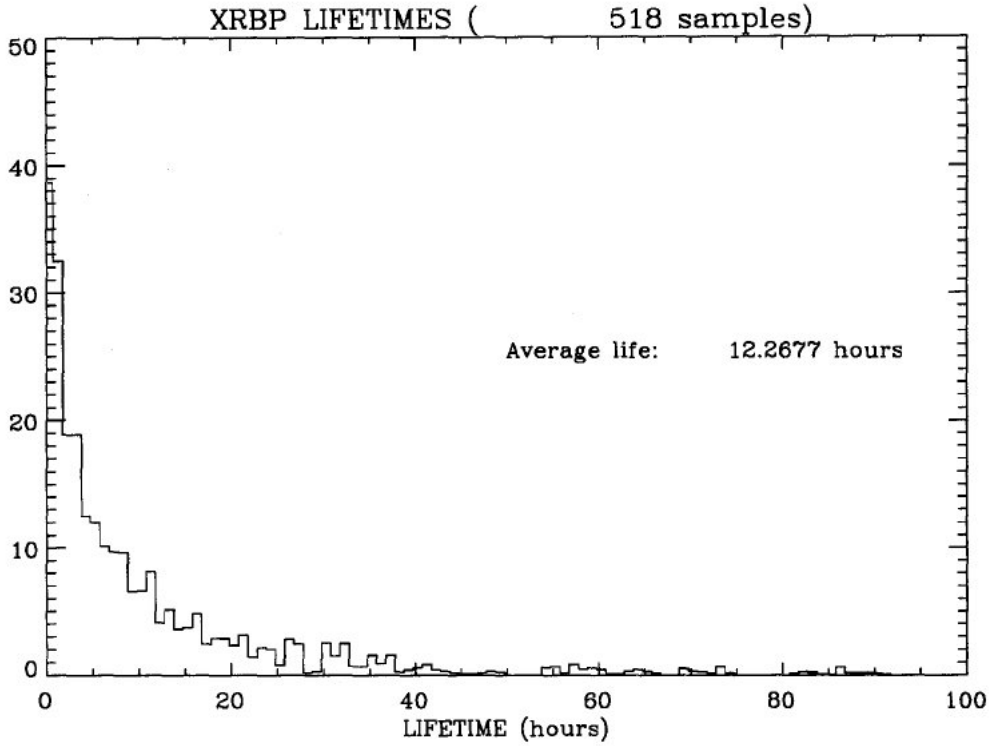

FIGURE 1.14 - Histogram showing the number of X-ray BPs with a given lifetime. (Harvey et al., 1993)

structure of BPs and the temporal variability of their emission in a coronal hole and a quiet region suggest that their distinctive properties are independent of the structure of the overlying large-scale magnetic field. They suggest that the dynamic nature of the emission from BPs is strictly determined by the properties of the small-scale magnetic field, particular its strength and complexity, rather than the large-scale magnetic field features.

1.2.2 Bright Point models

Most of the models developed to explain the observational features associated with BPs consider the magnetic interaction of moving bipolar magnetic features with the surrounding magnetic field. Since BPs were first thought to be associated with emerging or canceling magnetic features, the first models considered only these two pattern of motion to try to explain the observed features. However, as it is now known magnetic features associated with BPs present patterns of motion that are much more complex. This should be considered in future models. Also, since the observed features of BPs seem to be independent of the background magnetic field, future models should be able to reproduce BPs considering the small scale magnetic field changes associated to the moving photospheric features.

In the following sections the early models developed considering flux emergence and cancelation are described. They constitute suggestions of mechanisms that can be responsible for the occurrence of BPs.

1.2.2.1 Emerging magnetic features

Bright points were at first thought to be associated only with emerging magnetic features (Krieger et al., 1971; Harvey et al., 1975; Golub et al., 1977). For this reason, the first models that were developed to explain their occurrence used the scenario of an emerging bipolar magnetic feature interacting with the ambient magnetic field.

(Tur; Priest, 1976) developed a two-dimensional model for the formation of current sheets during the emergence of new magnetic flux from below the photosphere. In this model the free magnetic energy associated with the magnetic field configuration containing a current sheet is assumed to power the BP. The authors considered two different configurations for the ambient field. In the first configuration the ambient field is bipolar, represented by a dipole with moment D_A and located at $x = a$, and interacts with a bipole of smaller moment D, which is emerging and located at $x = -a$ (Figure 1.15). Figure 1.15a shows the initial configuration of the magnetic field. The initial moment of the emerging bipole is $D = D_0$ and the magnetic field is potential and given by

$$B_0(z) \equiv B_{0x} - iB_{0y} = D_0(z + a)^{-2} + D_A(z - a)^{-2}, \tag{1.2}$$

where $z = x + iy$. In this configuration initially there are no current sheets and the interaction of the magnetic field of the two bipoles give rise to a null point at the position z_N. The emergence of a small bipolar region is simulated by increasing the moment of the smaller dipole, while its position is kept fixed. The additional flux that emerged presses up against the existing field and gives origin to a current sheet extending from z_1 to z_2 (Figure 1.15b). The free energy available in the system is associated to the current sheet. Figure 1.16 shows how the stored magnetic energy (W_S), relative to the mutual energy of the dipoles W_{12}, varies as the moment of the smaller dipole increases. In the second configuration the background field is a uniform horizontal field. The emergent dipole starts with a moment D_0 and the initial magnetic field is potential and given by

$$B_0(z) \equiv B_{0x} - iB_{0y} = b + D_0 z^{-2}, \tag{1.3}$$

where $\vec{b} = (b, 0, 0)$ is the ambient horizontal field. When the moment of the dipole increases a current sheet forms as the magnetic field of the dipole presses up against the ambient field (Figure 1.17). The variation of the stored magnetic energy (W_s), relative to the mutual

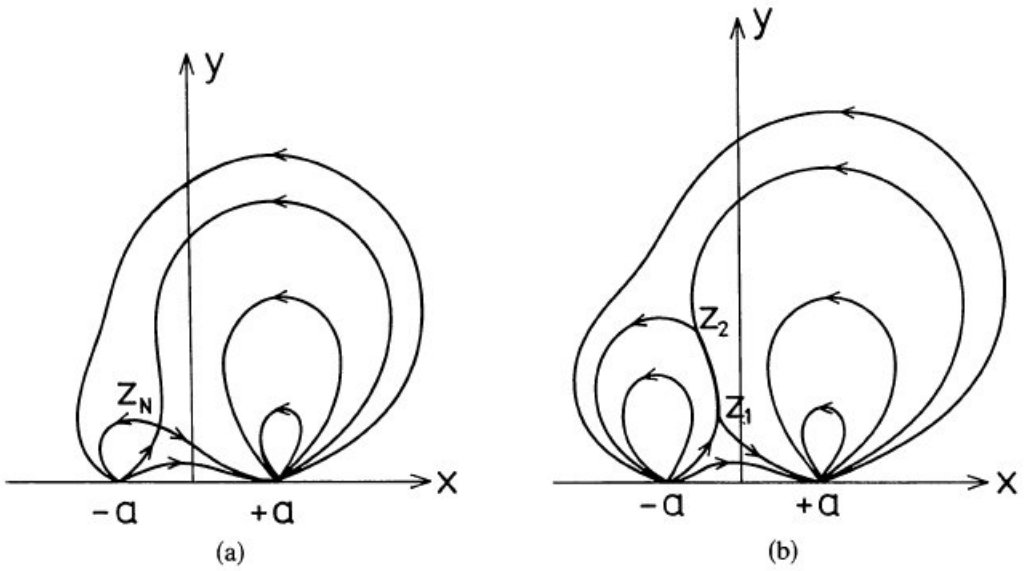

FIGURE 1.15 - Magnetic field configuration for the interaction of two bipoles. (Tur; Priest, 1976)

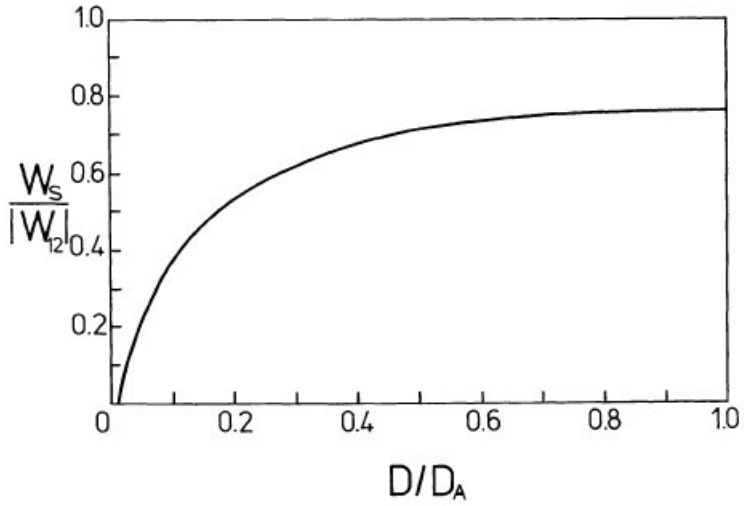

FIGURE 1.16 - Free magnetic energy as a function of the ratio between the moments of the two dipoles. (Tur; Priest, 1976)

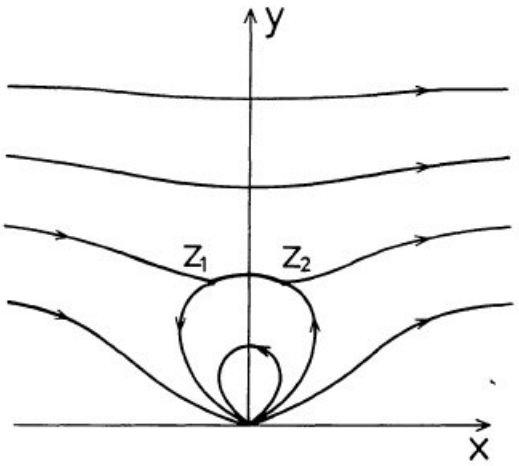

FIGURE 1.17 - Schematic representation of the magnetic field due to a dipole emerging into a uniform horizontal magnetic field. (Tur; Priest, 1976)

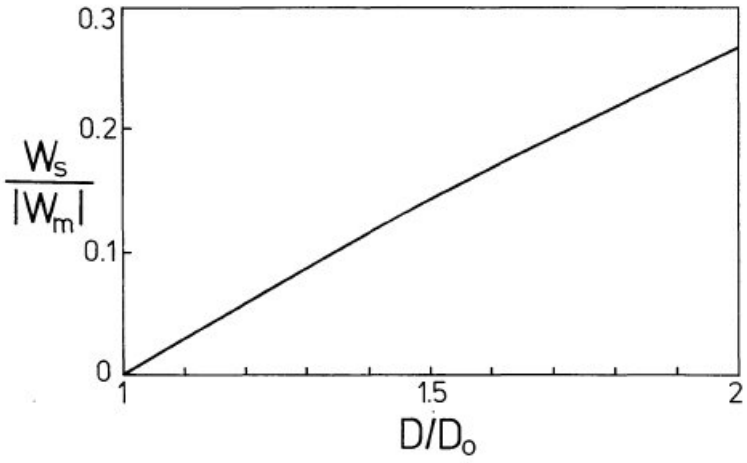

FIGURE 1.18 - Stored magnetic energy (W_s) for a dipole of moment D emerging into a uniform field. (Tur; Priest, 1976)

energy between the dipole and the uniform background field, is shown in Figure 1.18 as a function of the dipole strength. In both configurations the current sheet formation is an effective mechanism for energy storage.

1.2.2.2 Canceling magnetic flux

One important discovery was that many times the magnetic features associated with BPs are often not newly emerging, but instead approaching each other and disappearing. This discovery gave rise to a second group of models, that can be called canceling magnetic flux models.

(Priest et al., 1994) early proposed a model of BPs associated to canceling magnetic fragments. In this model the magnetic fragments are initially unconnected and the bright point is created by coronal reconnection in a three phase process: a pre-interaction phase, in which two photospheric fragments are unconnected magnetically and begin to approach one another, until eventually oppositely directed fields from the fragments come into contact at a null point; an interaction phase, in which an X-point forms which rises into the corona; and a cancelation phase, in which a canceling magnetic feature is produced by photospheric reconnection as the fragments come into contact and decrease in strength. Figure 1.19 illustrates the three different phases of the model by means of six cartoons: (i) two oppositely directed magnetic fragments are far apart and unconnected but approach one another; (ii) after some time the fragments become so close that an X-point forms between them in the photosphere; (iii) the field lines from the two fragments interact and reconnect at the X-Point, which rises from the photosphere into the corona; (iv) as the fragments approach, the reconnection continue for many hours; (v) the fragments come into contact and the cancelation phase begins by photospheric reconnection; (vi) the cancelation by photospheric reconnection continues and the fluxes decrease until either the approach of the fragments ceases or one or both fragments have completely canceled. Inside this physical picture, an analytical model of the pre-interaction and interaction phases is developed in (Priest et al., 1994). Figure 1.20 shows the main components of the model in a two dimensional cartesian system, where $y = 0$ represents the photospheric plane. The two magnetic fragments of equal strength, but opposite polarity, are modeled by sources of flux $+f$ and $-f$ located at $x = \pm a$. The dashed lines represent the separatrices, which separate the domain of the magnetic fragments from the domain of a horizontal background field with intensity B_0. The half-width of the pre-interaction channel, a channel that separates the flux from the poles, is given by b. As the poles approach, the channel narrows until eventually when the pole half-separation is d a null point is formed at the origin. If no reconnection occurs, a vertical current sheet will be created stretching up a height h. The magnetic energy then exceeds that of a purely potential field by an amount that can be later released by reconnection to generate the BP. The magnetic field components (B_x, B_y) for a potential configuration are given in compact form by

$$B_y + iB_x = \frac{if/\pi}{z-a} - \frac{if/\pi}{z+a} + iB_0, \tag{1.4}$$

where $z = x + iy$. In (Priest et al., 1994) the energy available for powering the bright point is estimated by the energy stored in excess of the potential in the field that includes a current sheet. This is done by subtracting the energy obtained for a potential solution from that obtained for a solution containing the current sheet. This 'free energy' is given

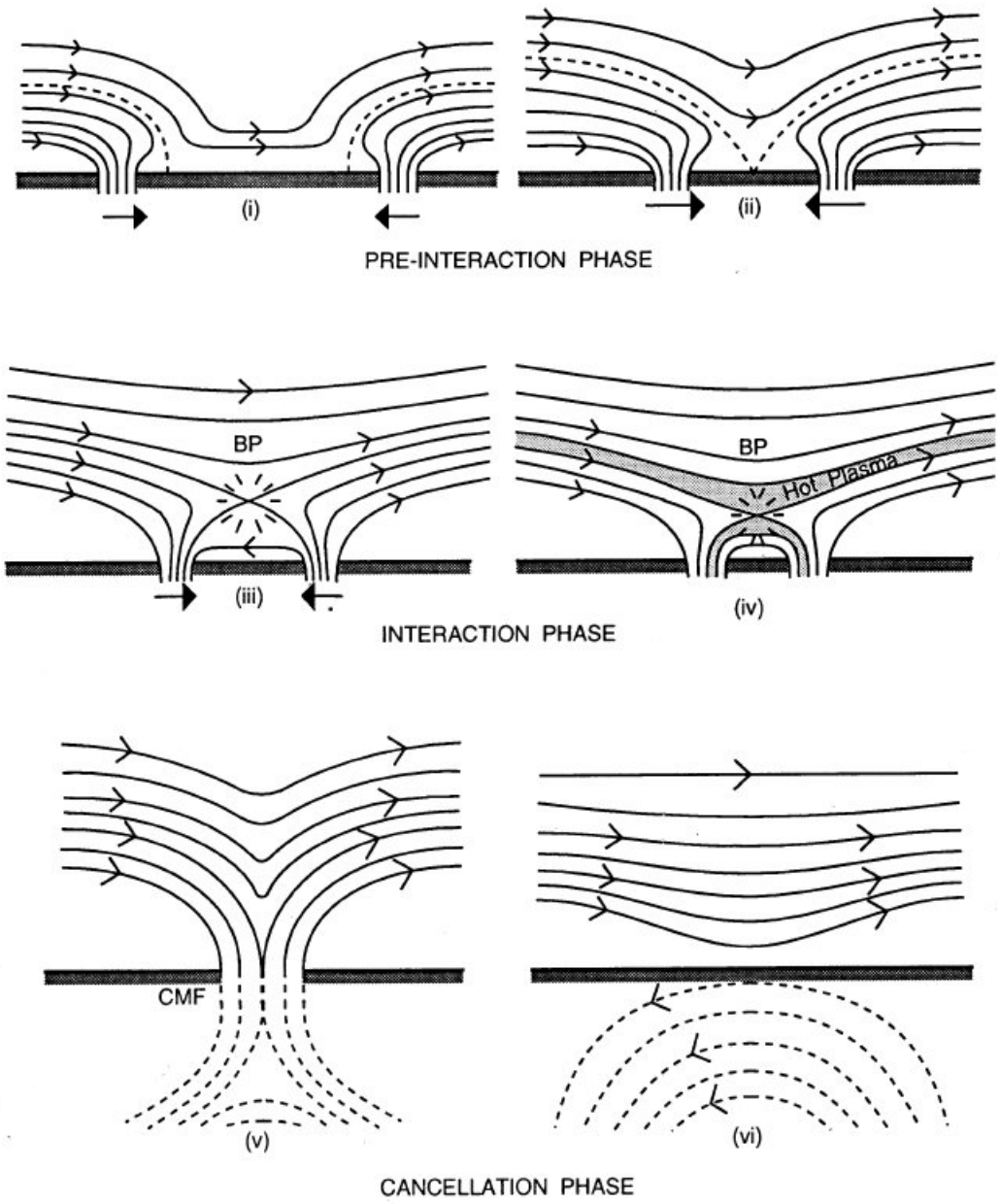

FIGURE 1.19 - Different phases in the approach and interaction of two equal and opposite magnetic field fragments. (Priest et al., 1994)

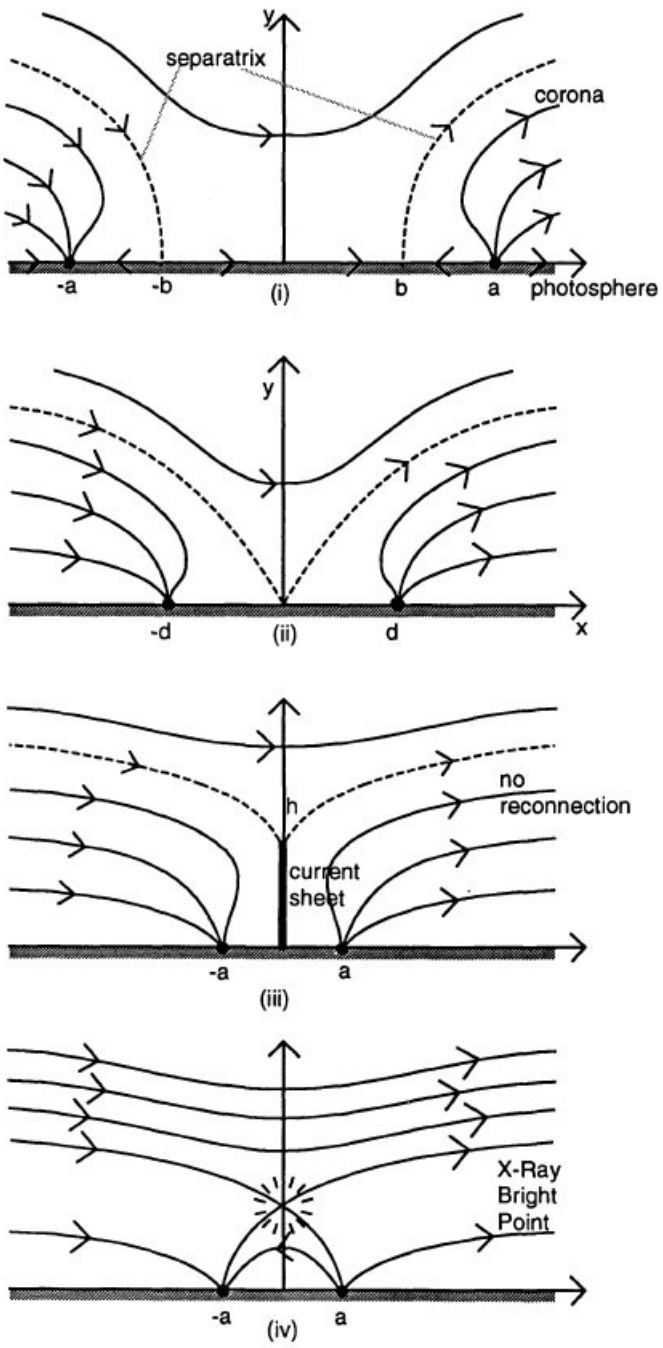

FIGURE 1.20 - Main components of the analytical model for pre-interaction and interaction phases. (Priest et al., 1994)

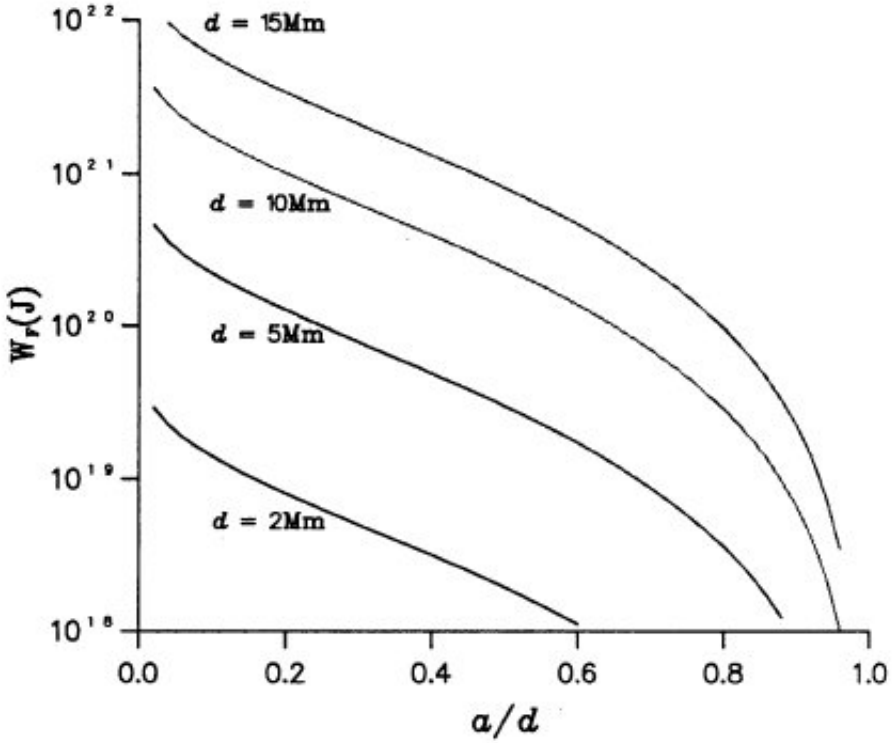

FIGURE 1.21 - Free energy as a function of a/d for different values of the interaction distance. (Priest et al., 1994)

by

$$W_f = \frac{B_0^2 d^3}{2\mu}\Big[-\pi\Big(\frac{h}{d}+\frac{1}{2}log_e\frac{1-h/d}{1+h/d}\Big)-2\int_0^{h/d}\frac{(h^2/d^2-\bar{y}^2)^{\frac{1}{2}}\bar{y}}{\bar{y}^2+a^2/d^2}tan^{-1}\frac{a/d}{\bar{y}}d\bar{y}\Big]. \quad (1.5)$$

The free energy (W_f) is shown in Figure 1.21 as a function of a/d when $B_0 = 10$ G for several values of the interaction distance d . The figure shows that when the two magnetic fragments approach each other the free energy stored in the system increases, until it is released by reconnection. Figure 1.22 ilustrates the pre-interaction phase, the interaction phase, the cancelation phase and the final state for four different configurations of the magnetic fragments (Priest et al., 1994). Figure 1.22a shows the basic model with equal in strength but oppositely directed magnetic polarities. Figure 1.22b is the corresponding model if the two magnetic elements are not equal in strength, where the final state consists of a single source containing the remaining field lines that have not reconnected superposed on the ambient uniform horizontal field. Figures 1.22c and 1.22d depict the interaction between a bipolar region and a unipolar element. In Figure 1.22c the unipolar element is weaker than each pole of the bipolar region, and the final state consists of a pole and bipole in a uniform field. Figure 1.22d shows the case when the unipolar element is stronger, and

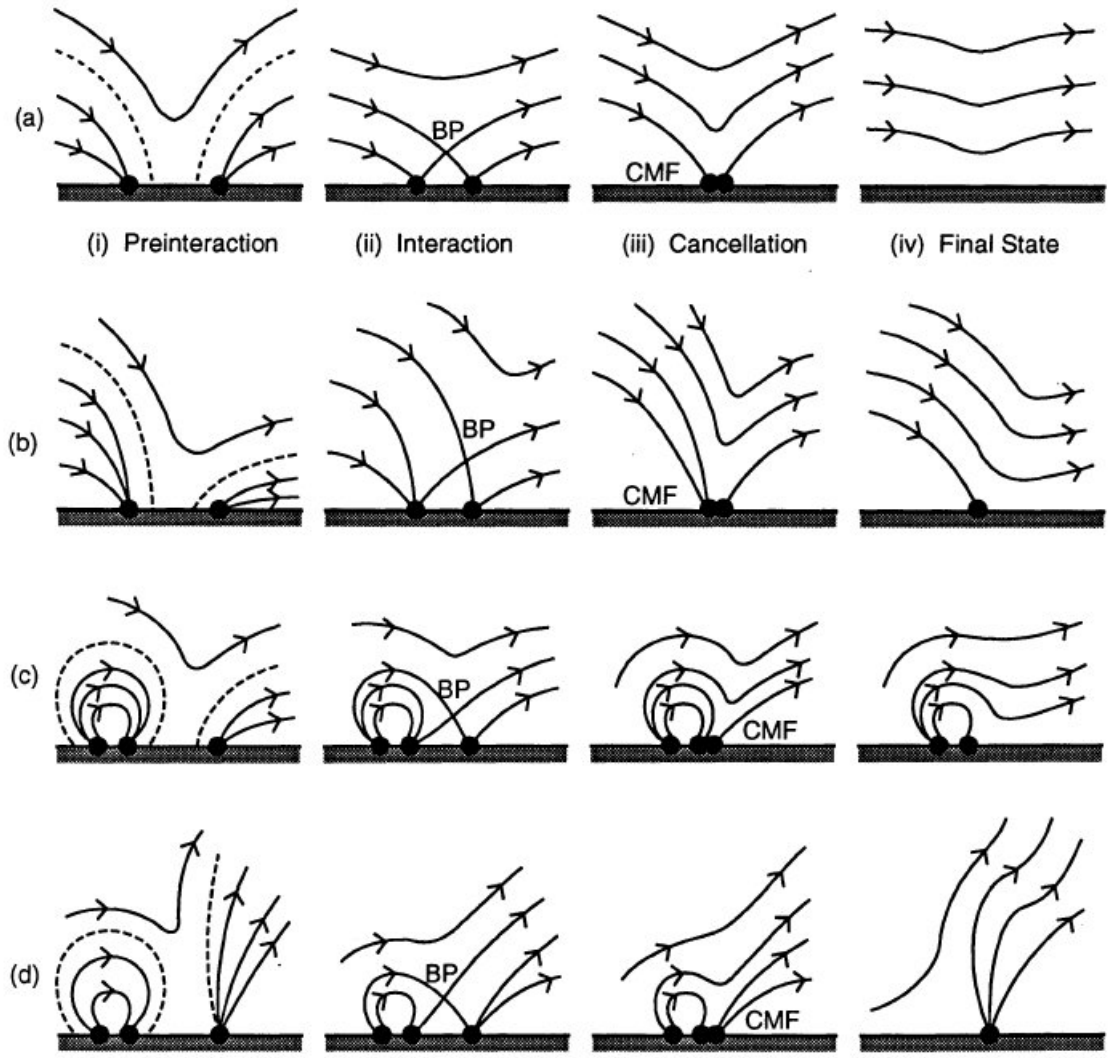

FIGURE 1.22 - Pre-interaction phase, interaction phase, cancelation phase and final state in the approach and interaction of four different configurations of the magnetic fragments. (Priest et al., 1994)

the final state is a unipole in the uniform field.

A model for x-ray bright points due to unequal canceling flux sources in an overlying horizontal field was developed in (Parnell et al., 1994b). The model is similar to that developed in (Priest et al., 1994), it contains a pre-interaction phase, an interaction phase and a cancelation phase. However, in this model an extra phase occurs called the capture phase, which starts after the interaction phase and before the cancelation phase. Figure 1.23 shows the configuration of the magnetic field, the position of the null point and the position of the poles during the different phases of the model. The pre-interaction phase starts with two poles, one of strength $-g$ situated at $-a$ and the other of strength f positioned at position a, representing two magnetic regions of opposite sign and different strengths lying in the plane of the photosphere. When the poles have half-separation of

$a > d_i$, where d_i is called the interaction distance, they are unconnected (Figure 1.23a). When the half-separation a is equal to d_i a neutral point forms in the photospheric plane (x-axis) in between the two poles (Figure 1.23b). During the interaction phase the poles continue moving together and their half-separation lies in the range $d_c < a < d_i$, where d_c is the capture distance (Figure 1.23c). When $a = d_c$, the weaker pole becomes fully connected to the stronger pole and the neutral point descends back down to the photosphere (Figure 1.23d). As the two poles continue to move together reconnection ceases and the capture phase starts. With the weaker pole fully connected to the stronger pole, two neutral points appear on the photosphere, lying to the left of the poles (Figure 1.23e). The neutral points diverge until the poles have zero separation, when at $a = 0$ the cancelation phase starts (Figure 1.23f). The magnetic field components (B_x, B_y) for a potential configuration, in this model, are given by

$$B_y + iB_x = \frac{if/\pi}{z - a} - \frac{ig/\pi}{z + a} + iB_0, \tag{1.6}$$

where $z = x + iy$ and B_0 is the strength of the ambient magnetic field. If no reconnection occurs, a vertical current sheet will be created. The magnetic energy then exceeds that of a purely potential field by an amount that can be later released by reconnection to generate the BP. The free magnetic energy is calculated in the same way as in (Priest et al., 1994). Figure 1.24 shows the free energy as a function of a/d_i when the background field is 10 G. The free energy changes for different values of the separation distance, but now it depends also on the pole strength ratio (k).

All these models were essentially two-dimensional. Other three dimensional models for BPs are described in (Parnell et al., 1994a) and (Mandrini et al., 1996). However, these models are qualitative and do not make predictions about the energy. A different 3D model for current sheet formation and reconnection in X-ray BPs was proposed by (Longcope, 1998). His model tries to predict the reconnection rate based on the observable quantities: magnetic flux, field strength, and polar separation. Figure 1.25 shows the geometry of his modeled bipole. It consists of a positive (P) and a negative (N) pole, of fluxes ψ_+ and ψ_-, separated by a distance d. For simplicity the bipoles are considered to have the same flux ψ_0. An overlying background field $(\vec{B}_0)$ was considered, whose origin is assumed far away compared with the distance between the polarities that form the bipole. The poles are located at positions $\vec{x}_+$ and $\vec{x}_-$, and the axis of the bipole makes an angle ϕ with respect to the background field vector $\vec{B}_0$. For a current free corona the resulting magnetic field can be written as

$$\vec{B}(\vec{x}) = \frac{\psi_+}{2\pi} \frac{\vec{x} - \vec{x}_+}{|\vec{x} - \vec{x}_+|^3} - \frac{\psi_-}{2\pi} \frac{\vec{x} - \vec{x}_-}{|\vec{x} - \vec{x}_-|^3} + \vec{B}_0. \tag{1.7}$$

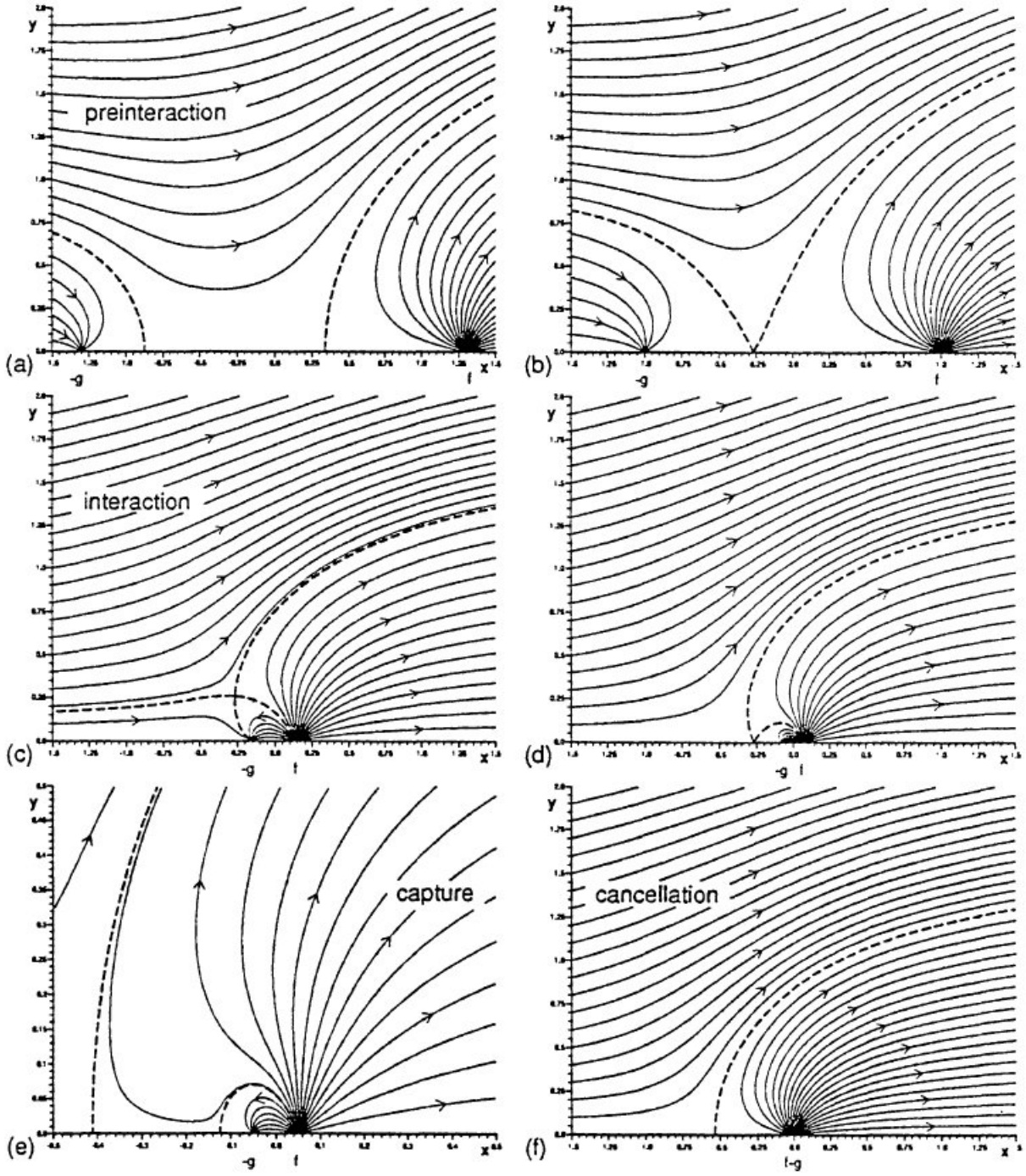

FIGURE 1.23 - Configuration of the magnetic field, position of the null point and position of the poles during different phases of the model for x-ray BPs due to unequal canceling flux sources. (Parnell et al., 1994b)

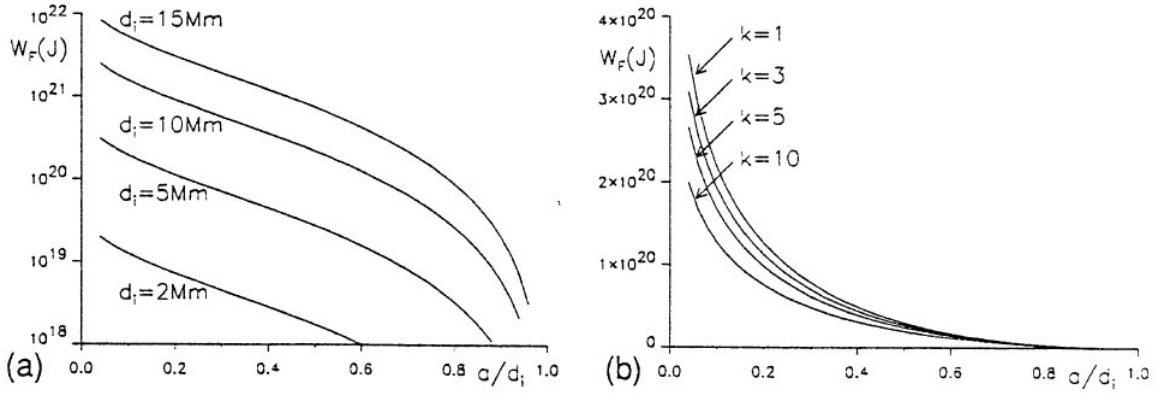

FIGURE 1.24 - Free energy as a function of a/d_i for different values of (a) the interaction distance and of (b) the pole strength ratio. (Parnell et al., 1994b)

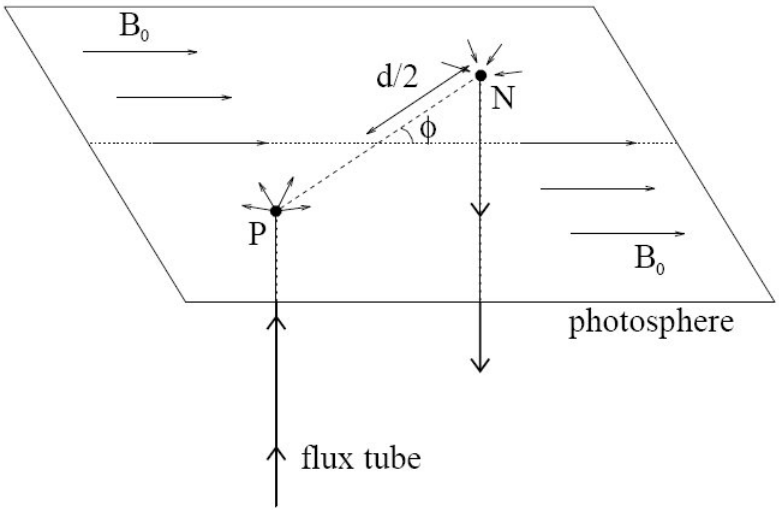

FIGURE 1.25 - Geometry of the model bipole studied using the 3D model for current sheets formation and reconnection in X-rays BPs. (Longcope, 1998)

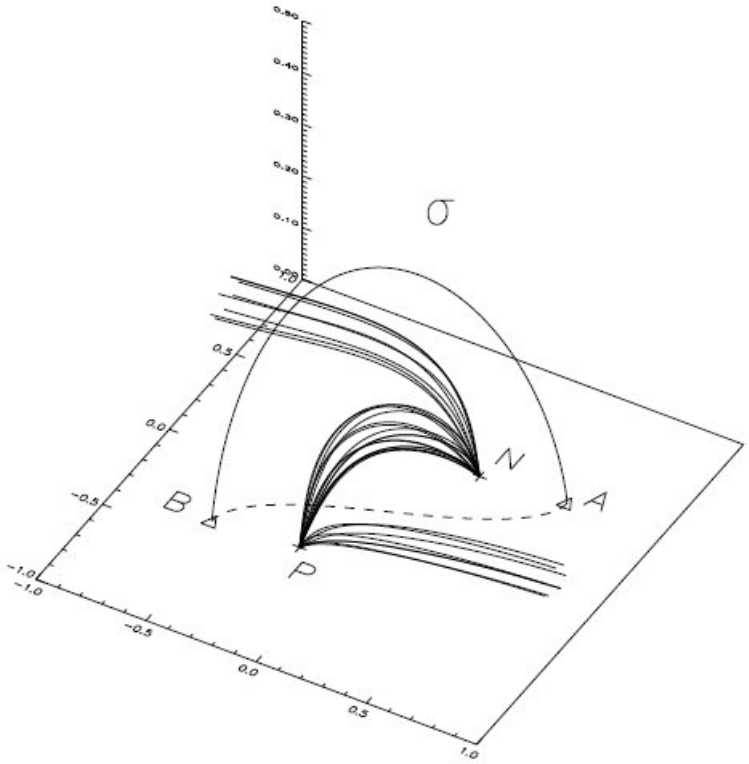

FIGURE 1.26 - Three of the four possible categories of magnetic field lines connecting the poles and the background field. (Longcope, 1998)

One important quantity is the dimensionless separation vector, defined as

$$\vec{\rho} \equiv \frac{1}{2} l^{-1}(\vec{x}_- - \vec{x}_+) = l^{-1}\vec{x}_-, \tag{1.8}$$

where $l \equiv \sqrt{\psi_0/B_0}$ is the characteristic length scale. This vector entirely characterizes the bipole, and its magnitude represents the dimensionless separation

$$\rho = \frac{1}{2} d/l. \tag{1.9}$$

Figure 1.26 shows three of the four possible categories of magnetic field lines: those field lines that begin at P and end at N form the domain P–N (the magnetic bipole itself); the field lines that begin at P and then extend to ∞ form the domain P–∞, thereby linking P to the background field; the field lines beginning at ∞ and ending at N define the domain ∞–N; and finally, the purely background field lines that begin and end at ∞ form the domain ∞–∞. The triangles A and B mark the position of the null points, where the magnetic field vanishes. The line connecting the two nulls is called separator and indicated by σ. The domains are separated from one another by surfaces called separatrices. Figure 1.27 show two different separatrices: one ending at the null point A, called separatrix

surface Σ_A, and the other ending at the null point B, called separatrix surface Σ_B. Inside Σ_A all field lines terminate at N and outside of it all field lines continue to ∞ (Figure 1.27a). Inside Σ_B all field lines begin at P and this surface divides the domains P–N and P–∞ from the domains ∞–N and ∞–∞ (Figure 1.27b). The domain P–N is simultaneously within Σ_A and Σ_B, characterizing the interaction region. When the two regions defined by Σ_A and Σ_B do not intersect there are no field lines connecting P and N, and there is no bipole. The model considers that a motion is responsible for the evolution of the bipole which gives rise to an electric current parallel to the separator line, in a way that the total flux in the domain P-N keeps constant. The magnetic energy in a configuration containing the current is larger than the magnetic energy in the current-free configuration. This difference in energy (ΔE) is the free energy that will be used to power the BPs. The free magnetic energy is dissipated by reconnection, which is triggered in the model by an instability that generates anomalous resistivity. The instability will occur if the current exceeds a threshold θI^*, where θ is a dimensionless parameter that depends on the nature of the instability. Once triggered the effect of the reconnection is to transfer enough flux across the separator and as a consequence the current ribbon disappears. The new equilibrium configuration has lowered the energy by a factor of ΔE, which corresponds to the free energy. As the poles continue to move, currents build up until they reach a threshold which allows reconnection. Figure 1.28 illustrates this scenario for a bipole undergoing cancelation along an axis making an angle of $\phi = 120^o$ with respect to the background. The characteristic values are $B_0 = 10$ G, $\psi_0 = 10^{19}$ Mx and $l = 10^9$ cm. Each pole is moving at $v = 300$ m/s and the interaction distance is $\rho \approx 0.5$. Finally, the threshold coefficient is chosen $\theta = 0.15$. Figure 1.28a shows the variation of θ with time. When the magnitude of this quantity reaches 0.15 reconnection occurs. Figure 1.28b show the evolution of the electric current in units of 10^{10} A. The evolution of the flux connecting the poles P and N is shown in Figure 1.28c. It is clear from the figure that the role of the reconnection is to transfer flux to this domain. Figures 1.28d and 1.28e show the free energy ΔE and a depiction of the energy liberated during each reconnection event, respectively.

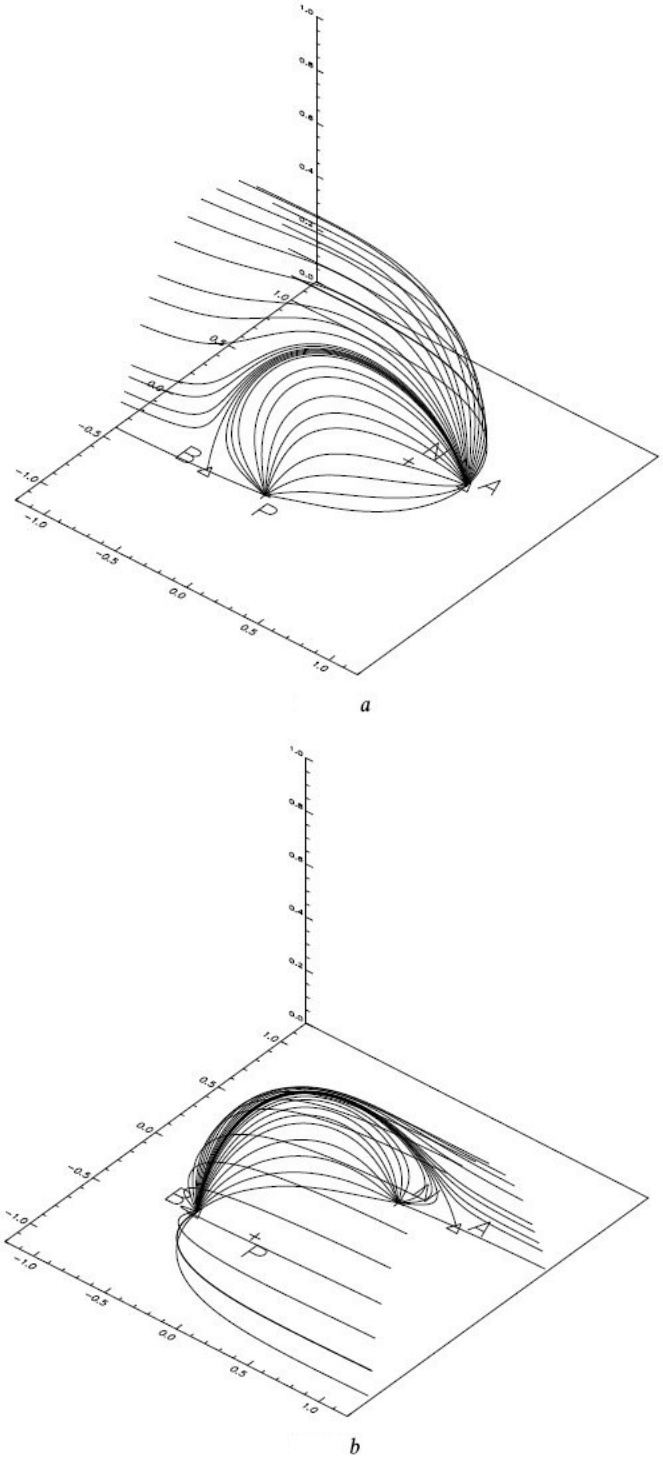

FIGURE 1.27 - Two different separatrices, one ending at (a) the null point A and the other ending at (b) the null point B. (Longcope, 1998)

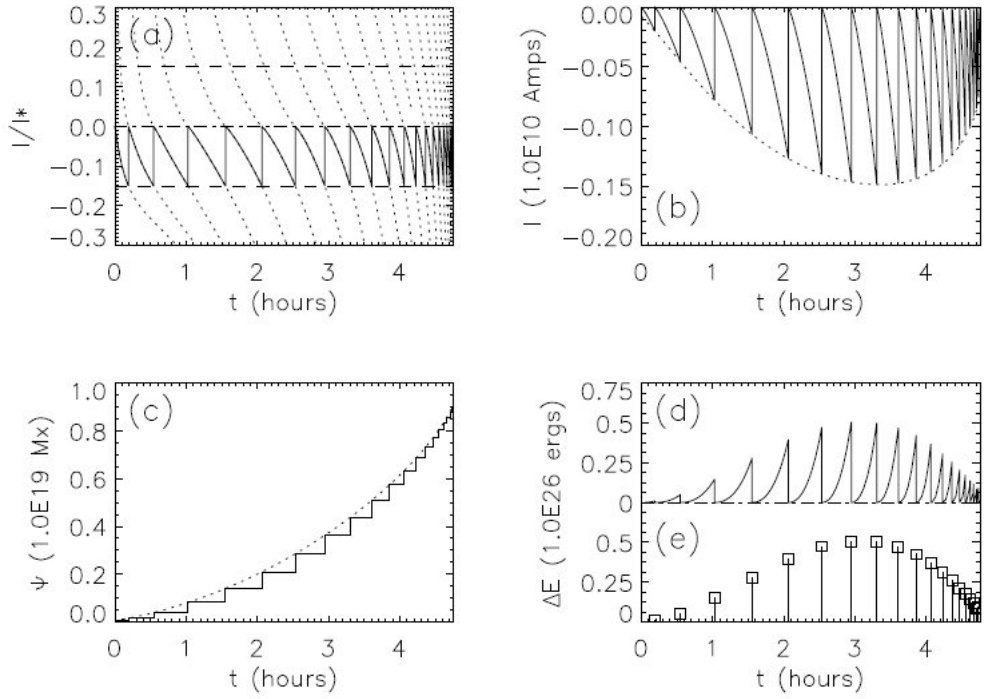

FIGURE 1.28 - Time variation of different parameters for a bipole undergoing cancelation along an axis making an angle of $\phi = 120^o$ with respect to the background. The characteristic values are $B_0 = 10G$, $\psi_0 = 10^{19}Mx$ and $l = 10^9cm$. Each pole is moving at $v = 300m/s$ and the interaction distance is $\rho \approx 0.5$. The threshold coefficient for reconnection is $\theta = 0.15$. (Longcope, 1998)

2 INFERRING PLASMA FLOW VELOCITIES FROM PHOTOSPHERIC MAGNETIC FIELD OBSERVATIONS

As a starting point for the investigation of the building up of free magnetic energy in the solar corona it is appropriate to utilize the observable photospheric magnetic field evolution. In fact, the photosphere is nowadays the only layer in which the magnetic field can be reliably measured. Since it is the boundary between the solar interior and the solar atmosphere, emerging plasma and magnetic flux pass through this region before they reach the solar corona. The motion of the foot points of magnetic flux tubes in the photosphere determine the evolution of the coronal plasma and magnetic field. So, knowing what happens at the photospheric boundary is the first step to understand the dynamics of the solar atmosphere. Also, if one wants to carry out MagnetoHydroDynamic (MHD) simulations of the solar atmosphere, it is appropriate to introduce the observed photospheric magnetic field and the inferred plasma motion as boundary conditions of the model. This might reveal important physical phenomena occurring in the solar atmosphere that are related to the photospheric evolution.

Data driven three-dimensional (3D) MHD models of the solar atmosphere can utilize initial conditions for the magnetic field obtained from measured photospheric magnetic field (Büchner et al., 2004a; Wu et al., 2006; Gudiksen; Nordlund, 2005; Peter et al., 2006). They also can include estimates of the plasma velocity in addition to this magnetic field to drive the evolution of the photospheric boundary. Therefore, an important task in working with such a kind of models is to determine the magnetic field configuration and the plasma velocities using the available data.

By its definition, when the Magnetic Reynolds number ($R_m = \frac{VL}{\eta}$) is very large the diffusion (η) is relatively unimportant, and the magnetic field lines are advected with the fluid flow (frozen-in theorem). Since this condition is fulfilled in the photosphere, plasma velocity can be determined from the evolution of photospheric magnetic features. Many methods are suggested for calculating the photospheric plasma velocity from a sequence of photospheric magnetograms:

- The local correlation tracking method (November; Simon, 1988);
- The inverse problem of the induction equation (Kusano et al., 2002);
- A combination of the induction equation and the local correlation method (Welsch et al., 2004);
- The minimum energy fit method (Longcope, 2004).

In this chapter, methods to derive the photospheric plasma velocity using photospheric magnetic field measurements are reviewed (Section 2.1) and applied to real photospheric magnetic field data (Section 2.2). A discussion of which method can be applied to observed line-of-sight (LOS) magnetic fields and which method seems to be more appropriate to use with vector magnetograms is given at the end (Section 2.3).

2.1 The methods

2.1.1 Local Correlation Tracking (LCT)

This technique was originally developed by (Leese et al., 1970) and (Leese et al., 1971) for tracking clouds. It was introduced into the solar physics by (November; Simon, 1988). The method measures the displacements of the various patterns in a pair of images and finds an average velocity associated with these displacements, assuming that the motions causing the displacements are smooth.

The idea behind this method is to find the displacement that maximizes the spatially localized cross correlation between two images of a scene separated by a sampling time delay τ, that is smaller than the lifetime of tracers in the scene. The two-dimensional cross correlation function is determined at each sub-region of the image by multiplying an intensity product with a window function $W(r)$, where $r = (x, y)$ represents the position of the center of the window function. The spatially localized cross correlation $C(\delta, r)$ is a function of four dimensions: the two-dimensional displacement δ between the images, and the two-dimensional central location r of the window function. $C(\delta, r)$ is defined in terms of the intensity images $J_t(\epsilon)$ and $J_{t+\tau}(\epsilon)$ which sample the scene at the two times t and $t + \tau$:

$$C(\delta, r) = \int_S J_t(\epsilon - \frac{\delta}{2}) J_{t+\tau}(\epsilon + \frac{\delta}{2}) W(r - \epsilon) d\epsilon, \tag{2.1}$$

where ϵ represents the space coordinates of a pixel. The integral is over the full area of the images, but effectively it is limited in extent by the size of the window function $W(r)$. The window size defines the spatial resolution of the vector displace determination.

The spatially localized cross correlation defined by equation (2.1) slides the two images symmetrically in opposite directions. This equation has the symmetry that the sign of the displacement δ flips upon interchange of the images J_t and $J_{t+\tau}$. The maximum of the cross correlation is a most reasonable definition for the motion of a tracer which undergoes evolutionary changes between successive image snapshots. This formulation is not affected by contrast variations that occur over the area of the window since it deals directly with the pixel values.

After computing the spatially localized cross correlation $C(\delta, r)$ for various displacements δ, an interpolation in δ is performed on the cross correlation to define the displacement that locally maximizes the cross correlation:

$$\frac{\partial C(\delta, r)}{\partial \delta}\Big|_{\delta=\Delta(r)} = 0. \tag{2.2}$$

The velocity is then obtained dividing the displacement $\Delta(r)$ by the time interval τ between the two images.

As pointed by (Georgoulis; LaBonte, 2006), a crucial requirement for the LCT method to work is that the studied patterns must exhibit significant contrast differences to be followed effectively in time. Moreover, the patterns must maintain their structural integrity for time scales much larger than the cadence of the observations since a continuous restructuring would make tracking problematic. In the quiet photospheric filigree observed in optical wavelengths these two requirements are fulfilled, but what about for the magnetic features in the solar photosphere?

In (Georgoulis; LaBonte, 2006) some reasons why LCT technique may be problematic are enumerated. First, it is not clear which input would give more appropriate results to LCT algorithms, as both the continuum images and the magnetogram images reveal different aspects of the photospheric flows. Second, both the white light and the magnetogram structures may reform rapidly at length and time scales necessary to infer the flows with sufficient detail. This introduces uncertainties in the LCT results. Third, the LCT technique requires a window function whose size is typically a few times larger than the instrument's pixel size. This is because the LCT maximizes the cross-correlation function by applying displacements to the initial image and by comparing the result with the second image of the pair, so each region must contain sufficient structure to yield a well-defined peak of the cross-correlation function. Different choices of the window function reflect different types of flows and give different results, since the kinetic power is distributed to a variety of spatial scales in the photosphere. Small window sizes tend to reveal the small-scale convection, while large window sizes reproduce systematic flows observed, e.g., during the emergence of magnetic dipole(s) that eventually form an active region. Fourth, some systematic motion patterns do not even correspond to actual flows. They are apparent and due to the emergence of inclined magnetic structures. Tracking techniques tend to attribute a fictitious transverse velocity to these purely vertical flows. In addition to this, (Welsch et al., 2004) found that noisy fluctuations in regions of weak magnetic field lead to spurious correlation there. For this reason it is recommended to discard correlation in such weak magnetic field regions. It was also found that Δt have to be large enough that mean changes in B_z exceed fluctuations in B_z. Another problem can

appear near the lines of polarity inversion, usually known as neutral lines, due to the fact that opposite-polarity fields move independently of each other, even in close proximity, causing crosstalk in the correlations and affecting LCT velocities.

One main problem with applying LCT to the magnetized photosphere was described in (Démoulin; Berger, 2003), (Longcope, 2004), (Welsch et al., 2004) and (Schuck, 2005). It is that LCT will accurately recover the photospheric velocity only if the changes in the intensity are primarily caused by the velocity through advection

$$\frac{\partial J}{\partial t} + \vec{v}_h \cdot \vec{\nabla} J = 0, \tag{2.3}$$

where $\vec{v}_h$ is the horizontal velocity of the tracer. However, the vertical magnetic field, measured by line-of-sight magnetograms, evolves according to the magnetic induction equation,

$$\frac{\partial B_z}{\partial t} + \vec{v}_h \cdot \vec{\nabla} B_z = -B_z \vec{\nabla} \cdot \vec{v}_h + \vec{\nabla} \cdot (v_z \vec{B}_h), \tag{2.4}$$

rather than according to the horizontal, scalar advection equation assumed by the LCT method. The principal source of difficulty in applying LCT to magnetograms stems from the second term on the right hand side of equation (2.4). According to this term, vertical flow may interact with the horizontal field to change B_z. Standard LCT will attribute this change to a fictitious horizontal velocity, a pattern velocity not corresponding to fluid flow (Démoulin; Berger, 2003).

2.1.1.1 The Démoulin & Berger relation

It was first mentioned by (Démoulin; Berger, 2003) that the apparent horizontal velocity field of magnetic features in magnetograms, $\vec{u}$, is not necessarily identical to plasma velocity field tangent to the surface, $\vec{v}_h$. It is considered that an emergence of a flux tube can contribute to the observed horizontal velocity, as the photospheric footpoints separate when the flux tube emerges.

To exemplify, a simple case is analyzed in (Démoulin; Berger, 2003): a magnetic configuration that is ideally transported by plasma motions across the photospheric boundary with only a vertical velocity component (v_z). By geometrical arguments it was shown that the photospheric footpoint moves with a fictitious horizontal velocity

$$\vec{u}_f = -\frac{v_z}{B_z} \vec{B}_h. \tag{2.5}$$

Hence, vertical motions ($\vec{v}_z$) produce a seeming horizontal velocity ($\vec{u}_f$), which is incorporated by tracking methods. Consequently, a correct relation between the velocity obtained

by tracking methods and the horizontal velocity would be

$$\vec{u} = \vec{v}_h - \frac{v_z}{B_z}\vec{B}_h. \tag{2.6}$$

This relation is often called the Démoulin & Berger relation.

2.1.2 A combination of LCT with induction equation

A combination of LCT and the induction equation was first discussed by (Kusano et al., 2002) and (Welsch et al., 2004). Such combination accounts for the differences between the vertical magnetic field evolution obtained using LCT velocities and that obtained by measurements. It requires that the flow field obtained from observations of the photospheric magnetic field satisfies at least the vertical component of the ideal MHD induction equation.

The magnetic field evolution at the photosphere is assumed to be consistent with the ideal MHD induction equation

$$\frac{\partial \vec{B}}{\partial t} = \vec{\nabla} \times (\vec{v} \times \vec{B}). \tag{2.7}$$

Since the transverse components of the induction equation contain derivatives in the vertical direction, which cannot be determined observationally, only the vertical component of the equation (2.7) can be considered, giving

$$\frac{\partial B_z}{\partial t} = \vec{\nabla} \times (\vec{v}_h \times \vec{B}_z + \vec{v}_z \times \vec{B}_h). \tag{2.8}$$

Following equation (2.8), the time derivative of the vertical photospheric magnetic field component (B_z) can be seen as a consequence of flux emergence and horizontal transport.

2.1.2.1 The inverse problem of the induction equation

A method for reconstructing a velocity field that satisfies both LCT results and the vertical component of the induction equation was developed by (Kusano et al., 2002). This method is called 'the inverse problem of the induction equation', and it consists of finding a velocity $\vec{v}_z$ that satisfies the induction equation when $\frac{\partial \vec{B}_z}{\partial t}$, $\vec{B}_z$, $\vec{B}_h$ and $\vec{v}_h$ are given in a surface S (photosphere).

The first problem is to find the regions where equation (2.8) has a unique solution. To consider the uniqueness of $\vec{v}_z$, it is assumed that two different velocities $\vec{v}_1 = \vec{v}_h + \vec{v}_{1z}$ and

$\vec{v}_2 = \vec{v}_h + \vec{v}_{2z}$, which have a common horizontal component, satisfy the induction equation

$$\frac{\partial \vec{B}_z}{\partial t} = \vec{\nabla} \times (\vec{v}_1 \times \vec{B})_h \tag{2.9}$$

$$\frac{\partial \vec{B}_z}{\partial t} = \vec{\nabla} \times (\vec{v}_2 \times \vec{B})_h. \tag{2.10}$$

The difference between equations (2.9) and (2.10) gives

$$\begin{aligned} \vec{\nabla} \times [(\vec{v}_1 - \vec{v}_2) \times \vec{B}]_h &= 0 \Rightarrow \\ (\vec{V} \times \vec{B})_h &= \vec{\nabla}_h \psi, \end{aligned} \tag{2.11}$$

where $\vec{\nabla}_h = \left(\frac{\partial}{\partial x}, \frac{\partial}{\partial y}, 0\right)$, $\vec{V} = \vec{v}_1 - \vec{v}_2$, and ψ is an arbitrary scalar function. The velocity $\vec{V} = \vec{v}_{1z} - \vec{v}_{2z}$ has only component perpendicular to S. As a consequence, equation (2.11) can be rewritten as

$$\vec{V} \times \vec{B}_h = \vec{\nabla}_h \psi, \tag{2.12}$$

and by the vector product with $\vec{B}_h$ it is obtained

$$\vec{V} = \frac{\vec{B}_h \times \vec{\nabla}_h \psi}{B_h^2}. \tag{2.13}$$

The area where ψ is constant produces $\vec{\nabla}_h \psi = 0$ and $\vec{V}$ vanishes. From this, it can be concluded that $v_1 = v_2$ and the solution is unique in this area.

The scalar product of equation (2.12) with $\vec{B}_h$ also produces

$$\begin{aligned} \vec{B}_h \cdot (\vec{V} \times \vec{B}_h) &= (\vec{B}_h \cdot \vec{\nabla})\psi \Rightarrow \\ (\vec{B}_h \cdot \vec{\nabla})\psi &= 0, \end{aligned} \tag{2.14}$$

which shows that ψ is constant along the horizontal field line defined by $\vec{r} = \vec{r}_0 + \int \frac{\vec{B}_h}{B_h} dl$, where $\vec{r}_0$ is an arbitrary point on S and l is the arc length along the field line. So, the solution is unique in the area along the tangential field lines.

The next step is to formulate the solution $\vec{v}_z$ in the restricted inverse problem. Following (Kusano et al., 2002), a vector potential $\vec{A}$ is defined as a vector field satisfying

$$\vec{\nabla} \times \vec{A} = \vec{B}, \tag{2.15}$$

$$\vec{\nabla} \cdot \vec{A} = 0 \tag{2.16}$$

and

$$\vec{\nabla}_z A_z = 0 \tag{2.17}$$

on the surface S. The vertical gradient is given by $\vec{\nabla}_z = (0, 0, \frac{\partial}{\partial z})$.

Calculating the rotational of equation (2.15) it is obtained

$$\begin{aligned} \vec{\nabla} \times (\vec{\nabla} \times \vec{A}) &= \vec{\nabla} \times \vec{B} \Rightarrow \\ \vec{\nabla}(\vec{\nabla} \cdot \vec{A}) - (\vec{\nabla} \cdot \vec{\nabla})\vec{A} &= \vec{\nabla} \times \vec{B} \Rightarrow \\ -\nabla^2 \vec{A} &= \vec{\nabla} \times \vec{B}. \end{aligned} \tag{2.18}$$

From this equation it follows that

$$\nabla_h^2 \vec{A}_h = -\vec{\nabla} \times \vec{B}_z, \tag{2.19}$$

and if a proper boundary condition is imposed, this equation gives a unique solution of $\vec{A}_h$ on S.

Once the vector potential $\vec{A}$ is determined, the induction equation can be converted to

$$\begin{aligned} \frac{\partial \vec{B}}{\partial t} &= \vec{\nabla} \times (\vec{v} \times \vec{B}) \Rightarrow \\ \frac{\partial}{\partial t}(\vec{\nabla} \times \vec{A}) &= \vec{\nabla} \times (\vec{v} \times \vec{B}) \Rightarrow \\ \vec{\nabla} \times \frac{\partial \vec{A}}{\partial t} - \vec{\nabla} \times (\vec{v} \times \vec{B}) &= 0 \Rightarrow \\ \vec{\nabla} \times \left(\frac{\partial \vec{A}}{\partial t} - \vec{v} \times \vec{B} \right) &= 0 \Rightarrow \\ \frac{\partial \vec{A}}{\partial t} - \vec{v} \times \vec{B} &= -\vec{\nabla}\phi \Rightarrow \\ \frac{\partial \vec{A}}{\partial t} &= \vec{v} \times \vec{B} - \vec{\nabla}\phi, \end{aligned} \tag{2.20}$$

where ϕ is some scalar function. Calculating the divergence of this equation leads to

$$\begin{aligned} \frac{\partial}{\partial t} \vec{\nabla} \cdot \vec{A} &= \vec{\nabla} \cdot (\vec{v} \times \vec{B}) - \vec{\nabla} \cdot \vec{\nabla}\phi \Rightarrow \\ \nabla^2 \phi &= \vec{\nabla} \cdot (\vec{v} \times \vec{B}). \end{aligned} \tag{2.21}$$

By applying the operator $\vec{\nabla}_z \cdot$ on equation (2.20) it is obtained

$$\begin{aligned}
\vec{\nabla}_z \cdot \left(\frac{\partial \vec{A}}{\partial t}\right) &= \vec{\nabla}_z \cdot (\vec{v} \times \vec{B}) - \vec{\nabla}_z \cdot \vec{\nabla}\phi \Rightarrow \\
\frac{\partial}{\partial t}\nabla_z A_z &= \vec{\nabla}_z \cdot (\vec{v} \times \vec{B}) - \nabla_z^2 \phi \Rightarrow \\
\nabla_z^2 \phi &= \vec{\nabla}_z \cdot (\vec{v} \times \vec{B}),
\end{aligned} \tag{2.22}$$

on the surface S. From equations (2.21) and (2.22) it is clear that the scalar function must also satisfy

$$\nabla_h^2 \phi = \vec{\nabla}_h \cdot (\vec{v} \times \vec{B}). \tag{2.23}$$

From the vector product of equation (2.20) with $\vec{B}$ it is obtained

$$\begin{aligned}
\vec{B} \times \frac{\partial \vec{A}}{\partial t} &= \vec{B} \times (\vec{v} \times \vec{B}) - \vec{B} \times \vec{\nabla}\phi \Rightarrow \\
\vec{B} \times \left(\frac{\partial \vec{A}}{\partial t} + \vec{\nabla}\phi\right) &= B^2 \vec{v} - (\vec{B} \cdot \vec{v})\vec{B}.
\end{aligned} \tag{2.24}$$

Expressing $\vec{A}$, $\vec{B}$, and $\vec{v}$ in the form

$$\vec{A} = \vec{A}_z + \vec{A}_h, \tag{2.25}$$

$$\vec{B} = \vec{B}_z + \vec{B}_h, \tag{2.26}$$

and

$$\vec{v} = \vec{v}_z + \vec{v}_h, \tag{2.27}$$

the vertical component of equation (2.24) leads to

$$\begin{aligned}
B^2 \vec{v}_z - (v_z B_z + v_h B_h)\vec{B}_z &= \vec{B}_h \times \left(\frac{\partial \vec{A}_h}{\partial t} + \vec{\nabla}_h \phi\right) \Rightarrow \\
(B^2 - B_z^2)\vec{v}_z &= (\vec{v}_h \cdot \vec{B}_h)\vec{B}_z + \vec{B}_h \times \left(\frac{\partial \vec{A}_h}{\partial t} + \vec{\nabla}_h \phi\right) \Rightarrow \\
B_h^2 \vec{v}_z &= (\vec{v}_h \cdot \vec{B}_h)\vec{B}_z + \vec{B}_h \times \left(\frac{\partial \vec{A}_h}{\partial t} + \vec{\nabla}_h \phi\right) \Rightarrow \\
\vec{v}_z &= \frac{(\vec{v}_h \cdot \vec{B}_h)\vec{B}_z + \vec{B}_h \times \left(\frac{\partial \vec{A}_h}{\partial t} + \vec{\nabla}_h \phi\right)}{B_h^2}.
\end{aligned} \tag{2.28}$$

The vertical velocity v_z is solvable only from the information on surface S and the conditions imposed on the boundary of S for ϕ, for example the Dirichlet condition $\phi = 0$.

The procedure to obtain the photospheric plasma velocity field from photospheric magnetic field measurements, developed in (Kusano et al., 2002), can be summarized as follows:

a) The photospheric magnetic field vector $\vec{B}$ is obtained at successive moments $t_0 - \frac{\Delta t}{2}$ and $t_0 + \frac{\Delta t}{2}$ from a vector magnetograph.

b) The variation of the magnetic field is numerically calculated using a finite difference method: $\frac{\partial \vec{B}_z}{\partial t} \approx [B_z(t_0 + \Delta t/2) - B_z(t_0 - \Delta t/2)]$.

c) The horizontal velocity $\vec{v}_h$ is constructed by applying the local correlation tracking technique on the data $\vec{B}_z$.

d) The vector potential $\vec{A}_h$ is derived from observed data $\vec{B}_z$ by solving equation (2.19).

e) The scalar potential ϕ is obtained by solving equation (2.23).

f) The vertical velocity is solved from equation (2.28).

In the last computation described in (Kusano et al., 2002), an iterative technique is used in which a trial function of ϕ, e.g. $\phi = 0$, is adopted first. The calculations of $\vec{v}$ and ϕ are successively repeated using equations (2.28) and (2.23), respectively, until a nearly self-consistent solution is obtained. It was found that the iterative process quickly converges with a sufficient accuracy when the Dirichlet condition ($\phi = 0$) is adopted.

2.1.2.2 The ILCT technique

In (Welsch et al., 2004) a technique was developed to derive flow fields consistent with both the induction equation and LCT results. The technique is dubbed as 'ILCT', just adding I (for the induction equation) to LCT. Unlike the approach in (Kusano et al., 2002), the technique developed in (Welsch et al., 2004) uses only standard Fourier and algebraic methods in two dimensions.

The vertical component of the induction equation (2.8) is written as

$$\frac{\partial B_z}{\partial t} = \vec{\nabla}_h \cdot (v_z \vec{B}_h - B_z \vec{v}_h), \tag{2.29}$$

and a temporal finite-difference approximation is used to rewrite this equation as

$$\frac{\Delta B_z}{\Delta t} = \vec{\nabla}_h \cdot (v_z \bar{\vec{B}}_h - \bar{B}_z \vec{v}_h), \tag{2.30}$$

where the overbar on the magnetic field component refers either to a temporal average of fields between times t_i and t_{i+1}, used in LCT, or to the measured field at an intermediate time $t_{i+\frac{1}{2}}$.

From the Démoulin & Berger relation (2.6), it can be obtained

$$\begin{aligned} \vec{u} &= \vec{v}_h - \bar{\vec{B}}_h \frac{v_z}{\bar{B}_z} \Rightarrow \\ -\vec{u}\bar{B}_z &= \bar{\vec{B}}_h v_z - \vec{v}_h \bar{B}_z, \end{aligned} \tag{2.31}$$

where $\vec{u}$ is the velocity recovered by LCT method, for example, and $\vec{v}_h$ and v_z are the actual horizontal and vertical components of the velocity, respectively. Substituting this result in equation (2.30), gives

$$\frac{\Delta B_z}{\Delta t} = -\nabla_h \cdot (\vec{u}\bar{B}_z). \tag{2.32}$$

The solution method of (Welsch et al., 2004) begins with decomposing the vector field $\vec{u}\bar{B}_z$ into the sum of the curl of a stream function, ψ, and the gradient of a scalar function, ϕ,

$$\vec{u}\bar{B}_z \equiv \vec{\nabla}_h \times \psi\hat{n} - \vec{\nabla}_h\phi, \tag{2.33}$$

where $\vec{u}$ is the recovered velocity pattern and $\hat{n}$ is the unit vector perpendicular to the plane S. Substituting equation (2.33) into the equation (2.32) follows

$$\begin{aligned} \frac{\Delta B_z}{\Delta t} &= -\vec{\nabla}_h \cdot \left(\vec{u}\bar{B}_z\right) \Rightarrow \\ \frac{\Delta B_z}{\Delta t} &= -\vec{\nabla}_h \cdot \left(\vec{\nabla}_h \times \psi\hat{n} - \vec{\nabla}_h\phi\right) \Rightarrow \\ \frac{\Delta B_z}{\Delta t} &= \nabla_h^2\phi. \end{aligned} \tag{2.34}$$

Equation 2.34 is the Poisson equation for ϕ, where $\frac{\Delta B_z}{\Delta t}$ acts as a source term. After this, the curl of equation (2.33) is taken, giving

$$\begin{aligned} \vec{\nabla}_h \times (\vec{u}\bar{B}_z) &= \vec{\nabla}_h \times (\vec{\nabla}_h \times \psi\hat{n}) - \vec{\nabla}_h \times (\vec{\nabla}_h\phi) \Rightarrow \\ \vec{\nabla}_h \times (\vec{u}\bar{B}_z) &= \vec{\nabla}_h(\vec{\nabla}_h \cdot \psi_v) - \nabla_h^2\psi\hat{n}. \end{aligned} \tag{2.35}$$

The Poisson equation for ψ is obtained after performing the dot product of equation 2.35 with the unit normal vector $(\hat{n})$

$$\nabla_h^2\psi = -\vec{\nabla}_h \times (\vec{u}\bar{B}_z) \cdot \hat{n}. \tag{2.36}$$

Using $\vec{u}^{(LCT)}$ as a first estimate for $\vec{u}$ and solving equations (2.34) and (2.36) for ϕ and ψ, respectively, using standard Fourier techniques, equation (2.33) can be used to obtain a better estimate of $\vec{u}$.

(Welsch et al., 2004) verified that $-\vec{\nabla}\cdot(\vec{u}\bar{B}_z)$ accurately reconstructs $\frac{\Delta B_z}{\Delta t}$. The reconstruction of $\frac{\Delta B_z}{\Delta t}$ using the velocity field obtained by ILCT and that calculated using measurements of B_z only differ in the edges (see figures 1 and 6 of (Welsch et al., 2004)).

The vertical component is calculated using a method called algebraic decomposition. This method assumes that the velocity along the magnetic field is zero ($\vec{v}\cdot\vec{B}=0$). Using this assumption and the Demoulin and Berger relation, it is obtained that

$$v_z = -\frac{B_z}{|\vec{B}|^2}[\vec{u}\cdot\vec{B}_h]. \tag{2.37}$$

The assumption that the velocity parallel to the magnetic field is equal to zero is valid since it is not influencing the time derivative of the vertical component of the magnetic field. From the equation (2.37) it is possible to see that if one wants to calculate the vertical component of the velocity it is necessary to know the three components of the magnetic field in the photospheric plane.

2.1.3 Minimum Energy Fit (MEF)

This technique, introduced in (Longcope, 2004), requires that the photospheric flow agrees with the observed photospheric field evolution according to the magnetic induction equation. It selects, from all consistent flows, the one with the smallest overall flow speed, by demanding that it minimizes a functional.

The method and the minimization procedure is described in (Longcope, 2004). The photosphere surface is taken at $z=0$ and it is required that all three components of the magnetic field are measured there. The magnetic field is assumed to evolve according to the ideal induction equation, equation (2.7), and only the vertical component, given by equation (2.29), is considered. This component depends only on $\vec{v}$ and $\vec{B}$ measured in the photospheric plane (There is no vertical derivative present in the equation).

A magnetogram taken at time t_i includes several distinct regions $M_i^{(\nu)}$ in which $\vec{B}(x,y)$ is measured with sufficient accuracy to infer $\vec{v}$. From the magnetogram a photospheric velocity can be computed only inside these regions. The velocity within one region cannot be meaningfully related to that in any other based on the induction equation alone. Measurements outside of these regions are, in the simplest case, consistent with $\vec{B}=0$ and thus place no constraint on the velocity there. In a more general case the exterior will

contain a mixture of zero and non-zero pixels whose structure is too complex for spatial derivatives to be reliably computed.

The time derivative $\frac{\partial B_z}{\partial t}$ is obtained from measurements on times t_i and t_{i+1} by means of finite differences $\frac{\partial B_z}{\partial t} \approx (B_z^{t_{i+1}} - B_z^{t_i})/\Delta t$. The objective of the MEF method is to find the steady velocity field $\vec{v}$ by which $\vec{B}^{t_i}$ will evolve to $\vec{B}^{t_{i+1}}$ over Δt.

To solve equation (2.29), the same approach used as in (Kusano et al., 2002) and (Welsch et al., 2004) in terms of the unknown scalar potentials $\phi(x, y)$ and $\psi(x, y)$ is used. As proposed in (Longcope, 2004), the term between parenthesis in the right hand side of equation (2.29) can be rewritten as

$$v_z \vec{B}_h - B_z \vec{v}_h = \vec{\nabla}_h \phi + \vec{\nabla}_h \psi \times \hat{z}. \tag{2.38}$$

Substituting it into equation (2.29) one obtains a Poisson equation for $\phi(\vec{x}_h)$

$$\nabla_h^2 \phi = \frac{\Delta B_z}{\Delta t}. \tag{2.39}$$

As in (Kusano et al., 2002), a homogeneous boundary condition, the Dirichlet condition $\phi = 0$, is used. This boundary condition does not compromise the generality of the solution, since transverse velocity components may be added through ψ.

Once $\phi(x, y)$ has been found solving equation (2.39), the transverse velocity is given by equation (2.38)

$$\vec{v}_h = \frac{1}{B_z}(v_z \vec{B}_h - \vec{\nabla}_h \phi - \vec{\nabla}_h \psi \times \hat{z}) \tag{2.40}$$

This velocity satisfies equation (2.29) for all choices of $\psi(x, y)$ and $v_z(x, y)$. To uniquely specify these fields, a constraint on the solution is imposed, which incorporates an independent reference flow $\vec{u}(x, y)$. In this method, the constraint is that the velocity field must be as small as possible. The smallest velocity is defined as the one that minimizes the functional

$$W\{\psi, v_z\} \equiv \frac{1}{2} \int_M [|\vec{v}_h - \vec{u}_h|^2 + |v_z - u_z|^2] dx dy \tag{2.41}$$

For a stationary W under variations of the field $v_z(x, y)$ without variations in $\psi(x, y)$, yields the Euler-Lagrange equation

$$v_z = \frac{B_z^2 u_z + \vec{B}_h \cdot (\vec{\nabla}_h \phi + \vec{\nabla}_h \psi \times \hat{z} + B_z \vec{u}_h)}{|\vec{B}|^2} \tag{2.42}$$

Demanding stationarity under variations of $\psi(x, y)$, while holding $v_z(x, y)$ fixed, yields a

second Euler-Lagrange equation

$$\vec{\nabla}_h \cdot (\frac{\vec{\nabla}_h \psi}{B_z^2}) = \vec{\nabla}_h \cdot [\frac{\hat{z} \times (v_z \vec{B}_h - \vec{\nabla}_h \phi - B_z \vec{v}_h)}{B_z^2}] \tag{2.43}$$

A pair of fields $\psi(x, y)$ and $v_z(x, y)$ which satisfies both equations (2.42) and (2.43), will make W stationary under simultaneous variations. A first guess for the velocity is given and then the scalar function $\psi(x, y)$ is calculated. The value obtained for $\psi(x, y)$ is used to recalculate $v_z(x, y)$ and the method is repeated until the results converge.

A solution for $\psi(x, y)$ and v_z can be obtained iteratively. First, the elliptic equation (2.43) is solved for $\psi(x, y)$ within the domain M. The domain M is defined so that both $\vec{B}$ and $\frac{\partial B_z}{\partial t}$ vanish outside of it. No flow crossing the boundary is required: $\vec{v}_h \cdot \hat{n} = 0$ on the boundary. Next, the solution of $\psi(x, y)$ is used in equation (2.42) to compute $v_z(x, y)$. This field is used to re-compute $\psi(x, y)$, which is then used to re-compute v_z and so forth. This iterative procedure converges to solutions v_z and ψ which satisfy equations (2.42) and (2.43) and these are the minimum energy fit to the observed magnetic evolution.

Important points to summarize the MEF technique are (Longcope, 2004):

- The MEF method will not yield the actual photospheric velocity but one possible flow field, chosen to be the one with the least overall velocity.
- Applying the method to magnetogram pairs which are obtained from a known velocity field, it was seen that the inferred flow has good overall resemblance to the generating flow, and lower energy. The inferred flow has smaller vertical Poynting and net-mass fluxes than the generating flow.
- The algorithm does not converge in the vicinity of the polarity inversion lines.
- An advantage of the MEF method is that it derives velocity directly from the ideal induction equation on a grid matching that of the magnetic field measurements. Further, MEF has the capability of incorporating partial or imperfect velocity information obtained through independent observations.

2.2 Application of the methods

2.2.1 Active region NOAA 8210

The active region NOAA 8210 was a highly flare-productive active region, crossing over the solar disc from April 28^{th} to May 19^{th} 1998. Its flaring activity on May 1^{st} and May

2^{nd} was extensively studied (Thompson et al., 2000; Warmuth et al., 2000; Pohjolainen et al., 2001; Sterling; Moore, 2001a; Sterling; Moore, 2001b; Sterling et al., 2001; Wang et al., 2002) and the evolution of magnetic field and energetics of this active region was described in detail in (Régnier; Canfield, 2006).

In (Régnier; Canfield, 2006) the evolution of the magnetic field on the photosphere was studied using a long-term movie of Michelson Doppler Imager (MDI, (Scherrer et al., 1995)) 96 min cadence LOS magnetogram observations, as well as by a 1 minute cadence movie around the time of interest. In addition, the photospheric velocity field was derived applying MEF method using Imaging Vector Magnetograph (IVM, (Mickey et al., 1996)) data. The authors suggested two types of horizontal motion that might have driven the observed eruption: a clockwise rotation of the negative sunspot, and a fast motion of an emerging negative polarity. They also suggested that the slow sunspot rotation enables a flare reconnection close to a separatrix surface, whereas the fast motion causes a small-scale reconnection, not detectable.

The photospheric plasma flows responsible for the evolution of the magnetic field in AR8210 were determined using the other methods described in section 2.1. In (Welsch et al., 2004) the flows were computed using IVM vector magnetograms obtained between 17:13 UT and 21:29 UT on May 1^{st} 1998. The methods applied were LCT and ILCT, combined with algebraic decomposition method, and the horizontal and vertical plasma velocities associated to the evolution of the magnetic field were obtained. The IVM vector magnetograms of AR8210 were also used in (Longcope, 2004) to demonstrate the capability of the MEF method. Two independent pairs of vector magnetograms were considered, 18:38 UT/19:09 UT and 19:48 UT/20:19 UT, separated by approximately 30 minutes. Unfortunately, (Welsch et al., 2004) and (Longcope, 2004) used different time intervals and areas around the active region to obtain the velocities, what makes a direct comparison of their results difficult.

In this work a time series of vector magnetic field data taken by the IVM, at the Mees Solar Observatory, is used. The data set was obtained on 1998 May 1^{st} for AR8210 and consist in a time series of 15 time averaged vector magnetograms with an average cadence of 18 minutes, from 17:13 UT to 21:29 UT. The pixel size was originally 1.1" squared but it was resized on a 117 x 112 pixel grid, giving an effective pixel size of 1.77" ($\approx$ 1280 km). This data set was kindly provided to us by Dr. Brian Welsch to compare LCT, ILCT and MEF methods. The goal of this work is to check if the methods are being used correctly and also to apply them to the same region and to the same time interval, allowing, for the first time, a direct comparison of the results obtained using the three different methods. For this active region three different intervals are selected, named as cases (see table

2.1), which corresponds, approximately, to the intervals studied in (Welsch et al., 2004) and (Longcope, 2004). The study performed in (Longcope, 2004) was difficult to reproduce exactly, since the times used here are slightly different and the area chosen by (Longcope, 2004) around AR8210 is not exactly the same.

2.2.1.1 Case 1

In this case, an attempt is made to reproduce the results obtained in (Welsch et al., 2004). Figure 2.1 shows the input data used by the methods to calculate the velocities. The LCT method requires also the size of the window function used to perform the localized cross-correlation (in pixels), the pixel size in centimeters and the time interval in seconds. In addition, ILCT requires a first guess for the horizontal velocity. As in (Welsch et al., 2004), a value of 10 pixels is chosen for the size of the window function. Velocities in regions where $|B_z| < 100$ G and the the magnitude of the velocity is larger than 5 km/s (the photospheric sound speed) are discarded. The LCT results are used as a first guess for the velocity in ILCT. The MEF method is applied on the same data set and the computation of the MEF velocities is performed in two steps: a) a velocity field is calculated without the input of any first guess to the velocity and b) the output of the first step is used as a first guess in the second step, exactly like in (Longcope, 2004).

The velocities calculated using LCT, ILCT and MEF methods, together with the variation of the vertical component of the magnetic field estimated using $\frac{\Delta B_z}{\Delta t} = -\vec{\nabla} \cdot \vec{u}^* B_z$, are presented in Figures 2.2, 2.3 and 2.4, respectively. The velocity u^* represents the output velocity obtained using LCT, ILCT or MEF. The qualitative comparison of the results obtained here using LCT and ILCT with the results obtained in (Welsch et al., 2004) shows that they are similar. This gives confidence that the methods are being applied correctly. The MEF results show local differences compared to the one obtained using LCT and ILCT, what would be expected since the method uses a different approach, but some similarities are still recognizable in the general flow pattern. To have an idea about the distribution of the velocities obtained using the different methods, a histogram of the velocities was calculated (Figure 2.5). From the histogram, it is possible to verify that ILCT and MEF methods obtain larger velocity values than LCT. However, the majority of the velocities are smaller than 1 km/s for the three methods. A quantitative comparison of the variation of the magnetic field LOS component estimated using LCT, ILCT and MEF results with the one calculated using the available data is obtained by means of a cross-correlation between the two data sets. The results are shown in Table 2.2. The correlation analysis is performed in two different cases: considering all the values or discarding the ones where the vertical component of the magnetic field is less than 100 G. The results show that ILCT velocities recover the variation of the vertical component of the magnetic

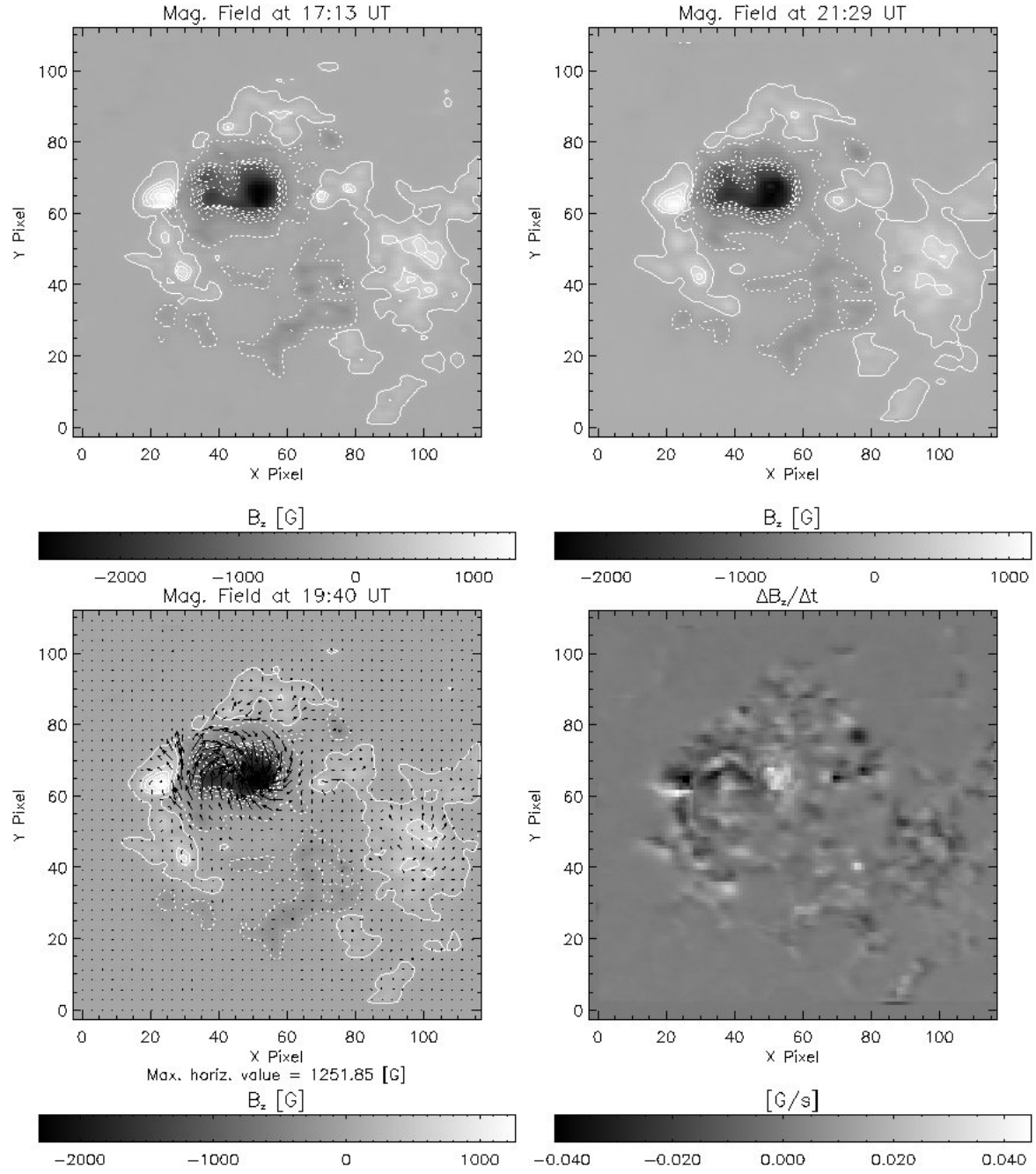

FIGURE 2.1 - Input data used to calculate the velocity fields on May 1^{st} 1998: a) top left- vertical component of the magnetic field obtained at 17:13 UT, b) top right - vertical component of the magnetic field obtained at 21:29 UT, c) bottom left - vector magnetic field obtained at 19:40 UT and d)bottom right - variation of the vertical component of the magnetic field between 17:13 UT and 21:29 UT. The gray scale represents the intensity or the variation of the LOS component of the magnetic field. The arrows represent the horizontal component of the magnetic field, with the largest length of the arrow associated to the maximum horizontal value measured for the magnetic field. The contour lines are drawn for the magnetic field modulus equal to 100, 500, 700, 900, 1100 and 1300 G.

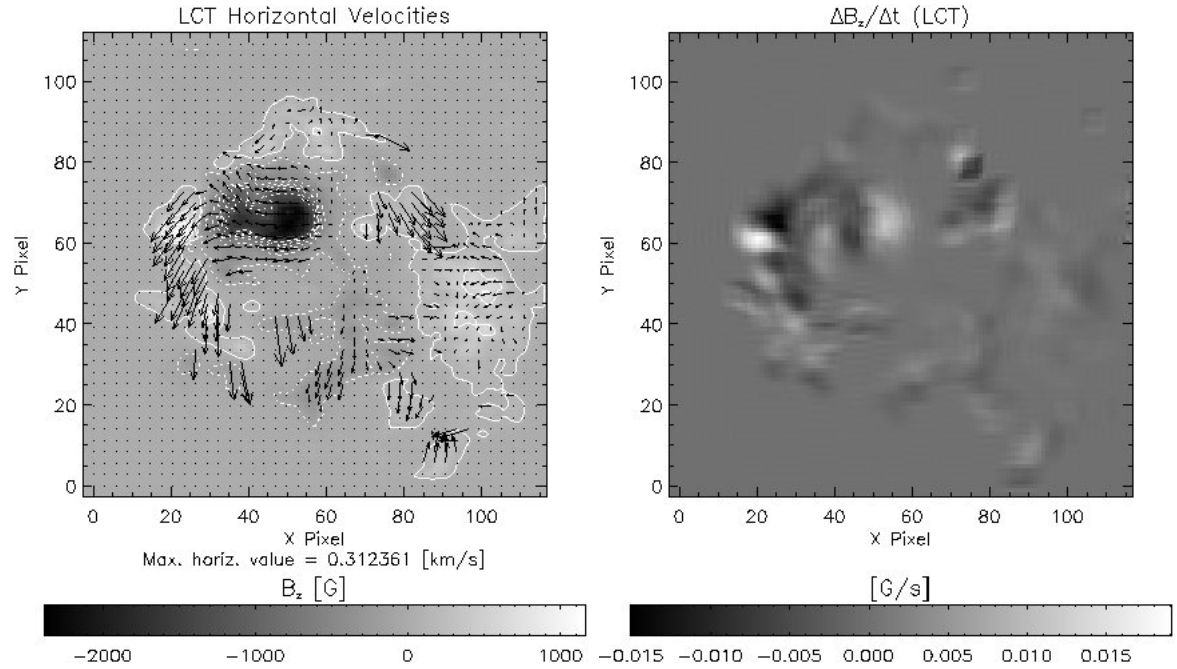

FIGURE 2.2 - Horizontal velocity obtained using LCT method (left) and the variation of the vertical component calculated using $\frac{\Delta B_z}{\Delta t} = -\vec{\nabla} \cdot (u^{(LCT)} B_z)$ (right). The gray scale represents the intensity or the variation of the LOS component of the magnetic field. The arrows represent the horizontal component of the velocity, with the largest length of the arrow associated to the maximum horizontal value measured for the velocity. The contour lines are drawn for the magnetic field magnitude equal to 100, 500, 700, 900, 1100 and 1300 G.

field more accurately than LCT or MEF velocities.

In summary, the results of this part of the dissertation are:

a) LCT and ILCT are applied correctly, our results match those obtained in (Welsch et al., 2004).

b) The comparison between the output of three methods show that the velocities obtained present local differences while some similarities are recognizable in the general flow pattern.

c) Generally, ILCT and MEF obtain velocity values larger than LCT.

d) The ILCT method recovers the variation of the vertical component of the magnetic field more accurately than LCT and MEF.

2.2.1.2 Case 2

In this section an attempt to reproduce the results obtained in (Longcope, 2004) is made. However, two problems immediately appear: 1) the same time interval is not available in

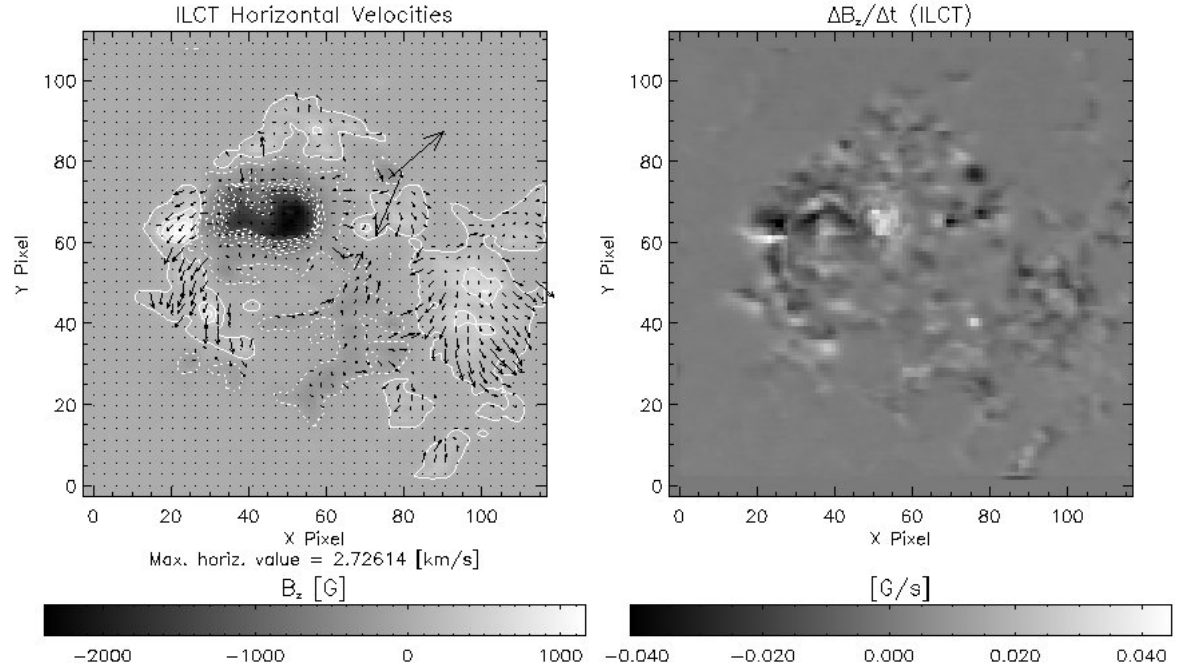

FIGURE 2.3 - Velocity obtained using ILCT method(left) and the variation of the vertical component calculated using $\frac{\Delta B_z}{\Delta t} = -\vec{\nabla} \cdot (u^{(ILCT)} B_z)$ (right). The gray scale represents the intensity or the variation of the LOS component of the magnetic field. The arrows represent the horizontal component of the velocity, with the largest length of the arrow associated to the maximum horizontal value measured for the velocity. The contour lines are drawn for the magnetic field magnitude equal to 100, 500, 700, 900, 1100 and 1300 G.

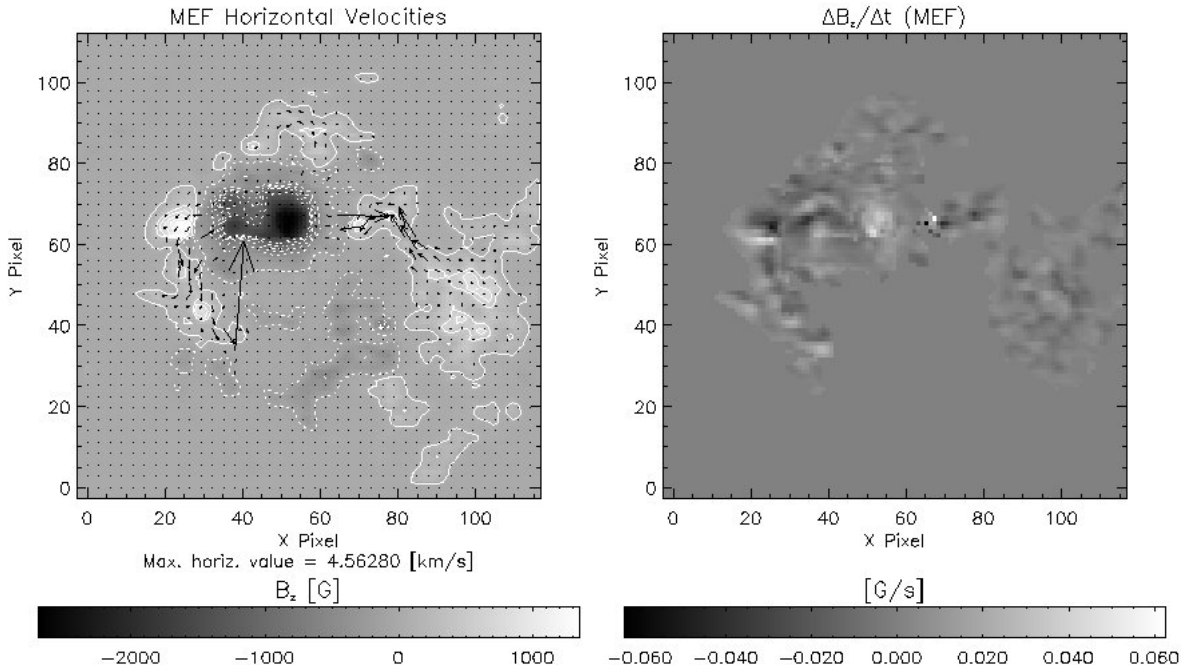

FIGURE 2.4 - Velocity obtained using MEF method (left) and the variation of the vertical component calculated using $\frac{\Delta B_z}{\Delta t} = -\vec{\nabla} \cdot (u^{(MEF)} B_z)$ (right). The gray scale represents the intensity or the variation of the LOS component of the magnetic field. The arrows represent the horizontal component of the velocity, with the largest length of the arrow associated to the maximum horizontal value measured for the velocity. The contour lines are drawn for the magnetic field magnitude equal to 100, 500, 700, 900, 1100 and 1300 G.

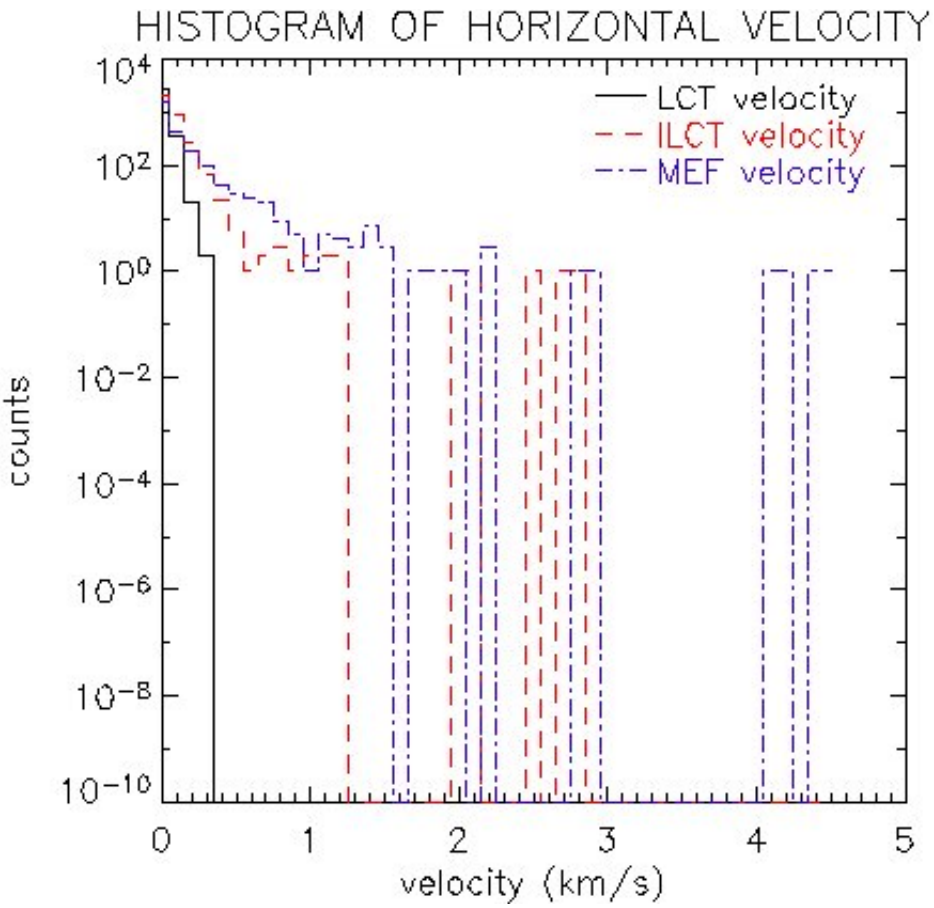

FIGURE 2.5 - Histogram showing the distribution of velocities obtained with LCT, ILCT and MEF. Velocities larger than 5km/s and in regions where the magnetic field is less than 100G were discarded.

the IVM data and 2) it is impossible to select exactly the same area analyzed. Hence, we selected the closest possible interval and more or less the same area. Results close to those obtained by (Longcope, 2004) are expected since the characteristic time of the evolution of an active regions spans from hours to days and the difference in time between the data sets is of the order of minutes.

As it was mentioned before, intervals close to those studied in (Longcope, 2004) are used and they are classified as cases 2A and 2B (see Table 2.1). Figure 2.6 shows the input data for case 2A. The window function used in LCT is 10 pixels and the velocities with modulus greater than 5 km/s or where $|B_z| < 100$ G are discarded. The results obtained using LCT, ILCT and MEF, together with the magnetic field variation estimated using them, are shown in Figures 2.7, 2.8 and 2.9, respectively. The use of a shorter time interval and a smaller area around the active region influences the results obtained. This is evident when these results are compared with those described in the previous section. Basically, the same general flow patterns are present in both results. However, the 10 pixel size of the window function used in LCT is not sufficient to produce a detailed velocity pattern.

The LCT results reveal clearly a southward motion of the positive polarity, but not the rotation of the negative polarity. The velocity pattern obtained with ILCT shows much more details in terms of small scale changes in the velocity. The ILCT results reveals a clockwise rotation of the negative polarity, a southward motion of the positive polarity and a clear motion of the magnetic polarities away from the polarity inversion line. The results obtained using MEF also show a detailed velocity pattern with small scale changes in the flow. Even if the general flow pattern is very similar to that obtained by ILCT, it presents some significant differences like the inversion of the flow pattern of the positive polarity from southward to northward in the lower left part of Figure 2.9. Also, the rotation of the negative polarity and the motion away from the polarity inversion line are not so clear in the MEF results. The distribution of the velocities is presented in the histogram in Figure 2.10. It shows that ILCT and MEF obtain larger velocity values than LCT, but the majority of the velocities are smaller than 1 km/s. The cross-correlation (Table 2.2) between the variation of the vertical component of the magnetic field obtained using the available data and that estimated using $\frac{\Delta B_z}{\Delta t} = -\vec{\nabla} \cdot \vec{u}^* B_z$ shows that ILCT velocities reproduce the variation of the vertical component of the magnetic field with more accuracy than LCT and MEF.

Figure 2.11 depicts the input data for case 2B. The velocities obtained using LCT, ILCT and MEF are presented in Figures 2.12, 2.13 and 2.14, respectively. The velocity pattern obtained by LCT shows clearly the southward motion of the positive polarity. However, the method is not able to capture the clockwise motion of the negative polarity. The velocity pattern obtained by ILCT presents small scale changes in the flow that are not present in LCT results. There are local differences when comparing with the results obtained by ILCT in case 2A, but the general flow pattern is still present. The positive polarity is moving southward and eastward, the negative polarity is rotating clockwise and both, positive and negative polarities, are moving away from the polarity inversion line. The MEF result is very similar to the one obtained in case 2A. The distribution of velocities (Figure 2.15) shows that ILCT and MEF methods produce velocities larger than LCT. However, the majority of the velocities are smaller than 1 km/s. The variation of the vertical component of the magnetic field displayed with the velocity results is quantitatively compared with the one calculated using the magnetic field data by means of a cross-correlation coefficient, displayed in Table 2.2. The results show that ILCT velocities reproduce the variation of the vertical component with higher accuracy than LCT and MEF.

For a better comparison with the results in (Longcope, 2004) for MEF method, the velocity was calculated again using a cutoff value for the magnetic field of 60 G. The resulting

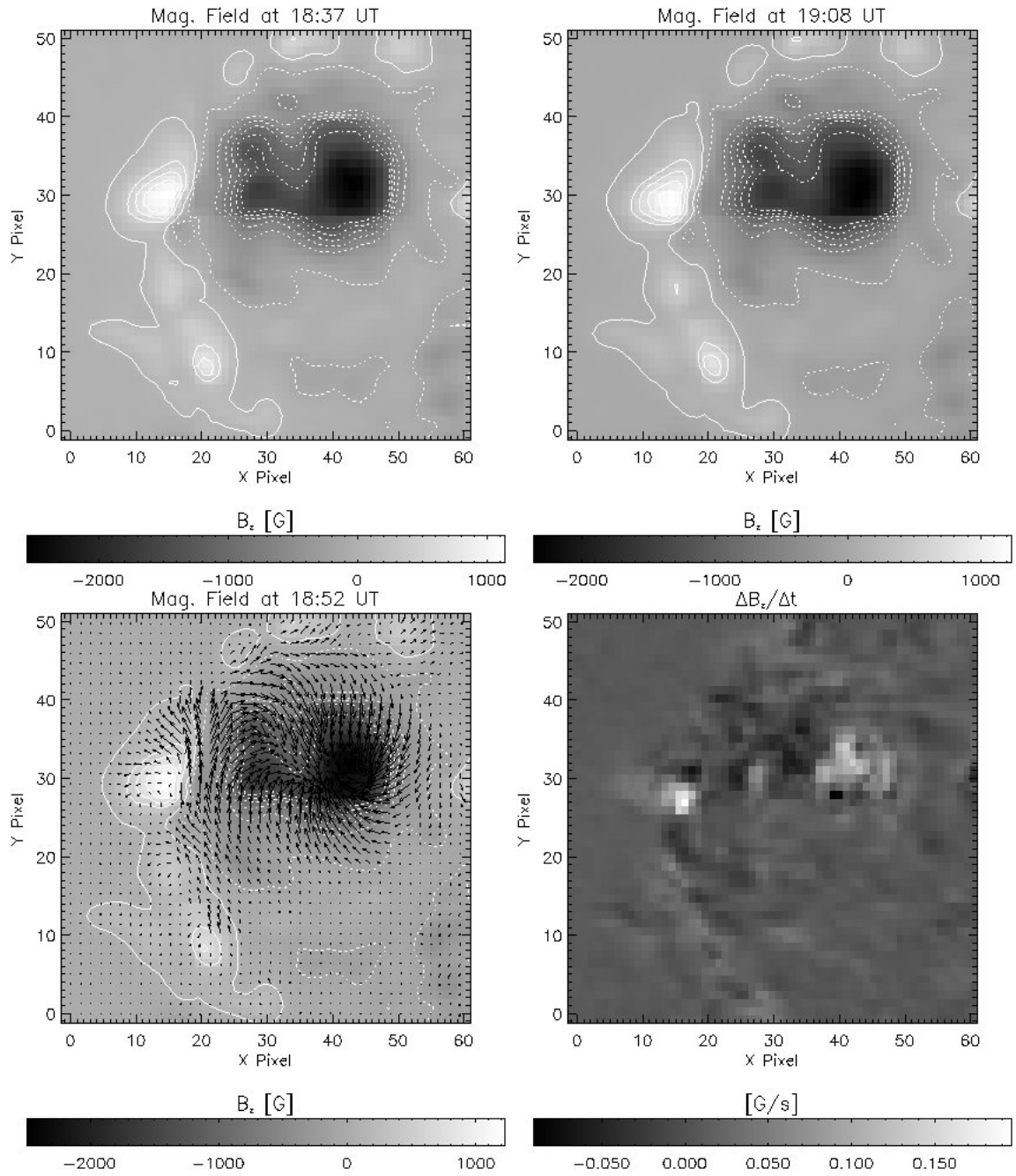

FIGURE 2.6 - Input data used to calculate the velocity fields on May 1^{st} 1998: a) top left- vertical component of the magnetic field obtained at 18:37 UT, b) top right - vertical component of the magnetic field obtained at 19:08 UT, c) bottom left - vector magnetic field obtained at 18:52 UT and d)bottom right - variation of the vertical component of the magnetic field between 18:37 UT and 19:08 UT. The gray scale represents the intensity or the variation of the LOS component of the magnetic field. The arrows represent the horizontal component of the magnetic field, with the largest length of the arrow associated to the maximum horizontal value measured for the magnetic field. The contour lines are drawn for the magnetic field magnitude equal to 300, 500, 700, 900, 1100 and 1300 G.

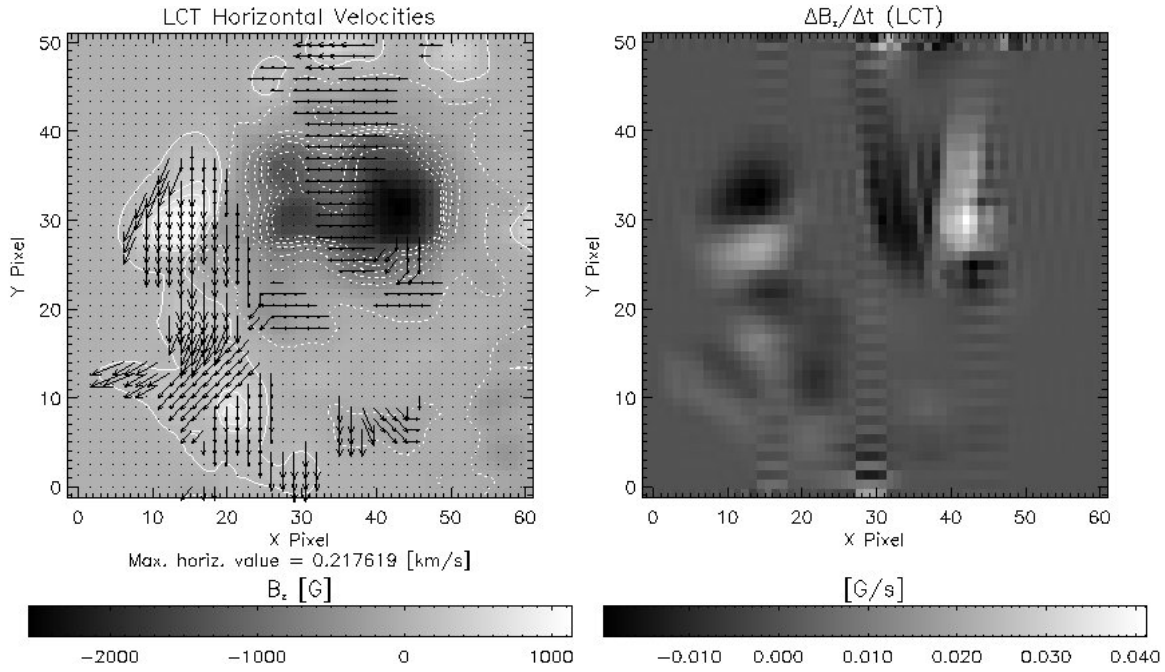

FIGURE 2.7 - Velocity obtained using LCT method (left) and the variation of the vertical component calculated using $\frac{\Delta B_z}{\Delta t} = -\vec{\nabla} \cdot (u^{(LCT)} B_z)$ (right). The gray scale represents the intensity or the variation of the LOS component of the magnetic field. The arrows represent the horizontal component of the velocity, with the largest length of the arrow associated to the maximum horizontal value measured for the velocity. The contour lines are drawn for the magnetic field magnitude equal to 300, 500, 700, 900, 1100 and 1300 G.

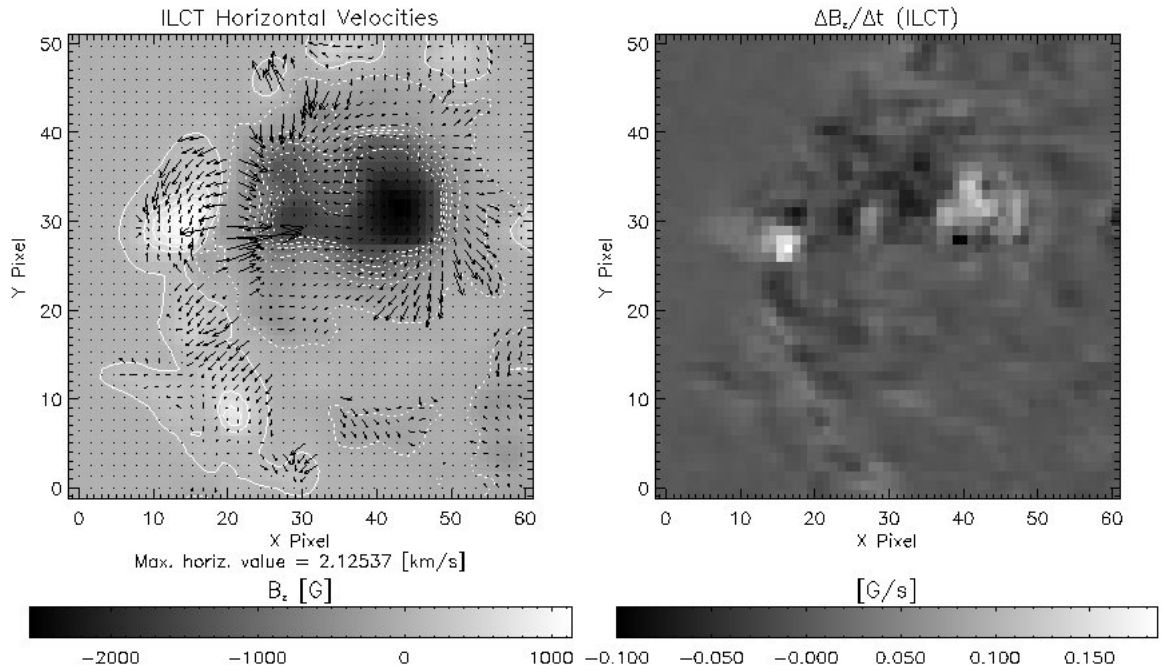

FIGURE 2.8 - Velocity obtained using ILCT method(left) and the variation of the vertical component calculated using $\frac{\Delta B_z}{\Delta t} = -\vec{\nabla} \cdot (u^{(ILCT)} B_z)$ (right). The gray scale represents the intensity or the variation of the LOS component of the magnetic field. The arrows represent the horizontal component of the velocity, with the largest length of the arrow associated to the maximum horizontal value measured for the velocity. The contour lines are drawn for the magnetic field magnitude equal to 300, 500, 700, 900, 1100 and 1300 G.

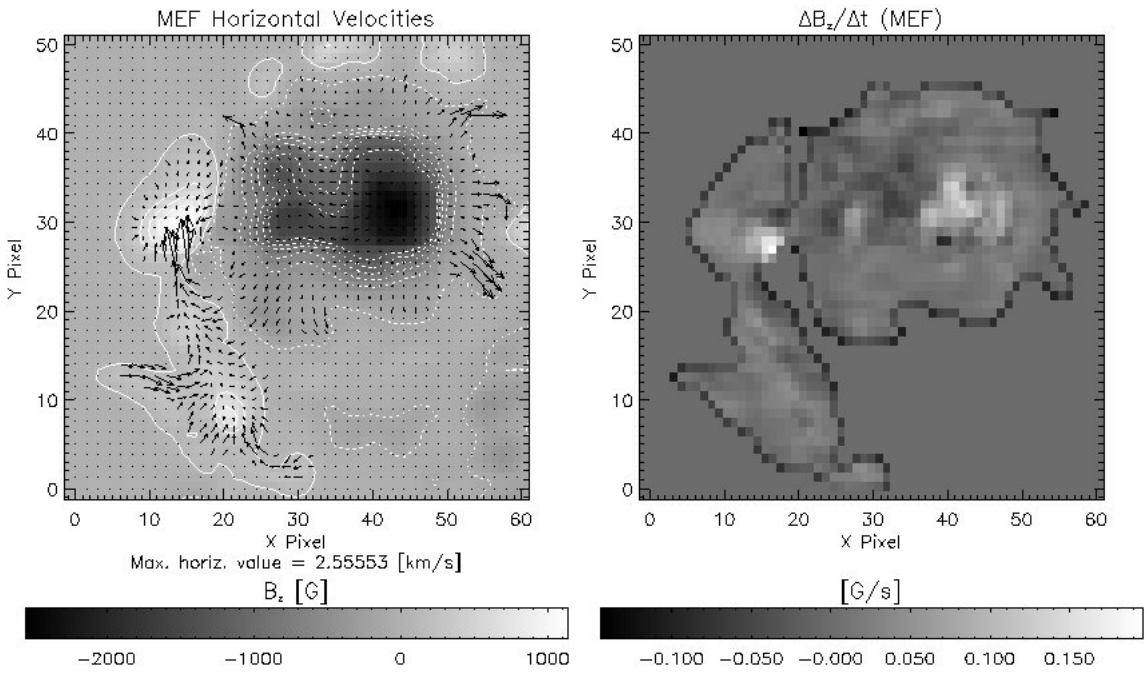

FIGURE 2.9 - Velocity obtained using MEF method (left) and the variation of the vertical component calculated using $\frac{\Delta B_z}{\Delta t} = -\vec{\nabla} \cdot (u^{(MEF)} B_z)$ (right). The gray scale represents the intensity or the variation of the LOS component of the magnetic field. The arrows represent the horizontal component of the velocity, with the largest length of the arrow associated to the maximum horizontal value measured for the velocity. The contour lines are drawn for the magnetic field magnitude equal to 300, 500, 700, 900, 1100 and 1300 G.

horizontal and vertical velocities obtained by MEF for cases 2A and 2B are displayed in Figure 2.16. These results present local differences when compared with those obtained in (Longcope, 2004) and even flows in the opposite direction occur. This can be due the fact that the flows change when different time intervals were used, even if the difference between the intervals is much less than the characteristic time of the evolution of an active region.

In summary, the results of this section show that:

a) The use of shorter time interval and a smaller area around the active region affects the results obtained by LCT at smaller scales. However, the general flow pattern remains as shown by comparison with case 1.

b) ILCT and MEF methods are able to resolve small scale changes in the flow that are not present in LCT.

c) However, MEF results may locally considerably differ from those obtained by ILCT, revealing even opposite flow direction in some small regions.

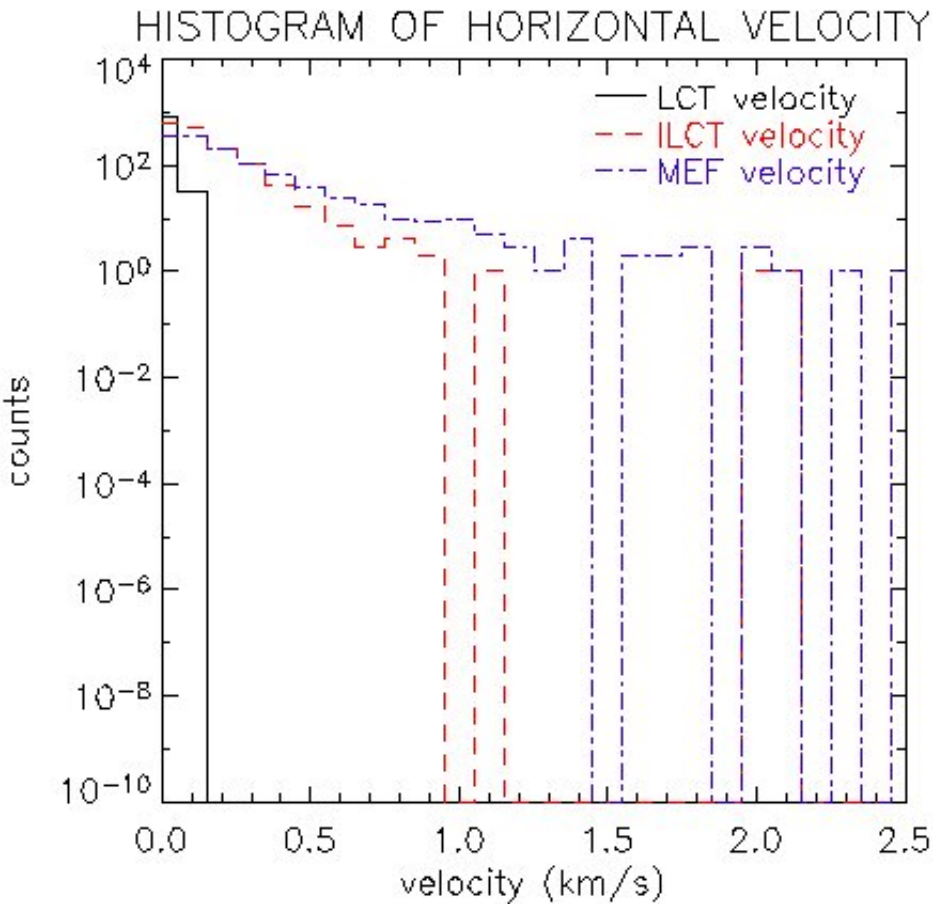

FIGURE 2.10 - Histogram showing the distribution of velocities obtained with LCT, ILCT and MEF. Velocities larger than 5km/s and in regions where the magnetic field is less than 100G were discarded.

d) Velocities, obtained by ILCT and MEF methods are larger than those, obtained by using just LCT.

e) ILCT results recover the variation of the vertical component of the magnetic field more accurately than LCT or MEF.

f) Our test results obtained using the MEF method do not very well agree with those obtained in (Longcope, 2004). This is, perhaps, due to the fact that the flows change during different intervals, even if the difference between the intervals is of just some minutes.

2.3 Conclusions

Different methods to calculate the (photospheric) plasma velocity from (photospheric) magnetic field observations were, for the first time, all applied to the same area and time interval. We found that the velocity fields obtained by the different methods contain local differences. However, a similar general flow pattern can still be recognized in the results.

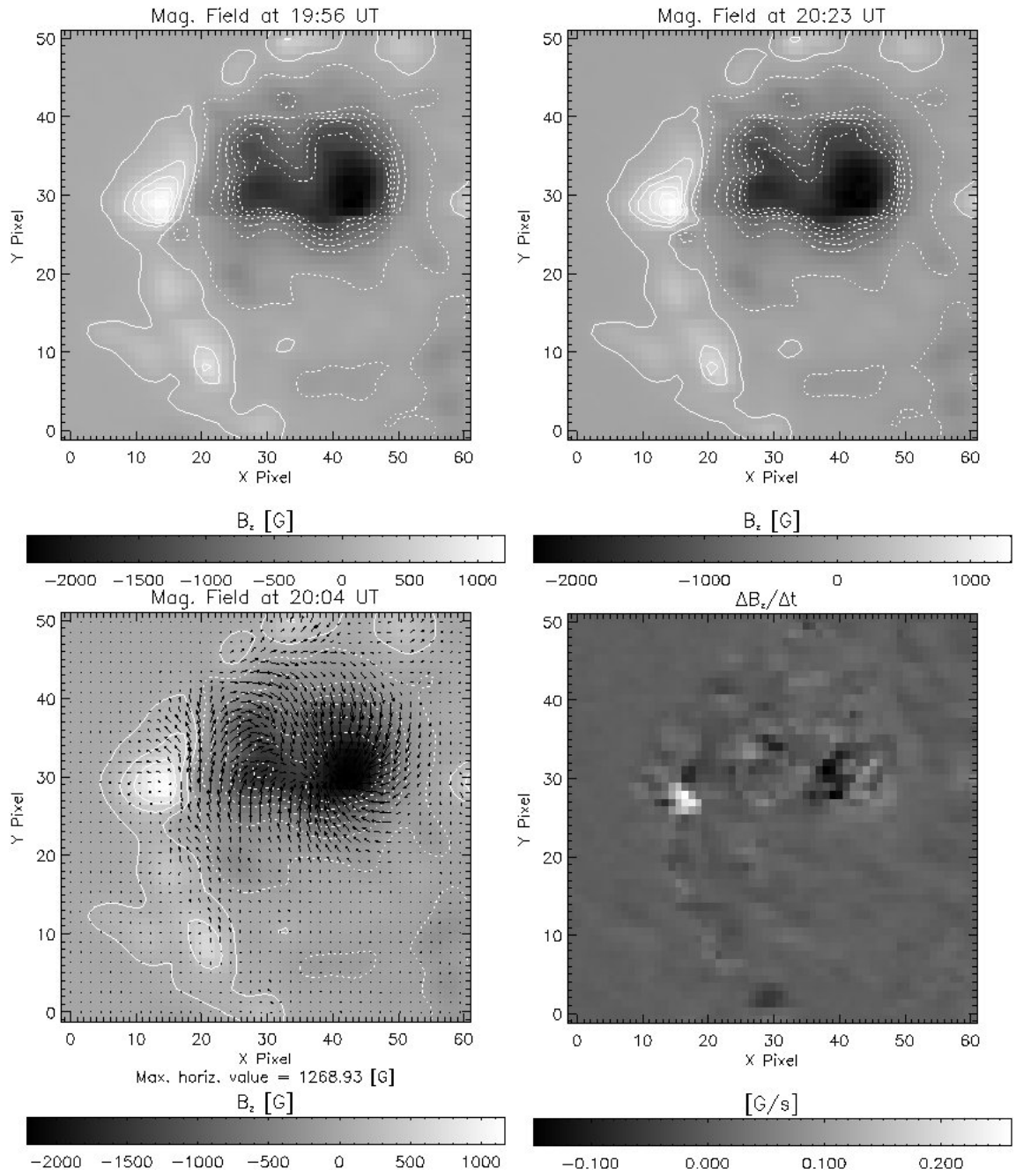

FIGURE 2.11 - Input data used to calculate the velocity fields on May 1^{st} 1998: a) top left- vertical component of the magnetic field obtained at 19:56 UT, b) top right - vertical component of the magnetic field obtained at 20:23 UT, c) bottom left - vector magnetic field obtained at 20:11 UT and d)bottom right - variation of the vertical component of the magnetic field between 19:56 UT and 20:23 UT. The gray scale represents the intensity or the variation of the LOS component of the magnetic field. The arrows represent the horizontal component of the magnetic field, with the largest length of the arrow associated to the maximum horizontal value measured for the magnetic field. The contour lines are drawn for the magnetic field magnitude equal to 300, 500, 700, 900, 1100 and 1300 G.

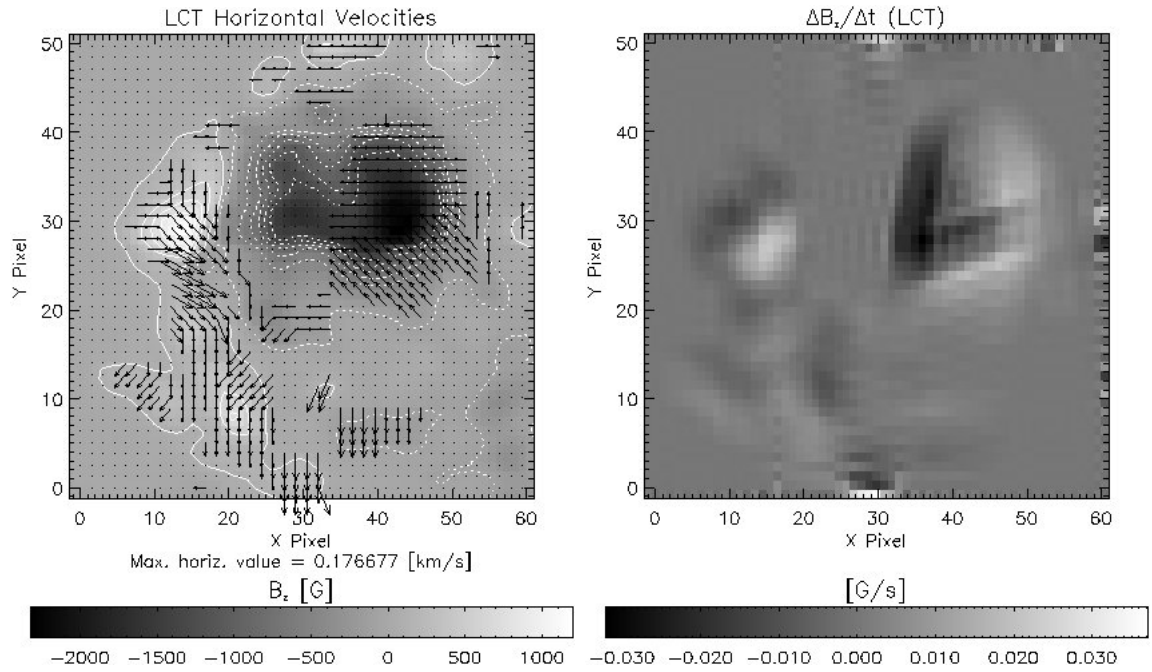

FIGURE 2.12 - Velocity obtained using LCT method (left) and the variation of the vertical component calculated using $\frac{\Delta B_z}{\Delta t} = -\vec{\nabla} \cdot (u^{(LCT)} B_z)$ (right). The gray scale represents the intensity or the variation of the LOS component of the magnetic field. The arrows represent the horizontal component of the velocity, with the largest length of the arrow associated to the maximum horizontal value measured for the velocity. The contour lines are drawn for the magnetic field magnitude equal to 300, 500, 700, 900, 1100 and 1300 G.

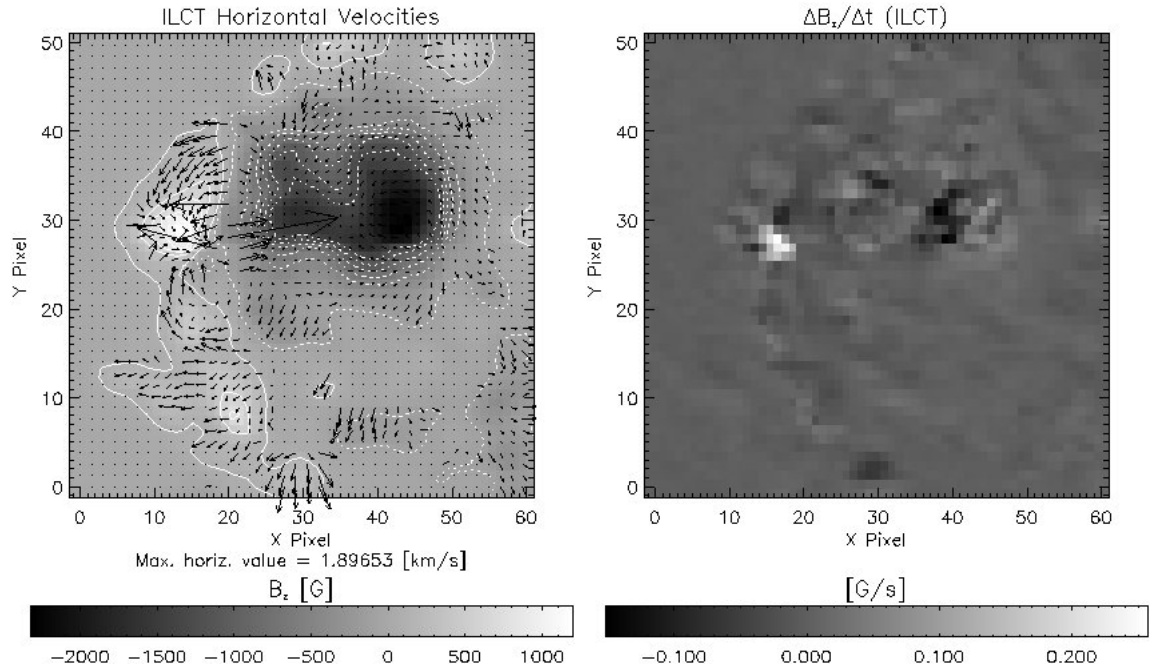

FIGURE 2.13 - Velocity obtained using ILCT method(left) and the variation of the vertical component calculated using $\frac{\Delta B_z}{\Delta t} = -\vec{\nabla} \cdot (u^{(ILCT)} B_z)$ (right). The gray scale represents the intensity or the variation of the LOS component of the magnetic field. The arrows represent the horizontal component of the velocity, with the largest length of the arrow associated to the maximum horizontal value measured for the velocity. The contour lines are drawn for the magnetic field magnitude equal to 300, 500, 700, 900, 1100 and 1300 G.

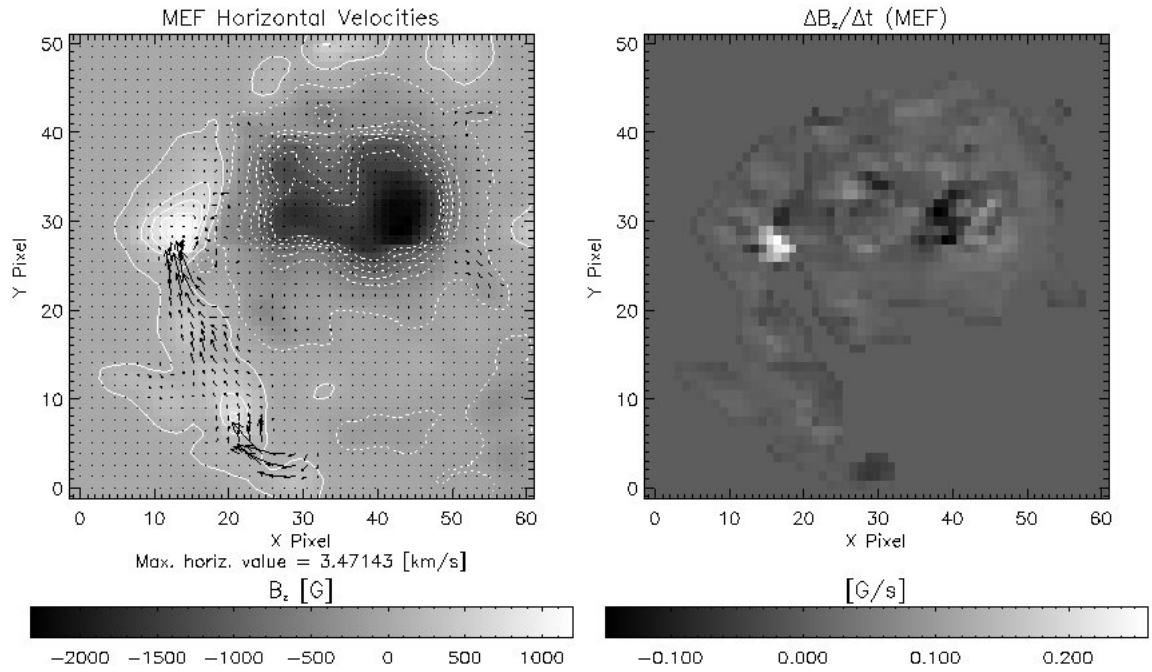

FIGURE 2.14 - Velocity obtained using MEF method (left) and the variation of the vertical component calculated using $\frac{\Delta B_z}{\Delta t} = -\vec{\nabla} \cdot (u^{(MEF)} B_z)$ (right). The gray scale represents the intensity or the variation of the LOS component of the magnetic field. The arrows represent the horizontal component of the velocity, with the largest length of the arrow associated to the maximum horizontal value measured for the velocity. The contour lines are drawn for the magnetic field magnitude equal to 300, 500, 700, 900, 1100 and 1300 G.

TABLE 2.1 - Different data intervals used to calculate the velocity responsible for the evolution of AR8210.

case	initial time (UT)	final time (UT)	intermediate time (UT)	Δt (s)
1	17:13	21:29	19:40	15360
2A	18:37	19:08	18:52	1860
2B	19:56	20:23	20:11	1620

TABLE 2.2 - Results for AR8210: the cross-correlation between the variation of the vertical component of the magnetic field per unit of time calculated with the available data and the one obtained using the approximation $\frac{\Delta B_z}{\Delta t} = -\vec{\nabla} \cdot (u^* B_z)$. Here u^* represents the velocities obtained using the different methods (LCT, ILCT and MEF).

case	method	correlation	correlation ($\lvert B_z \rvert > 100G$)
1	LCT	0.62	0.65
	ILCT	1.00	1.00
	MEF	0.83	0.87
2A	LCT	0.44	0.42
	ILCT	1.00	0.96
	MEF	0.71	0.78
2B	LCT	0.33	0.32
	ILCT	1.00	1.00
	MEF	0.94	0.96

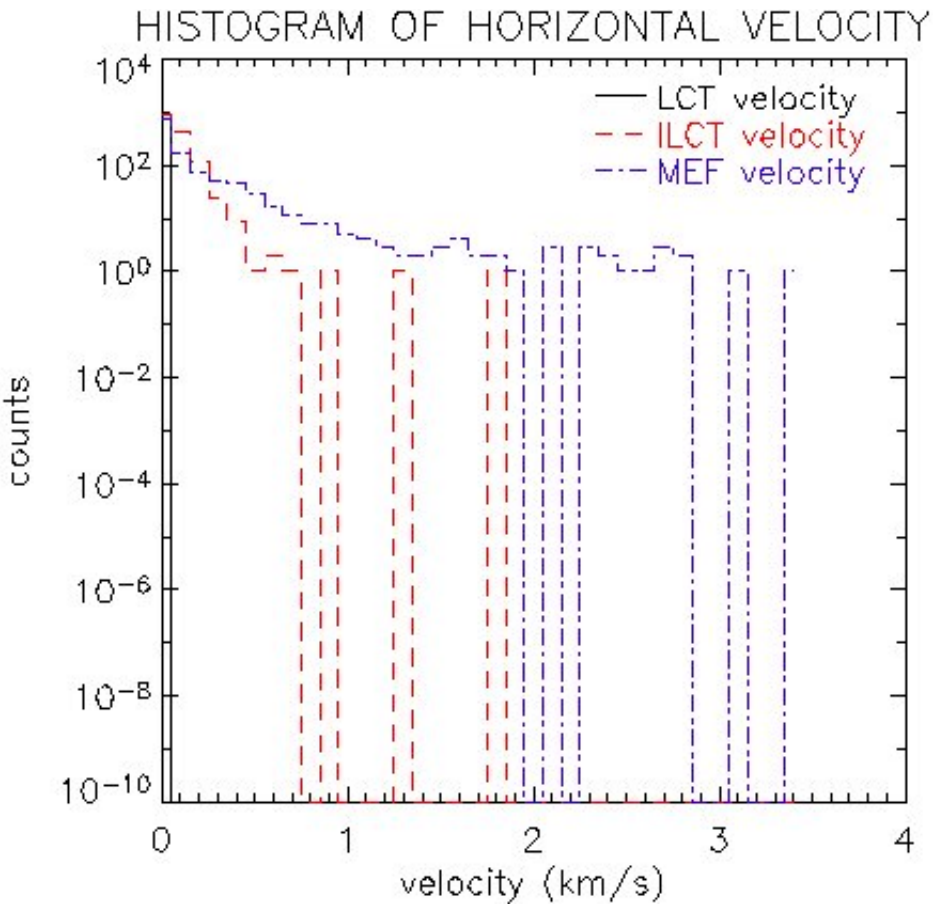

FIGURE 2.15 - Histogram showing the distribution of velocities obtained with LCT, ILCT and MEF. Velocities larger than 5km/s and in regions where the magnetic field is less than 100G were discarded.

For AR8210 this general flow pattern consists of a rotation of the negative polarity and a motion of the positive polarity, part of it southward and part of it northward or eastward.

When using the photospheric magnetic field observations, there are two different situations that must be considered: when only the information about the LOS component of the magnetic field is available or when the full vector magnetic field is known. The first situation is typical when MDI data is used. Since MDI gives only the LOS component of the photospheric magnetic field ILCT and MEF cannot be used to infer the plasma velocity responsible for the evolution of the magnetic features, and the method used will be LCT. The second situation applies for data obtained by vector magnetographs. When vector magnetograms are available the three methods can be applied and the full velocity field can be obtained. Due to its simplicity and the accuracy in recovering the variation of the vertical component of the photospheric magnetic field, the preferred method to be used will be ILCT. However, at the moment it is difficult to decide which method is the best one, since there is no information about the original plasma velocity responsible for the evolution of the magnetic features to be compared.

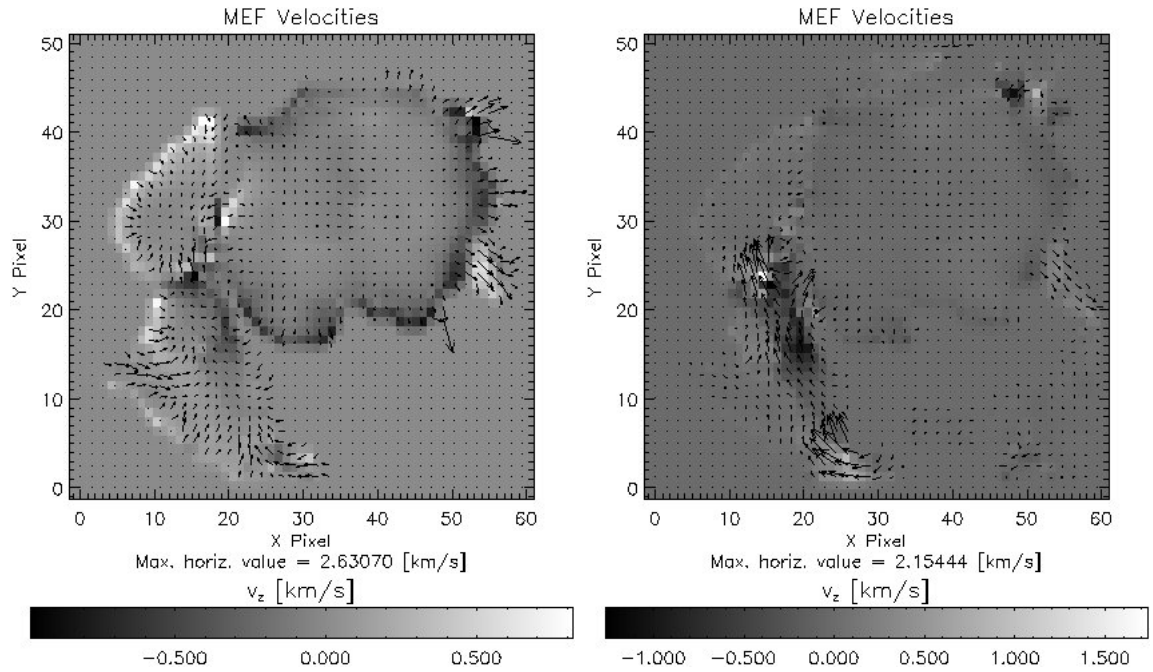

FIGURE 2.16 - Velocity obtained using MEF method for case 2A (left) and for case 2B (right). The gray scale depicts the vertical velocity and the arrows represent the horizontal component of the velocity, with the largest length of the arrow associated to the maximum horizontal value measured for the velocity.

3 THE NUMERICAL SIMULATION MODEL

The objective of the present work is to study the effects of horizontal photospheric plasma motion on the evolution of plasma and magnetic fields in the solar atmosphere, in regions of observed Extreme-UltraViolet (EUV) and X-ray Bright Points (BPs). To perform this work a 'data driven' three dimensional (3D) magnetohydrodynamic (MHD) model is used (Büchner et al., 2004a). The novelty of this model is the capability of combining numerical simulation with observations, by using the photospheric magnetic field measurements to obtain an initial configuration for the magnetic field and the photospheric horizontal plasma motion as a boundary condition of the model. The system starts from an observation based initial condition and evolves by the solution of an appropriate set of MHD equations in a 3D cartesian system using finite difference discretization methods. The simulation volume is characterized by six boundaries and the plasma motion is applied at the bottom boundary, but it is effective in the photosphere and chromosphere via momentum exchange with a moving neutral gas.

In this chapter a description of the model is given. The chapter is organized as follows: in section 3.1 the basic assumptions of MHD are described; in section 3.2 the set of MHD equations solved in the numerical simulation is presented; in section 3.3 the initial conditions are discussed; in section 3.4 the boundary conditions used in the 3D simulation box are presented; in section 3.5 the normalization parameters are presented; in section 3.6 the set of normalized MHD equations is described; and in section 3.7 the numerical simulation approach is detailed.

3.1 Basic assumptions of magnetohydrodynamics

The MHD approximation is an appropriate way of describing the large scale plasma motion and its interaction with magnetic fields. The MHD theory combines the equations of hydrodynamics with the Maxwell equations. In the MHD theory the following assumptions are made:

a) The fluid motion is non-relativistic, i.e.

$$\frac{V}{c} \ll 1 \tag{3.1}$$

and under change of the reference frame $\vec{E}$ and $\vec{B}$ transform according to

$$\vec{E}' = \vec{E} + \frac{1}{c}\vec{v} \times \vec{B} \tag{3.2}$$

$$\vec{B}' = \vec{B} - \frac{1}{c}\vec{v} \times \vec{E}, \tag{3.3}$$

where $\vec{v}$ is the relative velocity between the two frames of reference.

b) If L and T are the typical spatial and temporal scales at which a quantity changes, then

$$\frac{L/T}{c} \ll 1 \tag{3.4}$$

holds. This implies, e.q. that all phase velocities are non-relativistic. Hence, electromagnetic waves do not occur in MHD.

c) The plasma is assumed to be highly conductive and charge-neutral. In a plasma, charge neutrality is valid as long as spatial and temporal scales under consideration are much larger than the Debye length $\lambda_D = (kT/8\pi n_e e^2)^{1/2}$ and the inverse plasma frequency $\omega_p^{-1} = (m_e/4\pi e^2 n_e)^{1/2}$, respectively.

These assumptions bear the following properties of the MHD approach. Electric fields due to charge separation are negligible. This follows from an order-of-magnitude estimate of the Faraday equation, which governs the electric field in the absence of free charges:

$$\begin{aligned} \vec{\nabla} \times \vec{E} = -\frac{1}{c}\frac{\partial \vec{B}}{\partial t} \Rightarrow \\ \frac{E}{L} \approx \frac{B}{cT} \Rightarrow \\ \frac{E}{B} \approx \frac{L}{cT} \ll 1. \end{aligned} \tag{3.5}$$

From Ampère's law an estimate of the displacement current yields

$$\frac{\dot{\vec{E}}/c}{\vec{\nabla} \times \vec{B}} \approx \frac{E/T}{cB/L} \approx \frac{E}{B}\frac{L}{cT} \approx \left(\frac{E}{B}\right)^2 \ll 1, \tag{3.6}$$

where $\dot{\vec{E}} = \frac{\partial \vec{E}}{\partial t}$.

As a consequence, the displacement current can be neglected in the Ampère's law which can be rewritten as

$$\vec{\nabla} \times \vec{B} = \frac{4\pi}{c}\vec{j}. \tag{3.7}$$

Likewise, the $\vec{v} \times \vec{E}$ term disappears from equation (3.3). This follows from

$$\frac{\vec{v} \times \vec{E}}{c|\vec{B}|} \approx \frac{V}{c}\frac{E}{B} \ll 1. \tag{3.8}$$

Hence, the transformation law for the magnetic field reads

$$\vec{B}' = \vec{B} \tag{3.9}$$

Taking into account this transformation and the new form of Ampère's law, the transformation of the electric current is given by

$$\begin{aligned} \vec{\nabla} \times \vec{B}' &= \frac{4\pi}{c}\vec{j}' \Rightarrow \\ \vec{\nabla} \times \vec{B} &= \frac{4\pi}{c}\vec{j}' \Rightarrow \\ \frac{4\pi}{c}\vec{j} &= \frac{4\pi}{c}\vec{j}' \Rightarrow \\ \vec{j} &= \vec{j}' \end{aligned} \tag{3.10}$$

Using the previous relations, the Ohm's law in a moving reference frame can be written as

$$\vec{j} = \sigma(\vec{E} + \frac{1}{c}\vec{v} \times \vec{B}). \tag{3.11}$$

The equation that governs the temporal evolution of the magnetic field can be obtained from the previous equation by taking its curl and substituting $\vec{j}$ and $\vec{\nabla} \times \vec{E}$ from the Ampère and Faraday's laws, respectively.

$$\begin{aligned} \vec{\nabla} \times \vec{j} &= \sigma\Big[\vec{\nabla} \times \vec{E} + \frac{1}{c}\vec{\nabla} \times (\vec{v} \times \vec{B})\Big] \Rightarrow \\ \vec{\nabla} \times \Big(\frac{c}{4\pi}\vec{\nabla} \times \vec{B}\Big) &= \sigma\Big[-\frac{1}{c}\frac{\partial \vec{B}}{\partial t} + \frac{1}{c}\vec{\nabla} \times (\vec{v} \times \vec{B})\Big] \Rightarrow \\ \frac{\partial \vec{B}}{\partial t} &= \vec{\nabla} \times (\vec{v} \times \vec{B}) - \vec{\nabla} \times \Big(\frac{c^2}{4\pi\sigma}\vec{\nabla} \times \vec{B}\Big) \Rightarrow \\ \frac{\partial \vec{B}}{\partial t} &= \vec{\nabla} \times (\vec{v} \times \vec{B}) - \vec{\nabla} \times \Big(\eta\vec{\nabla} \times \vec{B}\Big), \end{aligned} \tag{3.12}$$

where $\eta = \frac{c^2}{4\pi\sigma}$ is the magnetic resistivity (diffusivity). Equation (3.12) is called the induction equation of resistive MHD. The first term of its right-hand-side describe the inductive effect of the velocity field, and the second term accounts for diffusion of magnetic field due to the finite conductivity of the plasma.

In most of the plasmas, including the plasma of the solar atmosphere, the resistivity is very low and the second term in the right-hand-side of the induction equation can be discarded. In this case the MHD approach to the plasma is called "ideal". A direct consequence of plasma ideality is that the magnetic field evolution is governed by the motion of the plasma alone. In other words, the magnetic field is advected together with the plasma

(frozen-in-theorem). This makes possible to store energy in the magnetic field by moving the fluid or the source of the magnetic field. The energy can then become available if the conditions for ideal MHD break down, allowing processes that releases the stored energy from the magnetic field.

In an imperfectly conducting (resistive) fluid, the magnetic field can generally move through the fluid, following a diffusion law with the resistivity of the plasma serving as a diffusion constant. Even in physical systems which are large and conductive enough that rare collisions suggest that the resistivity can be ignored, resistivity may still be important: micro-instabilities can increase the effective resistivity of the plasma by factors of more than a billion. The enhanced resistivity is usually the result of the formation of small scale structure like current sheets or fine scale magnetic turbulence. They introduce small spatial scales into the system at which the ideal MHD conditions are violated and magnetic diffusion can occur quickly. When this happens, magnetic reconnection may occur in the plasma which releases stored magnetic energy as waves, bulk mechanical acceleration of material, particle acceleration, and heat. Magnetic reconnection in highly conductive systems is important because it releases concentrated energy at short times, so that gentle forces applied to a plasma for long periods of time can cause violent explosions and bursts of radiation.

3.2 Basic equations

The MHD model solves the following set of MHD equations

$$\frac{\partial \rho}{\partial t} = -\vec{\nabla} \cdot \rho\vec{u}, \tag{3.13}$$

$$\frac{\partial \rho\vec{u}}{\partial t} = -\vec{\nabla} \cdot \rho\vec{u}\vec{u} - \vec{\nabla}p + \vec{j} \times \vec{B} - \nu\rho(\vec{u} - \vec{u}_0), \tag{3.14}$$

$$\frac{\partial \vec{B}}{\partial t} = \vec{\nabla} \times (\vec{u} \times \vec{B} - \eta\vec{j}), \tag{3.15}$$

$$\frac{\partial p}{\partial t} = -\vec{\nabla} \cdot p\vec{u} - (\gamma - 1)p\vec{\nabla} \cdot \vec{u} + (\gamma - 1)\eta j^2, \tag{3.16}$$

together with Ohm's law, Àmpere's law and an equation of state

$$\vec{E} = -\vec{u} \times \vec{B} + \eta\vec{j}, \tag{3.17}$$

$$\vec{\nabla} \times \vec{B} = \mu_0\vec{j}, \tag{3.18}$$

$$p = 2n\kappa_B T. \tag{3.19}$$

In these equations ρ is the plasma density, $\vec{u}$ is the plasma velocity, $\vec{B}$ is the magnetic field, p is the thermal pressure and T is the plasma temperature. The quantity $\vec{u}_0$ denotes the velocity of a neutral gas to which the plasma is coupled at least in the chromosphere and photosphere.

In the momentum equation (3.14) the collision term, the last term in the right-hand-side, describes the transfer of momentum between the neutral gas and the plasma, ν represents the collision frequency between the neutrals and plasma. In the solar photosphere and chromosphere the collision frequency is large compared to the inverse of the Alfvén time, hence, one can use a value for this frequency that is larger than the inverse of the Alfvén time to couple the plasma in the chromosphere strongly to the neutral gas. In the solar corona the density is much smaller, hence plasma and neutral gas are de-coupled.

3.3 Initial conditions

Initial conditions define the starting point for any numerical simulation model. Solving the MHD equations and applying the boundary conditions the system will evolve. For the sake of reality, initial conditions as close as possible to the real state of the solar atmosphere should be applied.

The initial density profile mimics the height stratification observed in the solar atmosphere. The density in the photosphere is considered 100 times larger than that in the solar corona and decreases abruptly in the simulated transition region. The density profile used in the numerical simulation (Figure 3.1) is given by

$$\rho(z) = \frac{1}{2}\rho_f\Big(\frac{tanh(z + z_{fc} - 1) - tanh(z - z_{fc} + 1)}{tanh(z_{fc} - 1)}\Big) + \rho_c \tag{3.20}$$

where ρ_f is the photospheric density, ρ_c is the coronal density and z_{fc} is the location of the boundary between chromosphere and corona, the transition region, in the z axis ($z \approx 5L_0$). Here, $L_0 = 5 \times 10^5$ m is the unit length scale.

The gravity force is not considered in this model and the plasma is assumed to be in hydrostatic equilibrium ($p = const.$) at the beginning of the simulation. The temperature profile, shown in Figure 3.2, is then computed from the equation of state (3.19).

The initial magnetic field configuration is obtained from the photospheric line of sight (LOS) magnetic field using a force-free extrapolation ($\vec{\nabla} \times \vec{B} = \alpha\vec{B}$). The extrapolation method follows (Otto et al., 2007), and is similar to that developed in (Seehafer, 1978) but requires that the boundary conditions used in the extrapolation are consistent with the boundary conditions applied to the MHD model. More specifically, the initial magnetic

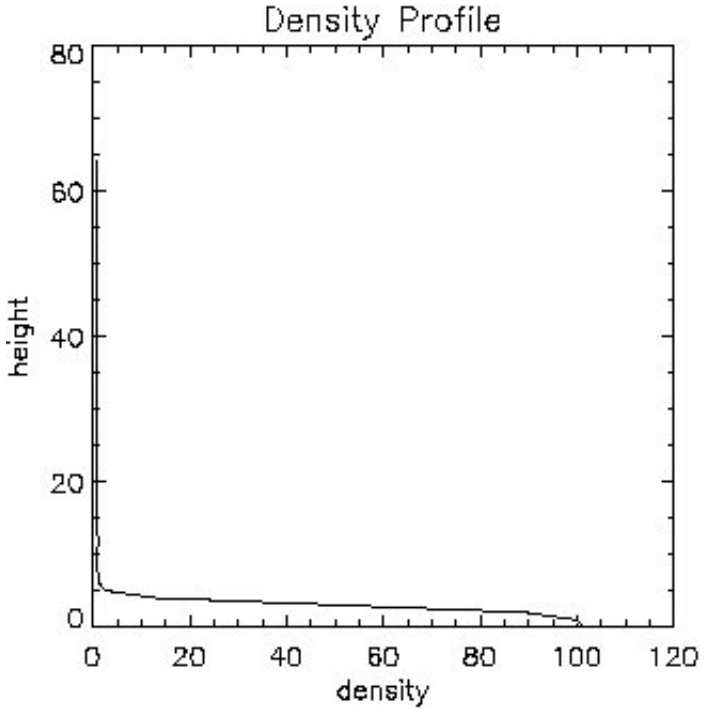

FIGURE 3.1 - Example of the density vertical profile used as initial condition in the MHD model.

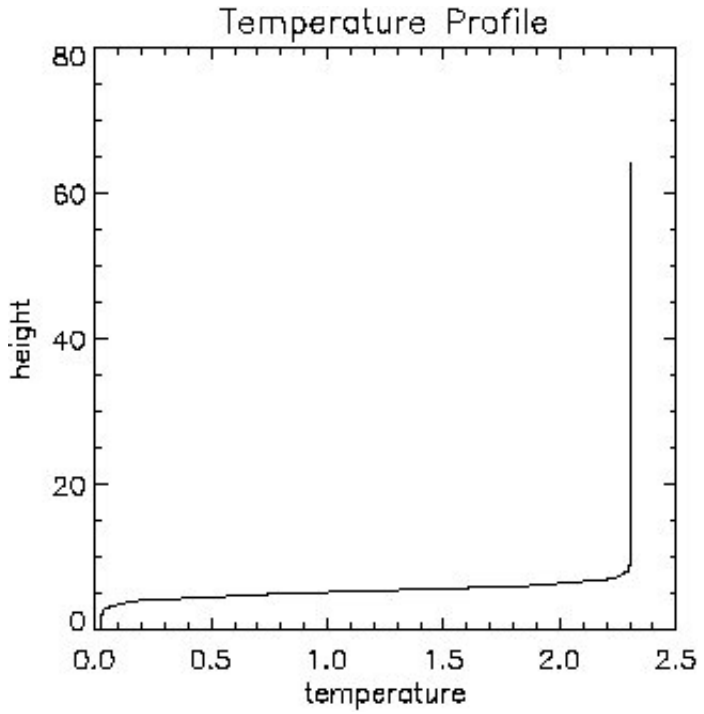

FIGURE 3.2 - Example of the temperature vertical profile used as initial condition in the MHD model.

field is assumed to be potential ($\vec{\nabla} \times \vec{B} = 0$), which means that there are no currents present in the system at all in the beginning.

Due to the discrete representation of the magnetic field and plasma, at the beginning of the simulation a relaxation phase is necessary to bring the system to an equilibrium situation, before to perturb it with the horizontal neutral gas velocity. During the relaxation phase the system is allowed to evolve 'freely' until it reaches the 'equilibrium', which can be determined by a force balance or the stability of the macroscopic variables.

After the relaxation phase has finished the neutral gas is allowed to move in the horizontal direction, to simulate the resulting evolution of the system. The velocity at the lower boundary is imposed by the neutral gas velocity. In the chromosphere the plasma is dragged behind since it interacts with the neutral gas by collisions (momentum equation). The collision frequency (Figure 3.3) assumes a maximum value of μ_0 in the photosphere and the profile is given by

$$\mu(z) = \mu_0 \Big(1 - \frac{z}{z_{fc}}\Big) \tag{3.21}$$

in the region covering photosphere and chromosphere ($z < 5$) and

$$\mu(z) = e^{\frac{-z}{4 z_{fc}}} \tag{3.22}$$

in the solar corona ($z > 5$).

The neutral gas motion can be conveniently generated by a combination of up to three velocity vortices. To avoid compression the resulting velocity field must satisfy $\vec{\nabla} \cdot \vec{u}_n = 0$. It can be introduced via a scalar potential U using the relation $\vec{u}_n = \vec{\nabla} \times (U \hat{e}_z)$, where

$$U = u_0 / cosh\Big(\frac{x - y + c_0}{L_0}\Big) / cosh\Big(\frac{x + y + c_1}{L_1}\Big). \tag{3.23}$$

The velocity is specified everywhere in the domain, but it is effective only where the collision frequency between neutral gas and plasma is larger than the inverse of the alfvén time (τ_A). In this way the velocity pattern calculated from the evolution of the photospheric magnetic field structures can be approximated.

The resistivity in the model contains a small background value η_0, which is chosen to be close to zero. In addition to this background resistivity, an anomalous resistivity is also applied. This anomalous resistivity is a function of the current density; when strong current densities appear it may be switched on allowing the occurrence of reconnection and the strong dissipation of currents to heat the solar atmosphere (Roussev et al., 2002).

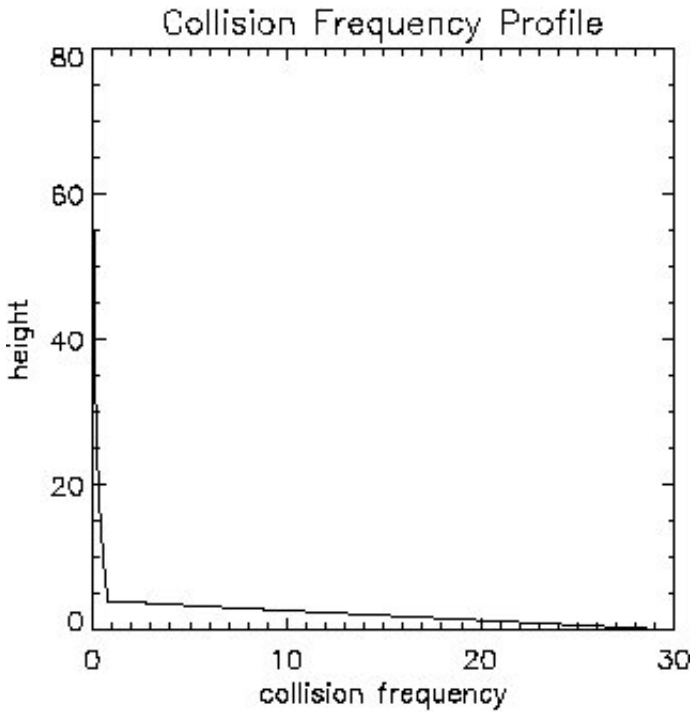

FIGURE 3.3 - Example of the collision frequency vertical profile used in the MHD model to couple the background neutral gas with the plasma.

3.4 Boundary conditions

The boundary conditions tell us how the variables behave at the system frontiers. They should be defined in a way that the MHD equations remain invariant under the transformation of the MHD variables. The simulation box has 6 boundaries: four lateral boundaries, the bottom boundary and the top boundary.

First, the boundary conditions in the x-y plane will be discussed. In this discussion the system boundaries are considered to be at $x = [0, L_x]$ and $y = \left[-\frac{L_y}{2}, +\frac{L_y}{2}\right]$. The symmetry conditions are considered at $x = 0$ for a plane $z = const$. The case where point (line) mirroring (at $x = 0$) with respect to $x = y = 0$ is used will be discussed. This boundary condition has the following characteristics: $x \rightarrow -x$, $y \rightarrow -y$, $z \rightarrow z$, $\partial_x \rightarrow -\partial_x$, $\partial_y \rightarrow -\partial_y$ and $\partial_z \rightarrow \partial_z$. This set of boundary conditions implies a line symmetry along the line $x = y = 0$.

The variables can be transformed in two different ways:

- Symmetric transformation

$$f(-x, y, z) = f(x, y, z) \tag{3.24}$$

TABLE 3.1 - Transformation properties resulting from the application of point (line) mirroring symmetry.

variable	set a	set b
ρ, p, η	(s)	(s)
u_x, u_y	(a)	(a)
u_z	(s)	(s)
B_x, B_y	(s)	(a)
B_z	(a)	(s)
j_x, j_y	(s)	(a)
j_z	(a)	(s)

- Antisymmetric transformation

$$f(-x, y, z) = -f(x, y, z) \tag{3.25}$$

for the boundary at $x = 0$. The symmetric transformation will be indicated by 's' and the antisymmetric transformation by 'a'. The positive definite MHD variables, such as density (ρ), pressure (p) and resistivity (η), must be symmetric. Examining the full set of MHD equations with these rules yields two possible sets of transformations which maintain the invariance of the equations (Table 3.1).

For the four lateral boundaries the MHD model here described uses the transformation properties presented in set b. Both sets could be used for the MHD equations, but this set presents the advantage of being applicable even when Hall MHD is considered. Figure 3.4 illustrates the geometry of the point (line) mirroring symmetry.

On the bottom boundary the magnetic field is obtained considering that there are no horizontal currents on the bottom boundary of the physical domain and also that $\vec{\nabla}\cdot\vec{B} = 0$ is valid, giving the relations:

$$\begin{aligned} \frac{\partial B_y}{\partial z} &= \frac{\partial B_z}{\partial x}, \\ \frac{\partial B_x}{\partial z} &= \frac{\partial B_z}{\partial x}, \\ \frac{\partial B_z}{\partial z} &= -\Big(\frac{\partial B_x}{\partial x} + \frac{\partial B_y}{\partial y}\Big). \end{aligned} \tag{3.26}$$

The plasma velocity is assumed to be equal to the neutral gas velocity. For the other variables, a reflective boundary condition is used and the variables are considered all symmetric. Also, it is considered that there is no flux of momentum through the bottom boundary ($u_z = 0$). The top boundary is an open boundary.

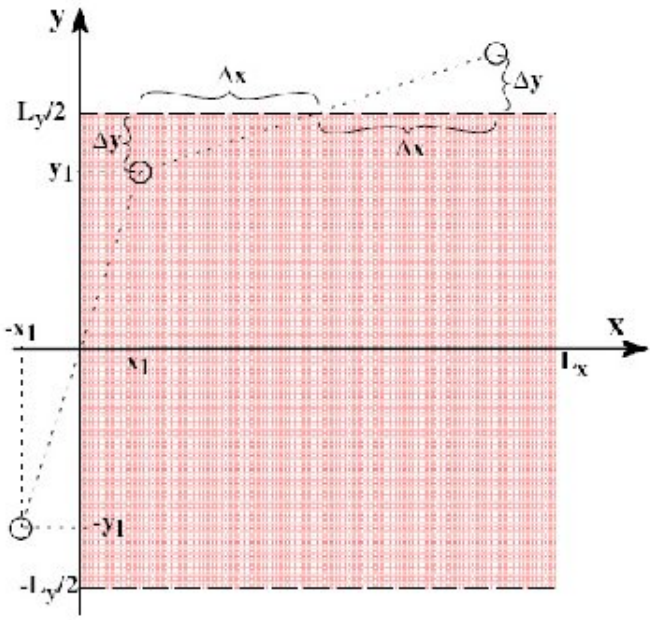

FIGURE 3.4 - Illustration of the geometry of the point (line) mirroring symmetry. (Otto et al., 2007)

3.5 Normalization and plasma parameters

In the set of equations discussed so far, all parameters and variables bear their original values and are not normalized. Very large quantitative differences can appear among these values and when these numbers are used directly in numerical calculations large errors would occur. A way to overcome this difficulty is to normalize the equations. Normalization is the transformation of the parameters and variables of the simulation to proper units, which makes these parameters and variables as close as possible to the unity.

In the MHD model used to study the solar atmosphere the following normalization parameters are used: the magnetic field is normalized to $B_0 = 1G = 10^{-4}$ T; the plasma density is normalized to the density in the corona just above the transition region ($n_0 = 2 \times 10^{15}$ m^{-3}); the mass density is given by $\rho_0 = m_p n_0$, where m_p is the proton mass; the length scale is normalized to $L_0 = 500$ km; the velocities are normalized to the Alfvén speed calculated for the normalizing magnetic field and plasma density ($v_0 = v_{A_0} = \frac{B_0}{\sqrt{u_0 \rho_0}} = 50$ km/s); the time is normalized to the Alfvén transit time through the normalizing length ($\tau_0 = \tau_A = \frac{L_0}{v_A} = 10$ s); the pressure is normalized to the magnetic pressure ($p_0 = \frac{B_0^2}{2\mu_0} = 4 \times 10^{-3}$ Pa); the temperature is obtained using the relation $p = 2n\kappa_B T$, considering $T_e = T_i$, and normalized to $T_0 = \frac{p_0}{2n_0\kappa_B} = 7.2 \times 10^4$ K; the electric field is normalized to $E_0 = v_{A_0} B_0$; the current density is normalized to $j_0 = \frac{B_0}{\mu_0 L_0}$; the resistivity is normalized to $\eta_0 = \mu_0 L_0 v_{A_0}$; and the collision frequency is normalized to the

TABLE 3.2 - Quantities defined in terms of typical values for a system.

quantity	normalized quantity
$\vec{\nabla}$	$\frac{1}{L_0}\vec{\nabla}'$
$\vec{B}$	$B_0\vec{B}'$
n	$n_0 n'$
$\vec{v}$	$v_0\vec{v}' = \frac{B_0}{\sqrt{\mu_0\rho_0}}\vec{v}' = \frac{L_0}{\tau_0}\vec{v}'$
t	$\tau_0 t'$
p	$p_0 p' = \frac{B_0^2}{2\mu_0}p'$
T	$T_0 T' = \frac{p_0}{2n_0\kappa_B}T'$
$\vec{E}$	$E_0\vec{E}' = v_0 B_0\vec{E}'$
$\vec{j}$	$j_0\vec{j}' = \frac{B_0}{\mu_0 L_0}\vec{j}'$
η	$\eta_0\eta' = \mu_0 L_0 v_0\eta'$

inverse of the Alvén time $\left(\frac{1}{\tau_A}\right)$.

3.6 Normalized MHD equations

The physical quantities can be defined in therm of typical values for a system (Table 3.2). The substitution into the MHD equations specifies the normalization values to yield a new set of equations for the normalized quantities (Appendix A). The normalized MHD equations become

$$\frac{\partial\rho}{\partial t} = -\vec{\nabla}\cdot\rho\vec{u} \tag{3.27}$$

$$\begin{aligned}\frac{\partial\rho\vec{u}}{\partial t} &= -\vec{\nabla}\cdot\rho\vec{u}\vec{u} - \frac{1}{2}\vec{\nabla}p + \vec{j}\times\vec{B} - \eta\rho(\vec{u}-\vec{u}_0)\\ &= -\vec{\nabla}\cdot\left[\rho\vec{u}\vec{u} + \frac{1}{2}(p+B^2)\underline{1} - \vec{B}\vec{B}\right] - \eta\rho(\vec{u}-\vec{u}_0)\end{aligned} \tag{3.28}$$

$$\frac{\partial\vec{B}}{\partial t} = \vec{\nabla}\times(\vec{u}\times\vec{B} - \eta\vec{j}) \tag{3.29}$$

$$\frac{\partial p}{\partial t} = -\vec{\nabla}\cdot p\vec{u} - (\gamma-1)p\vec{\nabla}\cdot\vec{u} + 2(\gamma-1)\eta j^2 \tag{3.30}$$

together with the Ohm's and Ampère's laws

$$\vec{E} = -\vec{u}\times\vec{B} + \eta\vec{j} \tag{3.31}$$

$$\vec{\nabla}\times\vec{B} = \mu_0\vec{j}, \tag{3.32}$$

where the *prime* symbol was omitted for simplicity.

In the pressure (energy) equation, the pressure p is substituted by the variable $h = \left(\frac{p}{2}\right)^{\frac{1}{\gamma}}$ because this yields a continuity equation in the absence of any source terms for the internal energy. The derivation of the energy equation for h is as follows:

$$\begin{aligned}
\frac{\partial p}{\partial t} &= -\vec{\nabla}\cdot p\vec{u} - (\gamma-1)p\vec{\nabla}\cdot\vec{u} + 2(\gamma-1)\eta j^2 \Rightarrow \\
2\frac{\partial h^\gamma}{\partial t} &= -2\vec{\nabla}\cdot h^\gamma\vec{u} - 2(\gamma-1)h^\gamma\vec{\nabla}\cdot\vec{u} + 2(\gamma-1)\eta j^2 \Rightarrow \\
2\gamma h^{\gamma-1}\frac{h}{t} &= -2h^\gamma\vec{\nabla}\cdot\vec{u} - 2\vec{u}\cdot\vec{\nabla}h^\gamma - 2(\gamma-1)h^\gamma\vec{\nabla}\cdot\vec{u} \\
&+ 2(\gamma-1)\eta j^2 \Rightarrow \\
2\gamma h^{\gamma-1}\frac{h}{t} &= -2\gamma h^{\gamma-1}\vec{u}\cdot\vec{\nabla}h - 2\gamma h^\gamma\vec{\nabla}\cdot\vec{u} \\
&+ 2(\gamma-1)\eta j^2 \Rightarrow \\
\frac{\partial h}{\partial t} &= -\vec{u}\cdot\vec{\nabla}h - h\vec{\nabla}\cdot\vec{u} + \frac{\gamma-1}{\gamma}h^{1-\gamma}\eta j^2. \qquad (3.33)
\end{aligned}$$

3.7 Numerical properties of the simulation

The system of equations presented in the previous section is solved in a 3D cartesian grid using finite difference discretization techniques. The grid is chosen equidistant in the x and y direction. It is non-equidistant in the z (vertical) direction. The resolution in the vertical direction decreases with height. It is chosen like this to treat the steep gradients in temperature and density that are characteristic for the transition region. Figure 3.5 shows how the step size varies with height. The maximum resolution is achieved close to the base of the system ($z = 0$), it is equal to 150 km.

Equations (3.27), (3.28), (3.29) and (3.30) are advanced in time using Leapfrog scheme (POTTER, 1973). This scheme is second order accurate and has very low numerical dissipation. The Leapfrog scheme is a two step scheme and for the first step Lax scheme (POTTER, 1973) is used. A small dissipation is switched on if oscillations develop on the grid scale, similar to FCT schemes (Devore, 1991). Figure 3.6 shows a flowchart with the main steps used in the simulation to solve numerically the MHD equations.

A correction is applied to the magnetic field before the numerical simulation starts. Due to numerical errors the solenoidal condition ($\vec{\nabla}\cdot\vec{B} = 0$)) is not fulfilled at the beginning of the simulation. To bring the values of the $\vec{\nabla}\cdot\vec{B}$ close to zero, avoiding the occurrence of non-physical forces, a divergence cleaning procedure (Appendix E) was developed. This procedure is applied to the magnetic field after the extrapolated magnetic field is generated

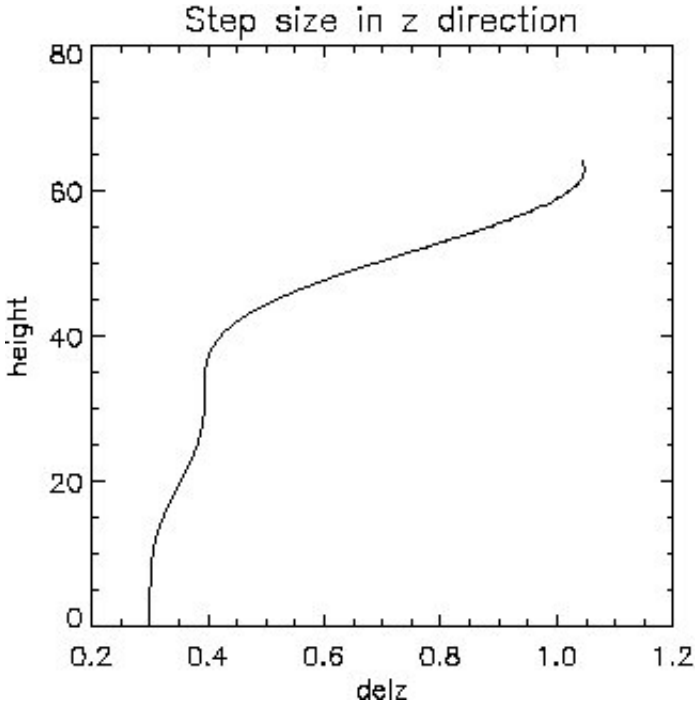

FIGURE 3.5 - Example of how the step size in the vertical direction (z direction) used in the nonuniform grid can vary. In this example the maximum resolution is $0.3L_0$ on the base of the simulation box.

and interpolated in the non-equidistant grid.

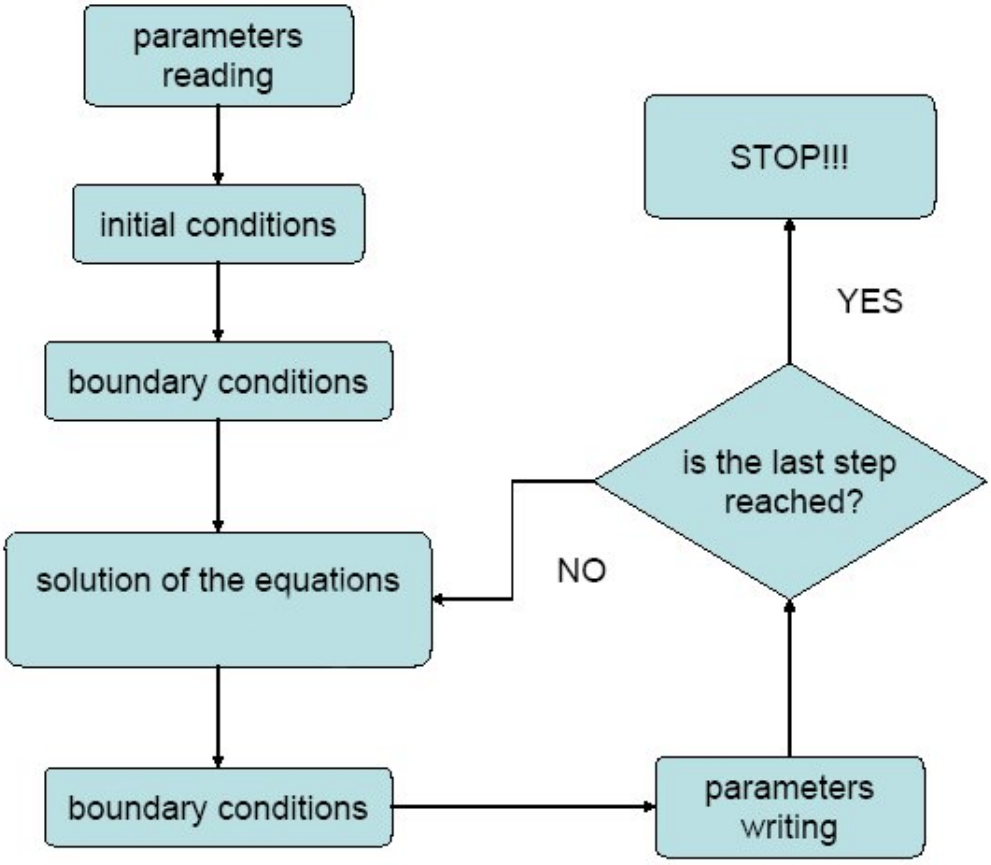

FIGURE 3.6 - Flowchart showing the main steps in the MHD simulation.

4 ON THE RELATION BETWEEN DC CURRENT LOCATIONS AND AN EXTREME ULTRAVIOLET BRIGHT POINT

Extreme-UltraViolet (EUV) and X-ray Bright Points (BPs) (Golub, 1980; Webb, 1986; Habbal, 1992) are a directly observable phenomena of the solar corona heating. Their understanding might provide a key to answer a question that for more than six decades has puzzled researchers: what is heating the solar corona? At the moment the attempts to answer this question can be divided in two main groups of heating models: wave (AC) heating and electric current (DC) heating. The energy source of both mecanisms is the photospheric kinetic energy reservoir. AC heating (Alfvén, 1947) requires that the magnetic field is moved around in the solar photosphere faster than the Alfvén crossing time of typical structures. Waves are generated in this process which must then be dissipated in the solar corona to generate heat. DC heating requires a slower plasma motion in the photosphere, at timescales longer than the Alfvén crossing time. Such motion generates currents that cannot be easily dissipated through conventional joule heating (Parker, 1972), but requires the occurrence of anomalous resistivity (Birn; Priest, 2007; Büchner; Elkina, 2005; Büchner; Elkina, 2006).

The main properties of BPs are summarized e.q. in (Brown et al., 2001), (Sattarov et al., 2002), (Madjarska et al., 2003) and (Ugarte-Urra et al., 2004) (and references therein): BPs are small-scale features of enhanced X-ray and EUV emission with an average size of 30-40 arcsec^2. Their fine structure seen in high-resolution (below 2 arcsec) images represents small-scale loops evolving at a time scale of $\approx$ 6 min. The average life time of BPs is 20 hours in EUV and 8 hours in X-ray observations. BPs are observed at different temperatures and their density distributions resembles that of an active region (Ugarte-Urra et al., 2004). An important characteristics that can help to understand their nature is the fact that BPs are associated with moving bipolar magnetic features. During the evolution of one BP, (Brown et al., 2001) found different patterns of motion of the magnetic structures in the solar photosphere. The patterns of motion, coalescence, fragmentation, rotation and translation, were associated with different stages of the evolution of the BP: pre-brightening stage, the initial brightening, the sigmoid phase and the π-phase, respectively.

Most of the models developed to explain the observational features associated with BPs consider the interaction between the magnetic field of the moving bipolar magnetic feature and the surrounding magnetic field (Priest et al., 1994; Parnell et al., 1994b; Longcope, 1998; von Rekowski et al., 2006). However, these models usually do not consider the role of the plasma moving through regions of strongly diverging magnetic flux. (Büchner et al., 2004a; Büchner et al., 2004b) and (Büchner, 2006) show that horizontal plasma motion in the photosphere causes the formation of localized current sheets in and above the transition region at

the position of an EUV BP. These authors suggest that the enhanced current flow can make the current sheet resistive and allows stress relaxation by current dissipation and reconnection which power the BP.

In the following the results obtained using a 'data driven' three dimensional (3D) magnetohydrodynamic (MHD) model (Büchner et al., 2004a), described in chapter 3, to study the evolution of plasma and magnetic field in an EUV BP region observed on 2006 January 19 are presented. The velocity fields responsible for the evolution of the photospheric magnetic features between 16:00 UT and 17:30 UT are derived in accordance with the methods described in chapter 2, and are applied as a boundary conditions to the model. Chapter 4 is organized as follows: the observations are described in Section 4.1; the results obtained for the parallel and perpendicular currents using different velocity fields are presented in Section 4.2; and a discussion of the results and the main conclusions are given in Section 4.3.

4.1 Observational data

The model is applied to an EUV BP observed on 2006 January 19 by the Extreme-ultraviolet Imaging Telescope (EIT) in the Fe XII 195 Å passband, the Transition Region And Coronal Explorer (TRACE) in the 1550 Å passband (dominated by the C IV 1548 Å line and continuum emission) and the Michelson Doppler Imager (MDI). The BP appears in the EIT 195 Å images as a feature of diffused enhanced emission with a bright kernel which evolves in time (Figure 4.1, top). Due to the relatively low spatial resolution of the EIT images (2.62 arcsec/pixel), the fine structure of the BP cannot be resolved. Even though, the general evolution of the feature which has a size of 30 arcsec × 20 arcsec can be tracked. The TRACE 1550 Å images (0.5 arcsec/pixel) clearly show the BP as composed of numerous small-scale bright points (diameter comparable with the instrument resolution) believed to represent a cross-section of the BP loops (Fig. 4.1, middle). MDI provided LOS magnetograms at half resolution (2 × 2 pixels binned images resulting in 1.99 arcsec/pixel, bottom). The BP is associated with a magnetic bipolar region with the bright kernel overlying the negative polarity (Fig. 4.1, bottom). The alignment of the imager (EIT) and magnetogram data was achieved through the header pointing information.

To obtain the velocity responsible for the evolution of the photospheric magnetic structures associated with the EUV BP the local correlation tracking (LCT) technique (November; Simon, 1988) is used. First, the LOS component of the photospheric magnetic field is filtered using a Fourier filter to select the first eight modes of interest. Then, LCT is applied to the filtered magnetograms separated by a time interval of approximately 30 minutes, covering the interval between 16:00 UT and 17:30 UT. As a result, three different velocity patterns

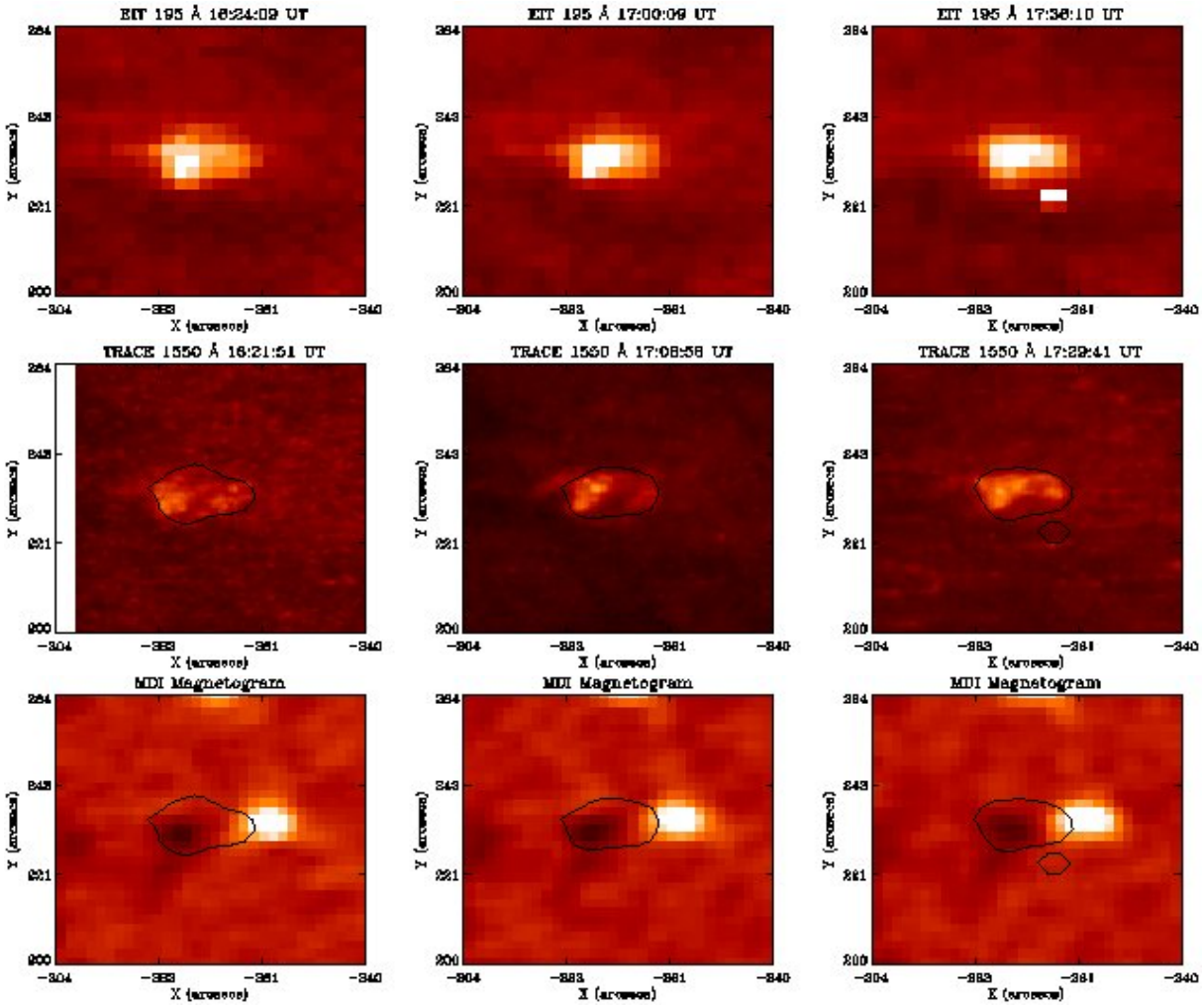

FIGURE 4.1 - Evolution of the EUV BP as seen by EIT/SOHO (top panels) and TRACE (middle panels), together with the LOS component of the photospheric magnetic field measured by MDI/SOHO (bottom panels). The images were obtained at three different instants of time: at around 16:30 UT (left column), 17:00 UT (central column) and 17:30 UT (right column). The X and Y axis are in arcsec (1arcsec= 726 km) and the contour line shows the position of the EUV BP as seen by EIT in 195 Å passband.

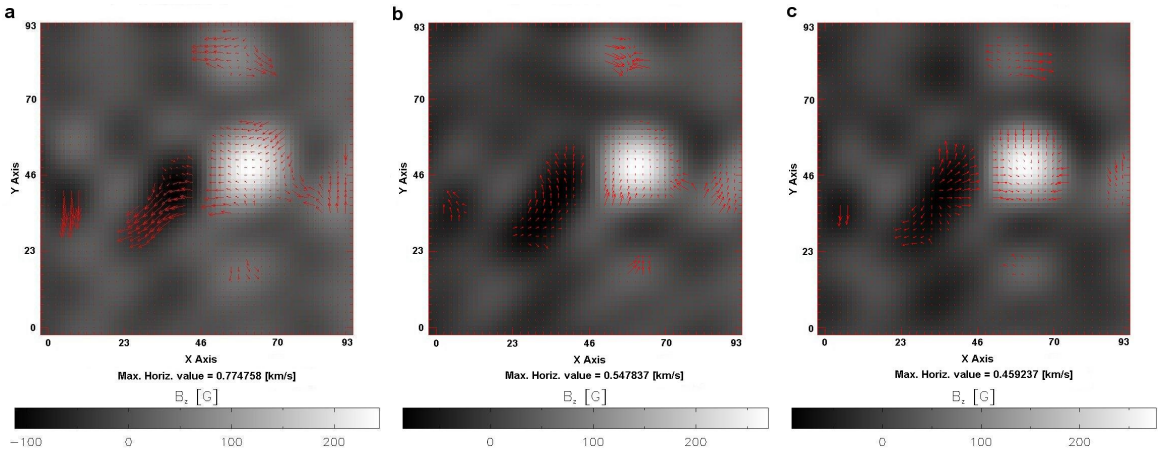

FIGURE 4.2 - Horizontal velocity obtained using LCT technique applied to the filtered photospheric magnetic field in the interval a)16:00 UT - 16:30 UT, b) 16:30 UT - 17:00 UT and c) 17:00 UT - 17:30 UT. The arrows show the horizontal velocity, while the gray scale shows the filtered LOS component of the photospheric magnetic field. The X and Y axis are in terms of the characteristic length scale ($L_0 = 5 \times 10^5$ m) and they cover the same area displayed in the MDI image of Fig.4.1.

are obtained, as shown in Figure 4.2. The horizontal motion around the positive magnetic field concentration is, however, an effect of the emergence of magnetic flux in that region interpreted by LCT as a horizontal velocity pattern (Démoulin; Berger, 2003). For this reason, in the simulation we focus on the horizontal motion derived from the displacement around the negative magnetic field concentration. The obtained velocity patterns can be described as follows: the first velocity pattern (Figure 4.2a) moves the negative polarity southward, away from the positive polarity; the second velocity pattern (Figure 4.2b) moves the negative polarity towards the positive polarity; and the third velocity pattern (Figure 4.2c) break the negative polarity apart, moving part of it towards the positive polarity and part of it away from the positive polarity. In the simulation model these motions are approximated by using a combination of vortices of velocity (Figure 4.3). The first velocity pattern (Fig. 4.2a) is approximated by a vortex that moves the negative polarity away from the positive polarity. The second velocity pattern (Fig. 4.2b) is approximated using a vortex that moves the negative polarity toward the positive polarity. Finally, the third velocity pattern (Fig. 4.2c) is approximated by combining two small vortices that break the negative polarity apart, moving part of it away from the positive polarity and the other part toward the positive polarity. The combination of the vortices in the third velocity pattern enhances the flow in the region between the vortices and makes the full vortical structure visually disappear. The Vx/Vy over the panels on Fig. 4.3 means that the velocity vectors in x–y plane are shown.

Figure 4.4 show the characteristics of the simulation box used to study the evolution of plasma and magnetic field over the BP region. It has $46.4 \times 46.4 \times 15.45$ Mm^3 and is

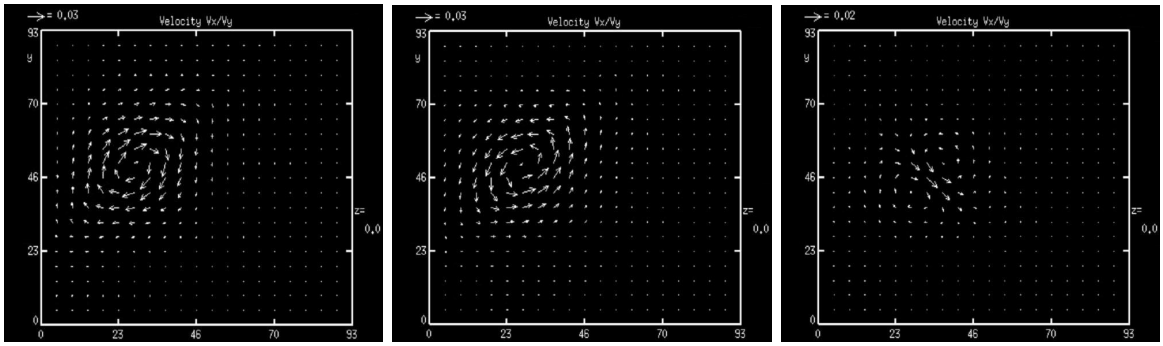

FIGURE 4.3 - Horizontal velocity used as boundary condition of the model to approximate the velocity pattern obtained for the interval 16:00 UT - 16:30 UT (left panel), 16:30 UT - 17:00 UT (central panel) and 17:00 UT - 17:30 UT (right panel). The arrows show the horizontal velocity. The maximum value of the horizontal velocity is given on the top left of each panel in terms of the Alfvén velocity ($v_A = 5 \times 10^4$ m/s). The X and Y axis are in terms of the characteristic length scale ($L_0 = 5 \times 10^5$ m) and they cover the same area displayed in the MDI image of Fig.4.1.

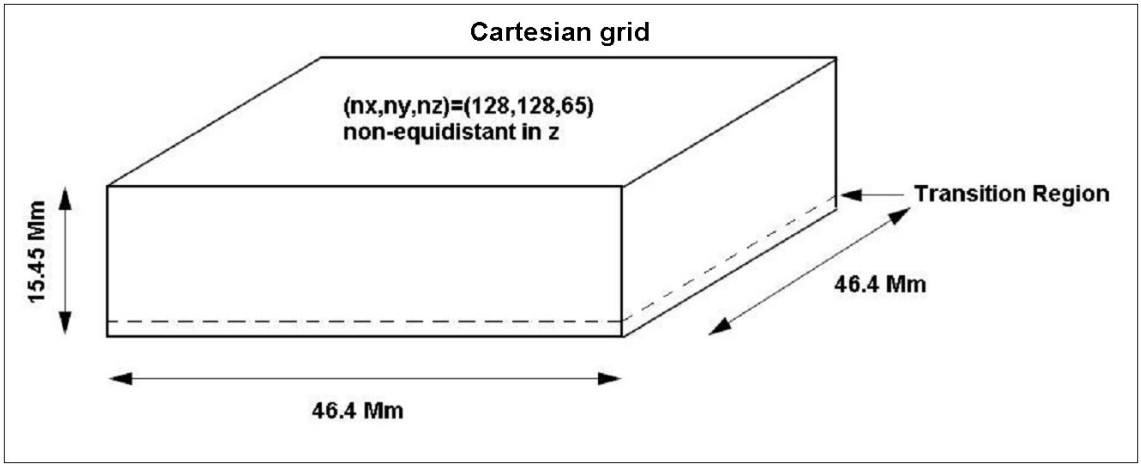

FIGURE 4.4 - Illustration showing the size of the simulation box used to study the evolution of plasma and magnetic field over the region associated to the BP of 2006 January 19.

discretized using a non-equidistant cartesian grid in the z direction with dimensions of $(128, 128, 65)$ grid points. The grid has maximum resolution on the bottom of the simulation box and the resolution decreases with height. The initial density and temperature profile try to mimic the observed density and temperature in the Sun's atmosphere (Chapter three, initial conditions). The initial three-dimensional magnetic field inside this box is obtained from a potential extrapolation of the filtered LOS photospheric magnetogram measured at 16:00 UT, as shown in Figure 4.5.

4.2 Results and discussion

We perform three simulation runs using the velocity patterns showed in Fig. **??**. The simulation starts always from the same initial condition. The difference from one simula-

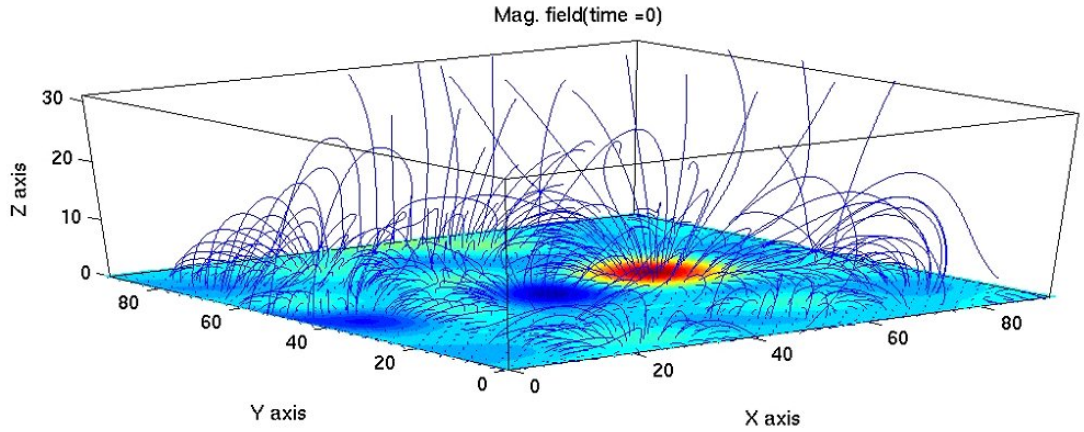

FIGURE 4.5 - Initial magnetic field obtained from a potential extrapolation of the filtered LOS magnetic field measured at 16:00 UT on 2007 January 19. The lines show the magnetic field lines of force and the colour code show the photospheric LOS magnetic field. The axis are given in terms of L_0.

tion run to the other is the neutral gas velocity used to perturb the system. This allows to compare the results and assume that any change in the evolution of the system is a consequence of the different velocity pattern assumed for the neutral gas.

Strong electric currents are expected to develop in regions where the magnetic field strongly changes the connectivity, known as quasi-separatrix layers (Démoulin et al., 1996a; Démoulin et al., 1996b). It is expected also that the effects of plasma motion in the generation of electric currents will be much more effective on these regions (Aulanier et al., 2005; Büchner, 2006). Due the fact that the coupling between neutral gas and plasma is much more efficient bellow the transition region, and the magnetic field is more intense there, it is expected that strong electric currents will develop in low heights in the solar atmosphere.

Indeed, the different horizontal patterns of photospheric plasma motion, used as boundary condition for the model, give rise to electric currents located mainly below the transition region, over the main polarities of the magnetic field. The current densities are diagnosed in two components, parallel ($j_\parallel$) and perpendicular ($j_\perp$) to the magnetic field , and analyzed independently. Figure 4.6 shows the isosurfaces of a parallel current density $j_\parallel = 2j_0$, where $j_0 = \frac{B_0}{\mu_0 L_0} \approx 1.59 \times 10^{-4}$ A/m^2 is the value used to normalize the electric current density. This current system results from the application of the first velocity pattern (left panel of Figure 4.3) which moves the negative polarity region southward, away from the positive polarity. This motion pattern stretches the magnetic flux tubes, increasing their magnetic energy contents. The horizontal motion also give rise to electric currents perpendicular to the magnetic field. Figure 4.7 shows the isosurfaces of a perpendicular current

density $j_\perp = 2j_0$. The parallel and perpendicular currents are formed in the chromosphere, transition region and lower corona. The perpendicular current is less distributed than the parallel component, appearing as kernels of current concentration. The vertical profile of the squared current density integrated over the area A, where A is the total area of the x–y plane of the simulation box,

$$E_j(z) = \int_A j^2 dxdy \tag{4.1}$$

is calculated at $t = 1300s$, for the parallel and the perpendicular current densities, and is used as a proxy for the current energy (Figure 4.8). The current energy presents a minimum value in a region between $z = 15L_0$ and $z = 25L_0$, where $L_0 = 5 \times 10^5$ m is the value used as the characteristic length scale. The highest values for the electric current energy are found for $z < 15L_0$. The model transition region corresponds to $z \approx 5L_0$. The energy associated with the parallel current dominates over that associated with the perpendicular current. The increase of the energy near the top of the simulation box is a boundary effect.

The other two velocity patterns obtained by LCT for later times of the evolution of the EUV BP are also used as boundary condition in the simulation. During the second period (central panel of Figure 4.3) the negative polarity moves northward, in the direction toward the positive polarity region. This lead to a decrease of the total magnetic flux (flux cancelation). The electric currents resulting from this motion are shown in Figure 4.9 and Figure 4.10. The parallel and perpendicular currents are formed preferentially below $z = 10L_0$. However, parallel currents start to develop higher in the solar atmosphere ($z \approx 20L_0$) due to the interaction of the magnetic fields resulting from the converging motion of the two opposite magnetic field polarities that form the bipole. The profile of the current energy (Figure 4.11) shows that in this case the highest values for the current energy are found for $z < 10L_0$, lower than in the first case. However, the current energy above $z \approx 15L_0$ is higher than in the first period. The energy associated with the parallel current dominates over that associated with the perpendicular current.

During the third period (right panel of Figure 4.3) the negative flux concentration break apart, part of it moving southward and the other part northward in the direction toward the positive polarity. The isosurfaces of current density obtained from this velocity pattern as boundary condition are shown in Figure 4.12 and Figure 4.13. Figure 4.14 shows the current energy profile for this period. Regions of minimum and higher values for the current energy are similar to the first period (notice the scale of the y axis). As in the previous cases, the isosurfaces of enhanced currents appear preferentially below $z = 10L_0$ and the parallel current is more distributed than the perpendicular current. In all cases the

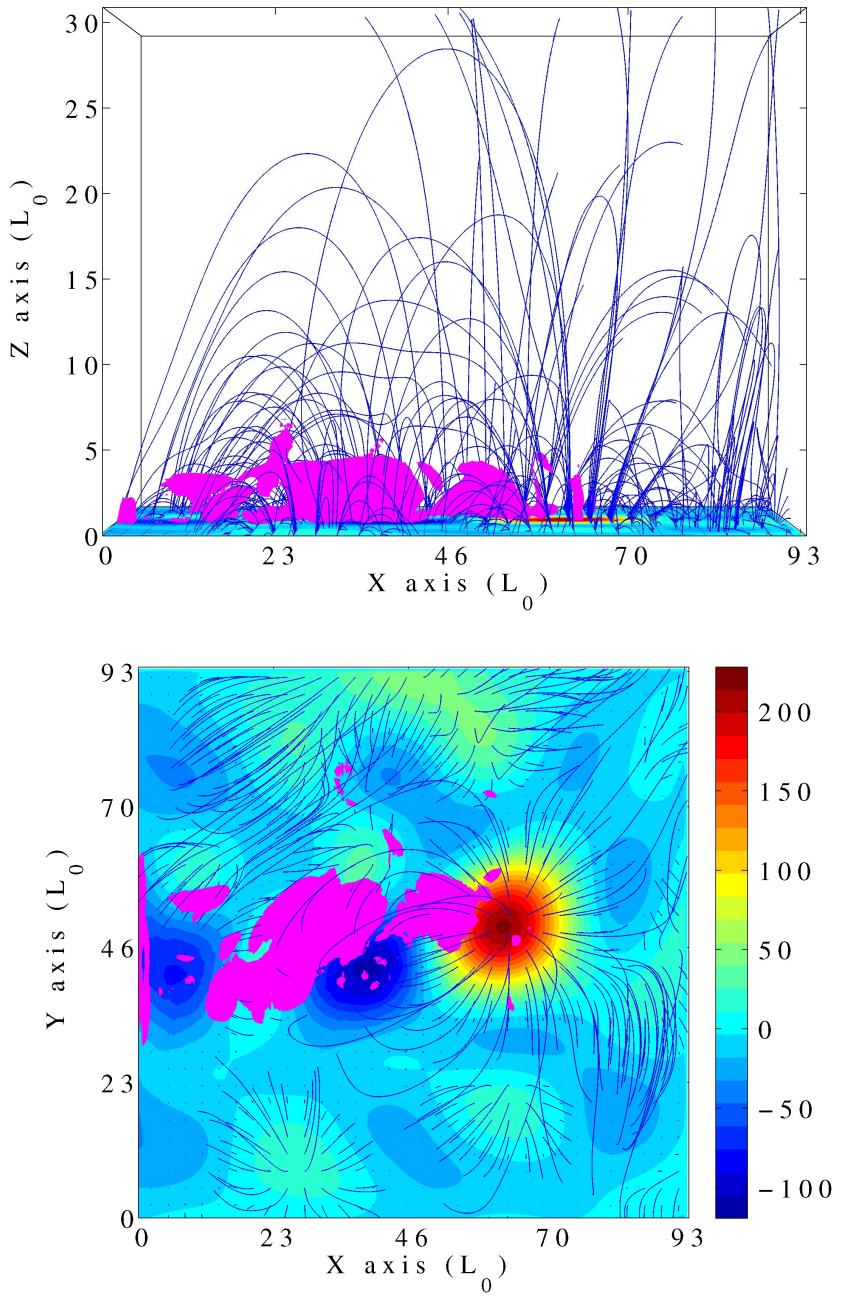

FIGURE 4.6 - Lateral view (top panel) and top view (bottom panel) of the isosurfaces of a parallel current density $j_{\parallel} = 2j_0$ at the instant $t = 1300$ s, resulting from the application of the first velocity pattern as boundary condition of the model (left panel of Fig.4.3). The colour code shows the vertical component of the photospheric magnetic field, with magnetic field values given in G, and the lines correspond to the magnetic field lines of force. The isosurfaces of parallel current density are shown in magenta.

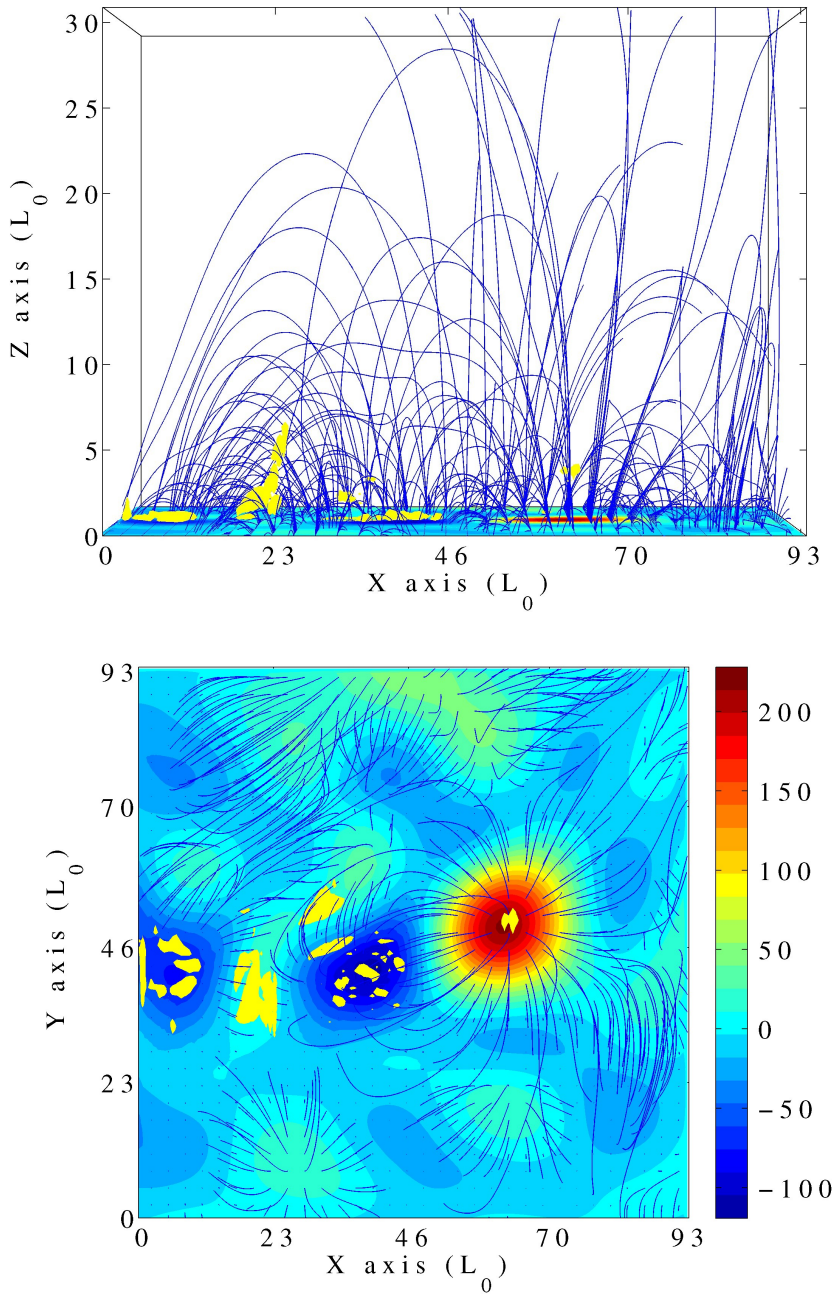

FIGURE 4.7 - Lateral view (top panel) and top view (bottom panel) of the isosurfaces of a perpendicular current density $j_\perp = 2j_0$, at the instant $t = 1300$ s, resulting from the application of the first velocity pattern as boundary condition of the model (left panel of Fig.4.3). The colour code shows the vertical component of the photospheric magnetic field, with magnetic field values given in G, and the lines correspond to the magnetic field lines of force. The isosurfaces of perpendicular current density are shown in yellow.

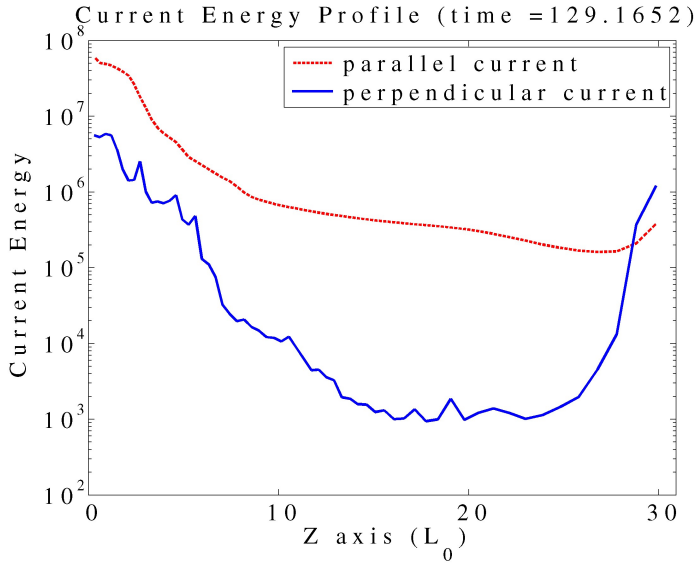

FIGURE 4.8 - Height profile of the current energy obtained using the first velocity pattern at $t = 1300$ s.

electric currents are formed in the region where the motion is applied and over the main concentrations of magnetic field, independent of the motion pattern used as boundary condition to the model. This occurs because there are some preferential places for the development of currents and these places are determined by the topology of the magnetic field and by the place where the motion is applied, rather than by the specific form of the horizontal velocity pattern.

The evolution in time of the total magnetic energy inside the simulation box is calculated as

$$E_B = \int_V \frac{B^2}{2\mu_0} dV. \tag{4.2}$$

Figure 4.15 shows the total magnetic energy (joules) versus time. The different runs correspond to the application of the different velocity patterns as boundary condition. The results obtained in run 1, for the evolution starting at 16:00 UT, show that the total magnetic energy increases while the opposite magnetic polarities are moved apart. The results in the second run, for the evolution after 16:30 UT, represent the effect of flux cancelation: a decrease of the total magnetic energy of the system. Run 3, describing the evolution after 17:00 UT, is intermediate between run 1 and run 2, where the break of the negative polarity and the motion of part of it away from the positive polarity and part of it in direction to the positive polarity maintain the total magnetic energy almost constant. Changes in the configuration of the magnetic field would change the location of the quasi-separatrix layers, and consequently the location where the electric currents develop. Also, changes in the location where the patterns of motion are applied would

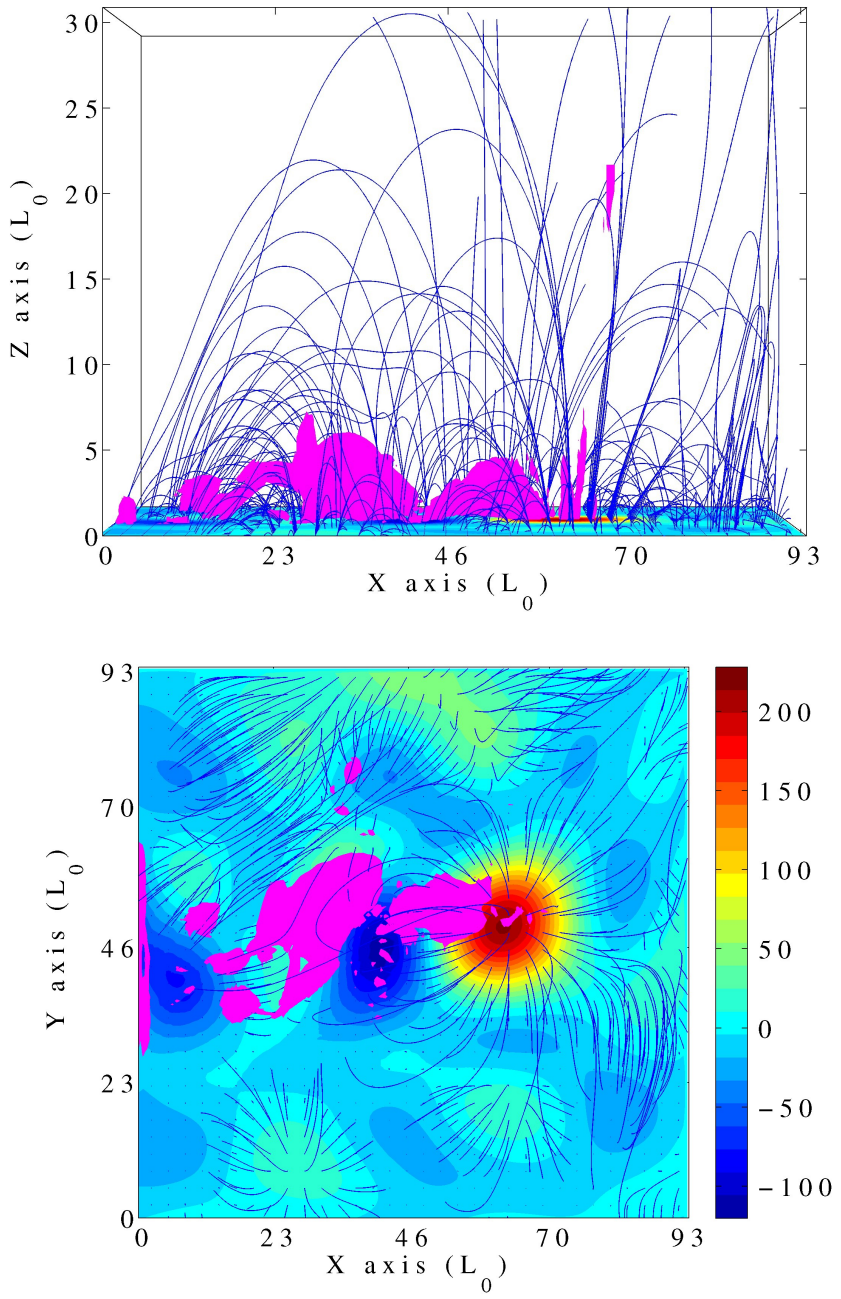

FIGURE 4.9 - Lateral view (top panel) and top view (bottom panel) of the isosurfaces of a parallel current density $j_{\parallel} = 2j_0$, at the instant $t = 1300$ s, resulting from the application of the second velocity pattern as boundary condition of the model (central panel of Fig.4.3). The colour code shows the vertical component of the photospheric magnetic field, with the magnetic field values given in G, and the lines correspond to the magnetic field lines of force. The isosurfaces of parallel current density are shown in magenta.

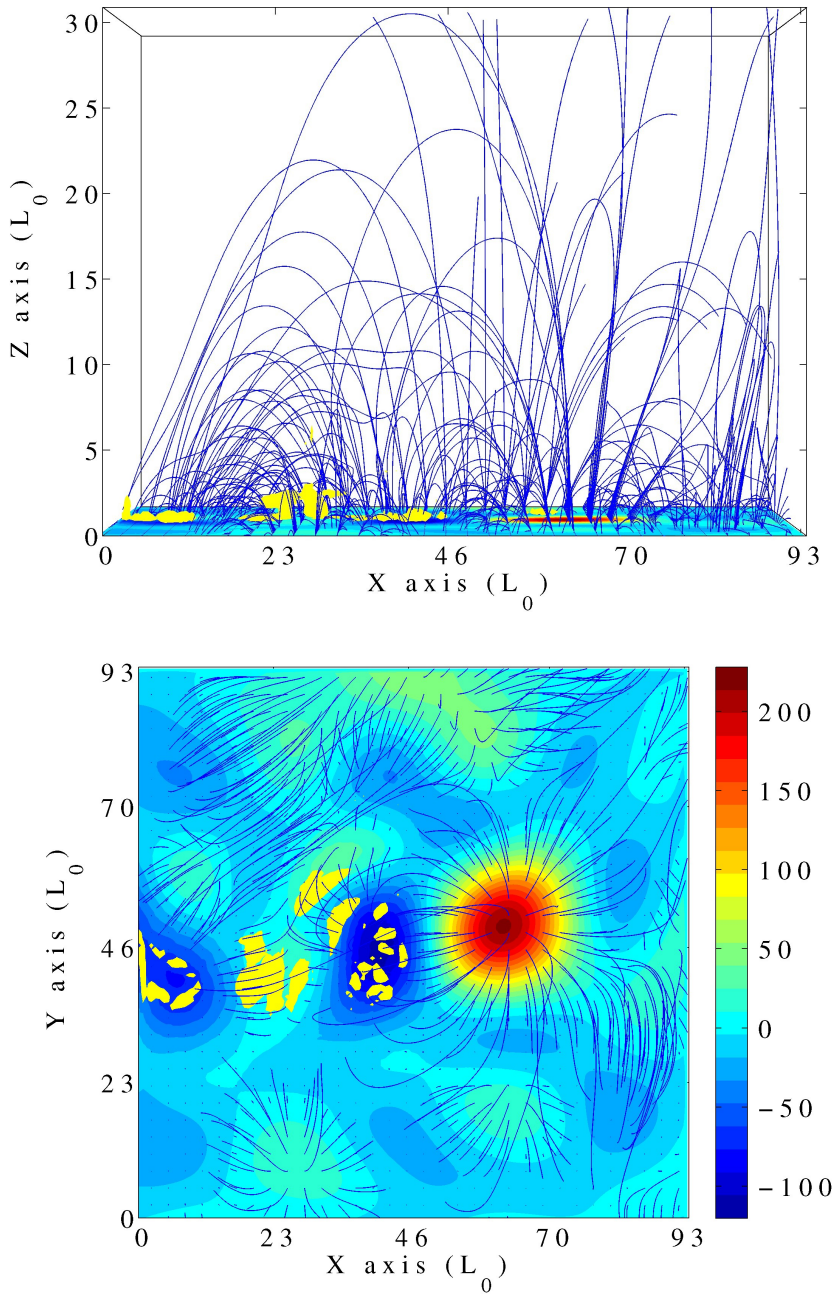

FIGURE 4.10 - Lateral view (top panel) and top view (bottom panel) of the isosurfaces of a perpendicular current density $j_\perp = 2j_0$, at the instant $t = 1300$ s, resulting from the application of the second velocity pattern as boundary condition of the model (central panel of Fig.4.3). The colour code shows the vertical component of the photospheric magnetic field, with the magnetic field values given in G, and the lines correspond to the magnetic field lines of force. The isosurfaces of perpendicular current density are shown in yellow.

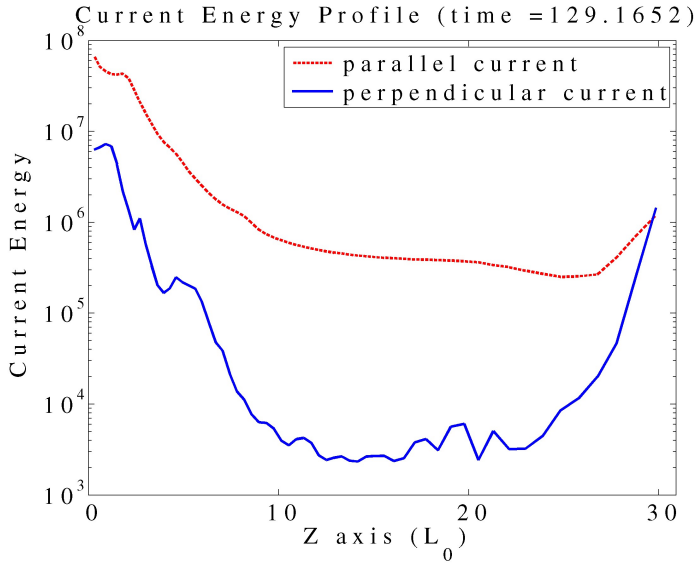

FIGURE 4.11 - Height profile of the current energy obtained using the second velocity pattern at $t = 1300$ s.

change the location of the current systems. However, stronger currents are expected to develop always in the lower part of the simulation box, where the magnetic field is more intense and the coupling between the neutral gas and plasma is more effective.

The plasma resistivity has an important contribution to the changes in the field topology, second term in the rhs of equation (3.15), and to the energy balance, by heating of the plasma by means of joule effect. As discussed in section 3, the model here described considers two different kinds of resistivity: a background resistivity, that is close to zero, and an anomalous resistivity, that is proportional to the velocity of the current carrier. The background resistivity has a global effect, but since it is choosen to be close to zero this effect is very small. The effect of the anomalous resistivity is localized and stronger than that of the background resistivity, depending on the velocity of the current carrier.

Electrical currents can lead to streaming instabilities, exciting a variety of modes of plasma oscillation which collectively lead to turbulence. The energy carried by the electrical current is then efficiently converted to turbulent motions which, through Coulomb collisions, rapidly heat the electrons. These instabilities begin when the current carrier speed $\left(v_{cc} = \frac{j}{en_e}\right)$ exceeds certain critical values. For the case when $T_e \cong T_i$, an important instability will appear when $v_{cc} \sim \xi$, where $\xi = \sqrt{\kappa_b T_e / m_e}$ is the thermal speed of electrons. In this case it is expected that the effective collision time will be reduced from the kinetic value to the much smaller value $\frac{2\pi}{\omega_{pe}}$, where ω_{pe} is the electron plasma frequency, enhancing the resistivity accordingly. Based on this physical picture a parametrization for

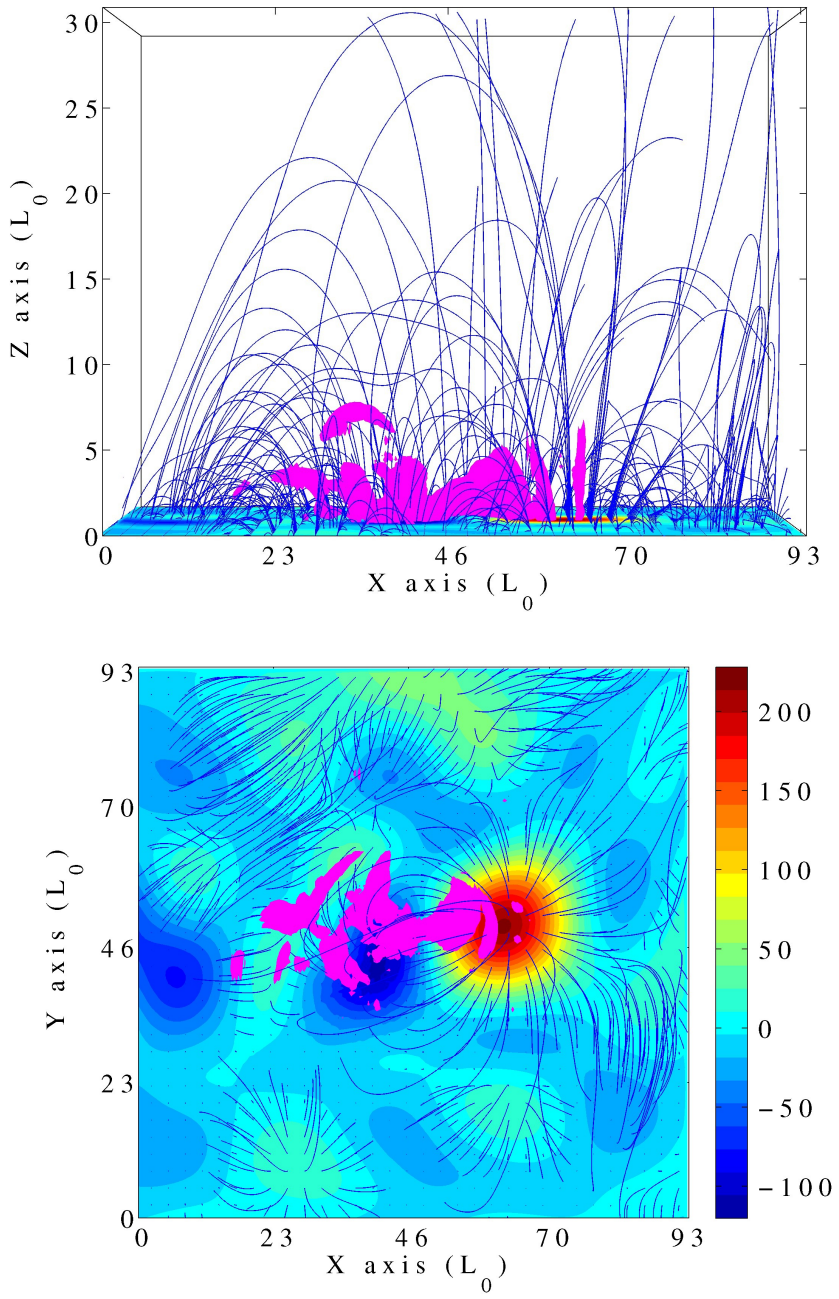

FIGURE 4.12 - Lateral view (top panel) and top view (bottom panel) of the isosurfaces of a parallel current density $j_{\parallel} = 2j_0$, at the instant $t = 1300$ s, resulting from the application of the third velocity pattern as boundary condition of the model (right panel of Fig.4.3). The colour code shows the vertical component of the photospheric magnetic field, with the magnetic field values given in G, and the lines correspond to the magnetic field lines of force. The isosurfaces of parallel current density are shown in magenta.

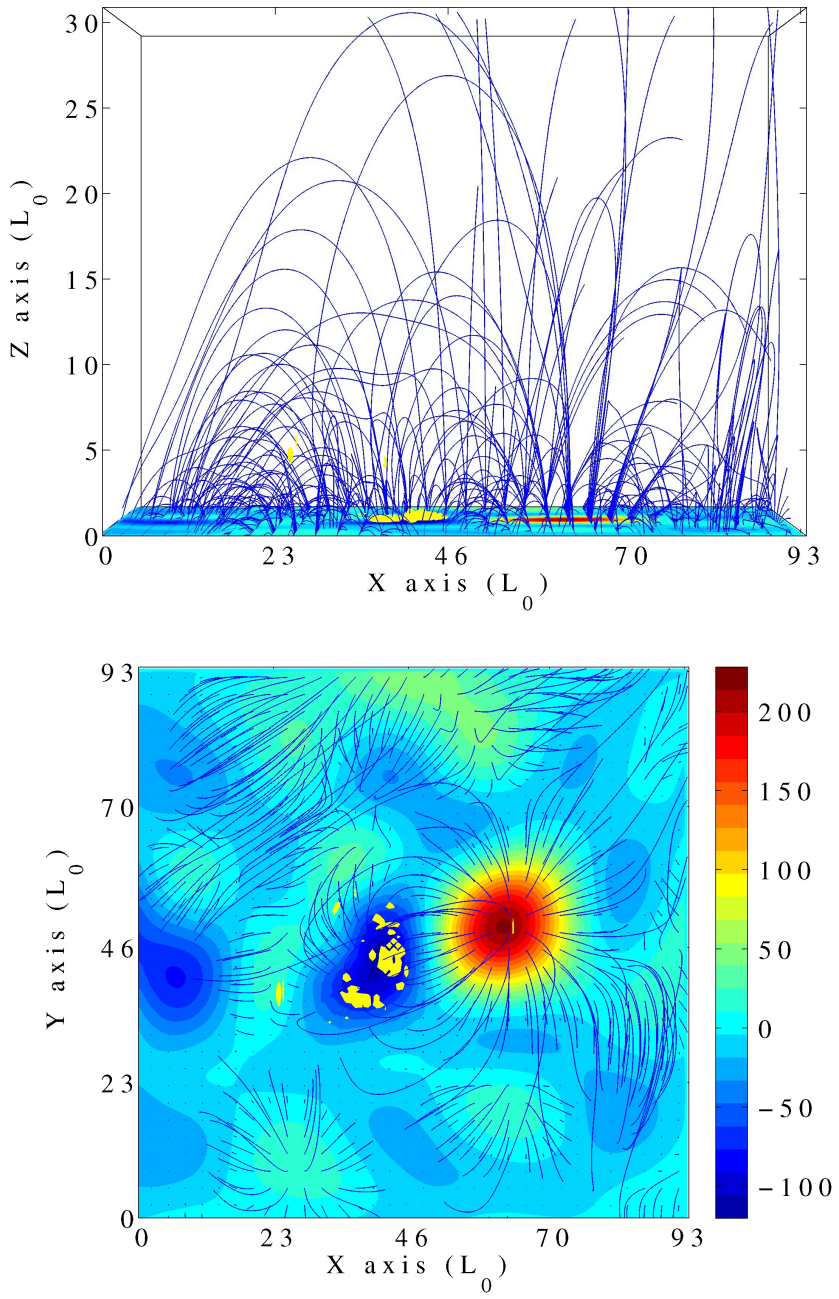

FIGURE 4.13 - Lateral view (top panel) and top view (bottom panel) of the isosurfaces of a perpendicular current density $j_\perp = 2j_0$, at the instant $t = 1300$ s, resulting from the application of the third velocity pattern as boundary condition of the model (right panel of Fig.4.3). The colour code shows the vertical component of the photospheric magnetic field, with the magnetic field values given in G, and the lines correspond to the magnetic field lines of force. The isosurfaces of perpendicular current density are shown in yellow.

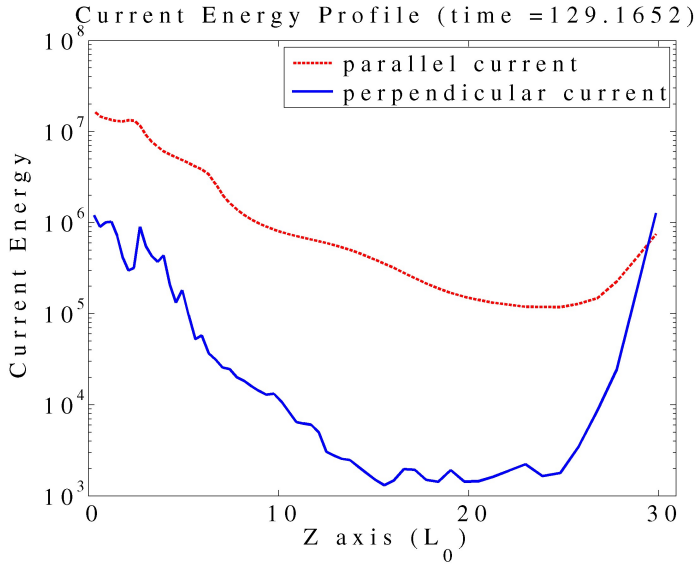

FIGURE 4.14 - Height profile of the current energy obtained using the third velocity pattern at $t = 1300$ s.

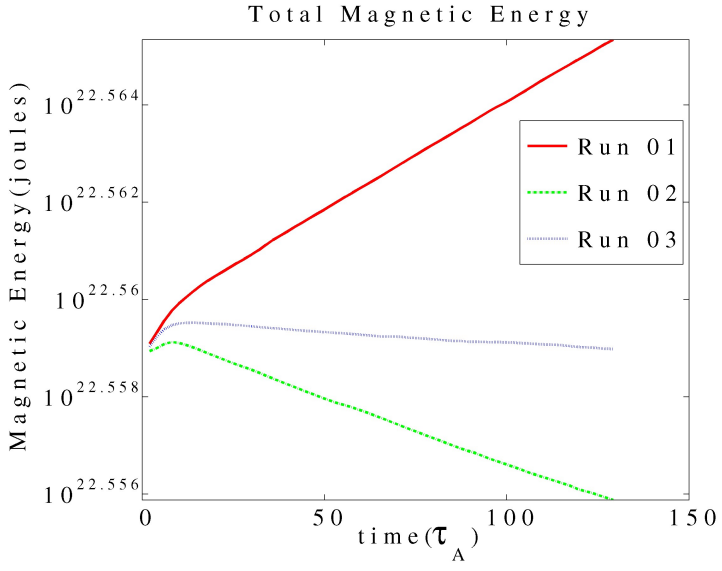

FIGURE 4.15 - Total magnetic energy (joules) versus time (τ_A). The different runs correspond to the application of the different velocity patterns as a boundary condition to the model. The Alfén time (τ_A) is equal to 10 s.

the anomalous resistivity is suggested in (Roussev et al., 2002) as

$$\eta' = \begin{cases} \eta_a \left(\frac{v_{cc}}{v_{th}} - 1 \right) & \text{if } v_{cc} \geq v_{th} \\ 0 & \text{if } v_{cc} < v_{th} \end{cases} \tag{4.3}$$

where v_{th} is a threshold speed of the order of the mean thermal speed of electrons and η_a is a normalized value of the anomalous resistivity.

As showed in (Roussev et al., 2002), the anomalous resistivity controls the current and contributes to the heating of plasma together with changes in the magnetic field topology. The continuous switch on and off of the anomalous resistivity in different time instants and different positions, depending on the fulfill of the current carrier velocity criteria, allows the formation of interesting plasma structures such as plasmoids and contributes significantly to the evolution of plasma and magnetic field.

Based on the description above, the places where the anomalous resistivity would probably occur were estimated using the results of the three different simulation cases. The ratio between the current carrier velocity $v_{cc} = \frac{j}{ne}$ and the thermal velocity of the electrons $v_{th} = \sqrt{\frac{2k_bT}{m}}$ is given by

$$\kappa = \frac{j}{\rho} \sqrt{\frac{1}{T}}. \tag{4.4}$$

The regions where κ is larger than 1 are the regions where plasma heating and changes of magnetic field topology are expected to happen. Figures 4.16, 4.17 and 4.18 show the location of the isosurfaces of $\kappa = 1.2$, at the instant $t = 1300$ s. These regions are located in the chromosphere, transition region and corona. They do not correspond exactly to the regions where the strongest currents develop and are spatially more localized than the parallel current systems. When compared to EIT and TRACE images presented in figure 4.1, a good spatial correspondence with the EUV BP region is still present.

4.3 Conclusions

a) Our simulation has shown that horizontal motion of the photospheric plasma gives rise to electric currents mainly in the chromosphere, transition region and lower corona ($z \leq 7.5 \times 10^6$ m).

b) The currents are formed mainly in the chromosphere and just above the region where the motion is applied and above the main concentrations of magnetic field.

c) The currents always appear in the same area, independently of the velocity pattern applied as boundary condition of the model. This result suggests that

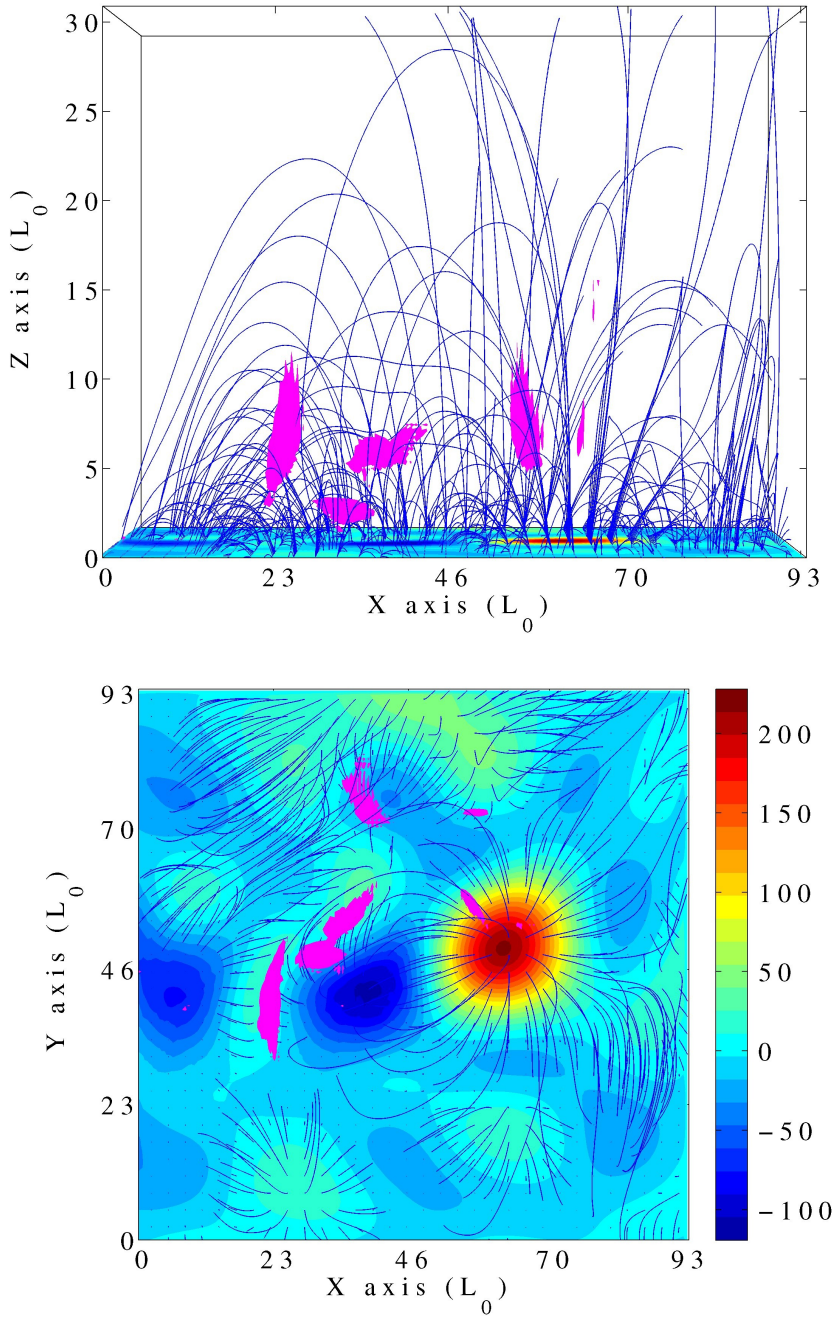

FIGURE 4.16 - Lateral view (top panel) and top view (bottom panel) of the isosurfaces of $\kappa = 1.2$, at the instant $t = 1300$ s, resulting from the application of the first velocity pattern as boundary condition of the model (left panel of Fig.4.3). The colour code shows the vertical component of the photospheric magnetic field, with the magnetic field values given in G, and the lines correspond to the magnetic field lines of force. The isosurfaces of κ are shown in magenta.

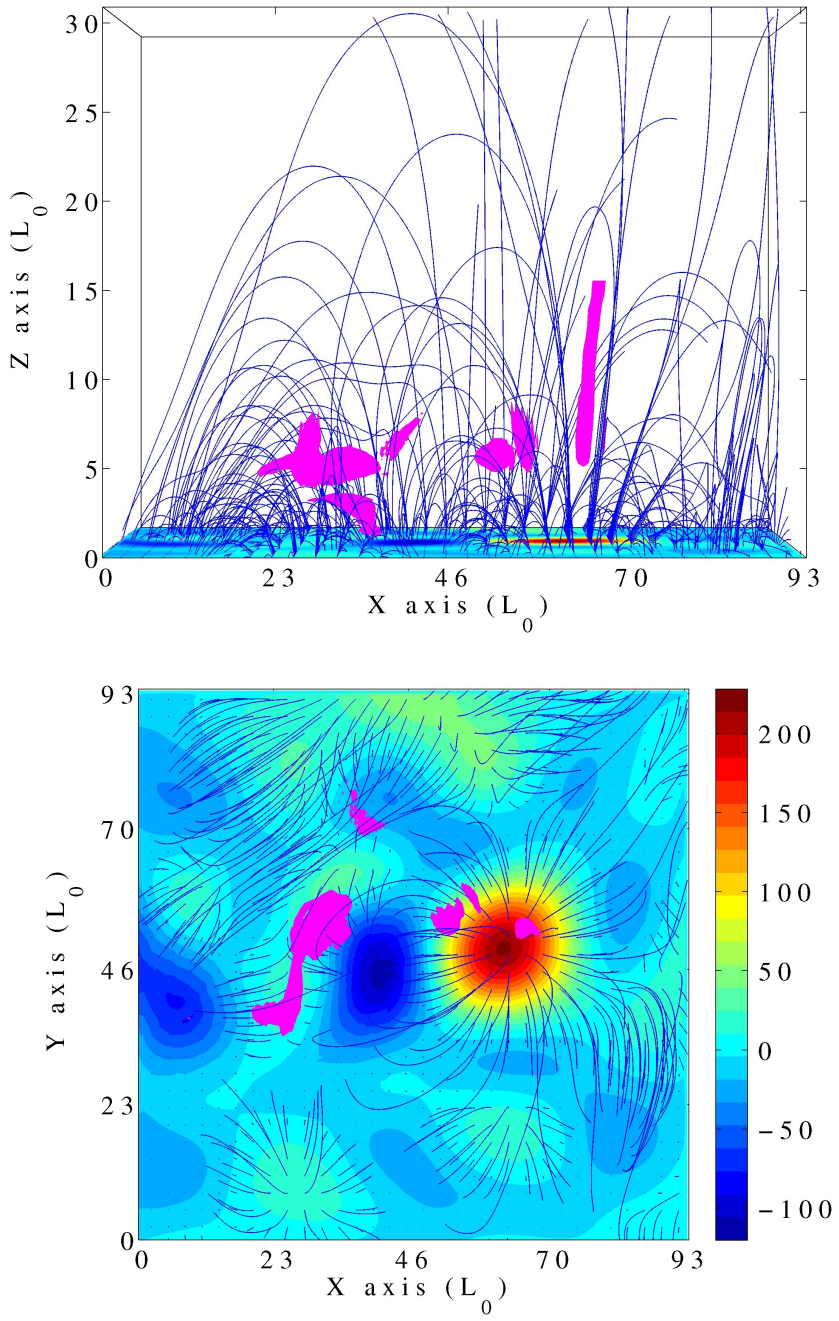

FIGURE 4.17 - Lateral view (top panel) and top view (bottom panel) of the isosurfaces of $\kappa = 1.2$, at the instant $t = 1300$ s, resulting from the application of the second velocity pattern as boundary condition of the model (central panel of Fig.4.3). The colour code shows the vertical component of the photospheric magnetic field, with the magnetic field values given in G, and the lines correspond to the magnetic field lines of force. The isosurfaces of κ are shown in magenta.

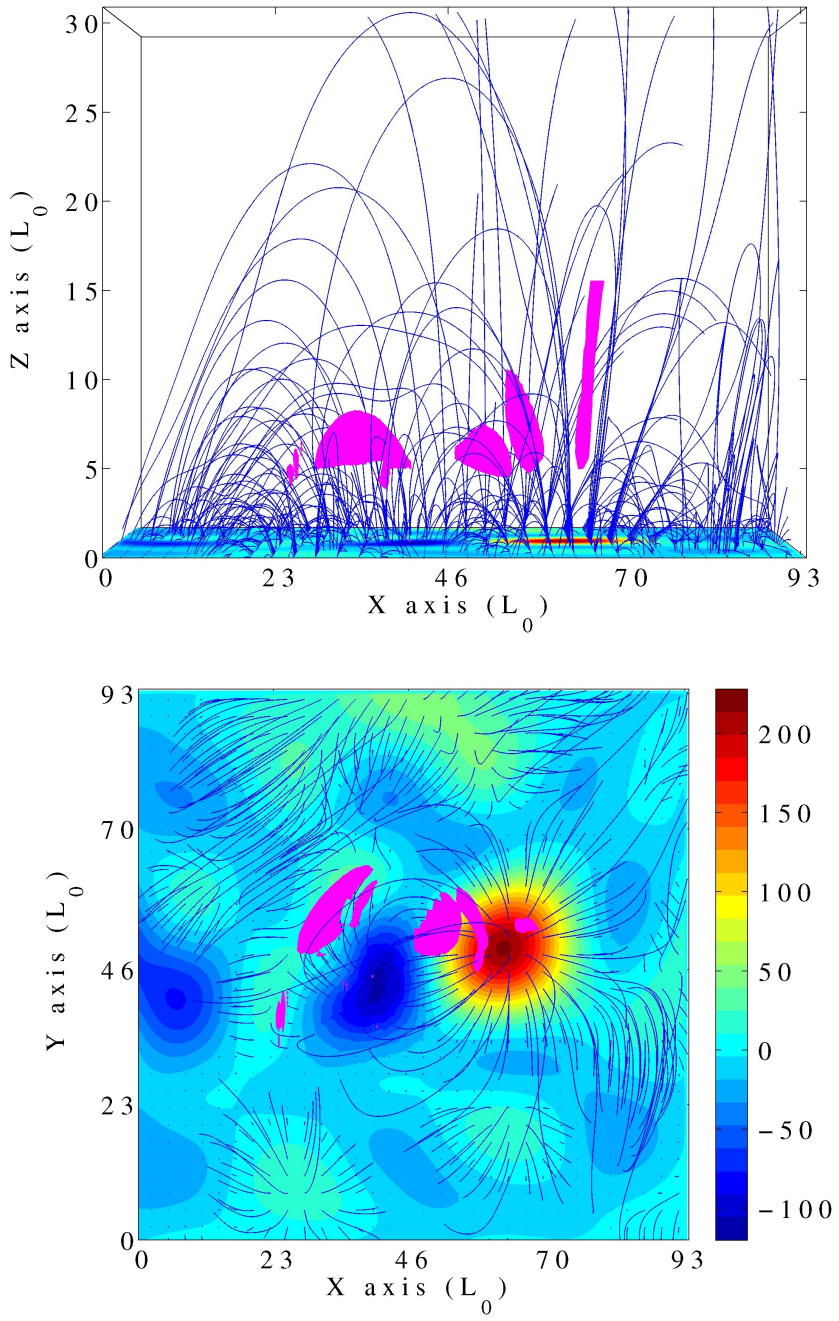

FIGURE 4.18 - Lateral view (top panel) and top view (bottom panel) of the isosurfaces of $\kappa = 1.2$, at the instant $t = 1300$ s, resulting from the application of the third velocity pattern as boundary condition of the model (right panel of Fig.4.3). The colour code shows the vertical component of the photospheric magnetic field, with the magnetic field values given in G, and the lines correspond to the magnetic field lines of force. The isosurfaces of κ are shown in magenta.

there are some preferential places for the development of currents and that these places are determined by the topology of the magnetic field and by the place where the motion is applied, rather than by the specific form of the horizontal velocity pattern.

d) The electric current parallel to the magnetic field is much stronger and spatially more extended than the component perpendicular to the magnetic field, the last appearing as kernels of current concentration.

e) The current energy profile shows that the current density presents the highest values for $z < 7.5 \times 10^6$ m and the energy associated to the parallel current dominates over that associated to the perpendicular current.

f) A comparison with TRACE and EIT data has shown that the area where the current systems are formed coincides with the area where the EUV BP was observed.

g) The results for the ratio between the current carrier velocity and the electron thermal speed show that the regions where this ratio is larger than 1 do not correspond exactly to the regions where the strongest currents appear. These regions extend from the chromosphere to the corona and are spatially more localized than the parallel current systems. A comparison with EIT and TRACE data show that they still present a good spatial correspondence with the location of the EUV BP.

h) The EIT 195 Å and TRACE 1550 Å images showed that the BP consists of bright kernels surrounded by a fainter brightening. The position of the kernel changes with time, while the fainter bright region seems to be located always over the same area. If the mechanism of heating by DC current dissipation is efficient, as suggested by (Büchner; Elkina, 2005; Büchner; Elkina, 2006), this current distribution could explain the appearance of the bright point in the EIT data. The fainter extended brightening could be associated with the heating caused by the distributed system of currents parallel to the magnetic field, and the moving brighter kernels would be associated with the more efficient dissipation of the kernels of current perpendicular to the magnetic field (Birn; Priest, 2007).

5 SUMMARY AND CONCLUSIONS

In this dissertation, a 'data driven' 3D numerical MHD simulation model was used to describe the evolution of currents in the solar atmosphere based on the observed evolution of photospheric magnetic fields. This model has the novelty of using as initial condition the magnetic field extrapolated from the measured LOS component of the photospheric magnetic field. It uses the motion of the solar neutral gas to drive the evolution of the system, in accordance with the observed photospheric B-field evolution. The neutral gas and plasma have the same velocity in the photosphere and are coupled in the chromosphere by means of a collision term in the momentum equation. We studied the effect of different horizontal patterns of motion in the photosphere and chromosphere for the development of electric currents in a region associated to an EUV BP, detected by EIT and TRACE on 2006 Jan 19.

BPs are a directly observable phenomenon of the solar atmosphere heating. At the moment there are two mechanisms that could explain why they occur: wave (AC) heating and electric current (DC) heating. The energy source of both mechanisms is the photospheric kinetic energy reservoir. AC heating requires that the magnetic field is moved around in the solar photosphere faster than the Alfvén crossing time. Waves are generated in this process which must then be dissipated in the solar corona to generate heat. DC heating requires plasma motions in the photosphere at timescales longer than the Alfvén crossing time. Such motions generate currents that can be dissipated and heat the plasma through joule heating.

DC heating models developed until now explain the observed features associated with BPs by an interaction between the magnetic field of a moving bipolar magnetic feature and the surrounding magnetic field for the generation of electric currents. The intensification of the electric currents generated in this way can even lead to the occurrence of reconnection, where free magnetic energy is converted to heat. However, these models do not consider the role of the plasma moving through regions of strongly diverging magnetic flux. *The objective of this work was to investigate whether horizontal plasma motion in the photosphere and chromosphere cause the formation electric currents in the solar atmosphere, at the position of an EUV BP, whether they can be dissipated to power the BP and their possible dependence on the specific pattern of motion.*

The first part of the work was devoted to investigate and compare methods to determine the initial condition and the boundary conditions from solar observations. The methods were applied to a specific case of observed BP. Firstly, the LOS component of the photospheric magnetic field, observed on 2006 Jan 19 at 16:00 UT, was filtered using a Fourier

filter and the small spatial scale variations were removed. The filtered magnetic field was then used as a boundary condition for a potential extrapolation, giving as result the initial configuration of the magnetic field used in the simulation. Secondly, the plasma velocities responsible for the evolution of the magnetic structures present in the filtered LOS photospheric magnetograms were determined. The time interval selected for the study ranged from 16:00 UT to 17:30 UT. This interval was subdivided into segments of 30 minutes. The velocity fields responsible for the evolution of the magnetic structures for each interval were determined using the local correlation tracking technique. *The resulting velocity showed that in the interval between 16:00 UT and 17:30 UT three different patterns of motion contributed to the evolution of the magnetic bipole: shear motion, converging motion and fragmentation of the negative polarity.*

The second part of the work was devoted to study the consequences of the different patterns of motion, obtained from the evolution of the magnetic bipole, to the development of electric currents in the solar atmosphere over the BP region. Three different cases of motion pattern were chosen. We started from the same initial condition and used three different velocity patterns as boundary condition:

- In the first run, the negative polarity is moved away from the positive polarity. This motion pattern stretches the magnetic flux tubes, increasing their magnetic energy contents.
- In the second run, the negative polarity is moved in the direction toward the positive polarity region. This lead to a decrease of the total magnetic flux (flux cancelation).
- In the third run, the negative flux concentration break apart. Part of it is moved away from the positive polarity and the other part in the direction toward the positive polarity.

The results of the simulations have shown that all three patterns of horizontal motion of the photospheric plasma gives rise to electric currents practically in the same position of the chromosphere, transition region and lower corona ($z \leq 7.5 \times 10^6$ m). The currents are maximum in the chromosphere, just above the region where the motion is applied and above the main concentrations of the photospheric magnetic field. The electric currents always appear in the same area, independent of the velocity pattern applied as boundary condition of the model. This last result suggests that there are some preferential places for the development of currents and that these places are determined by the topology of the magnetic field and by the place where the motion is applied, rather than by the specific

form of the horizontal velocity pattern. A comparison with TRACE and EIT data has shown that the area where the current systems are formed coincides with the area where the EUV BP is located.

Another result is concerned with relative importance of parallel and perpendicular components of the electric current. The electric current parallel to the magnetic field is much stronger and spatially more extended than the component perpendicular to the magnetic field. The last appears as kernels of the current concentrations. The analysis of the current energy profile also shows that the energy associated with the parallel current dominates over that associated with the perpendicular current and that the current density presents the highest values for $z < 7.5 \times 10^6$ m. *These facts confirm the observations that the magnetic field in the solar atmosphere is mainly force-free and indicates that deviations of the force-free state occur in localized regions, low rising in the solar atmosphere.*

Based on the results described above, it is reasonable to suggest that the electric currents generated by the horizontal motion in the solar photosphere and chromosphere could be dissipated and give rise to the bright point observed on 2006 Jan 19. However, there are two questions that make the direct relation between electric current and solar brightening not so simple: 1) Is the resistivity in the solar atmosphere high enough to dissipate the currents? 2) Is the DC heating produced by the current dissipation suffice to heat the plasma to the observed temperatures? The answer for the first question can be given, since the classical resistivity is not sufficient, only by considering plasma instabilities beyond the MHD approach, that can increase the resistivity in the solar atmosphere up to six orders of magnitude. This resistivity is known as anomalous resistivity. The second question is not so simple to answer. Since the joule heating is proportional to the product of the resistivity by the square of the electric current, the correct treatment of this term depends very much at the *'ab initio'* formulation used for the plasma resistivity. This *'ab initio'* formulation for the resistivity is derived from small scale studies of the solar plasma, obtained using Vlasov and particle simulations, and it is a current state of art in solar physics research. Further, the find temperature distribution in the solar atmosphere also depend very much on the energy distribution, e.g. by heat conduction and thermal radiative cooling. So, different contributions to the energy equation can provide different temperature distributions.

In this sense, the direction for the future work can be suggested as:

- Improve the energy equation by considering effects as radiative cooling and heat conduction;

- Test different *'ab initio'* formulations for the anomalous resistivity;
- To apply the model to regions of strong magnetic field (active regions) responsible for more energetic phenomena (solar flares);
- Consider the effects of the anisotropies imposed by the presence of strong magnetic field;
- Finally, to use the output of the model to perform forward modeling and compare directly the results with observations.

REFERENCES

Alfvén, H. Magneto hydrodynamic waves, and the heatinhg of the solar corona. **Monthly Notices of the Royal Astronomical Society**, v. 107, p. 211–+, 1947. 101

Aulanier, G.; Pariat, E.; Démoulin, P. Current sheet formation in quasi-separatrix layers and hyperbolic flux tubes. **Astronomy and Astrophysics**, v. 444, p. 961–976, dez. 2005. 106

Birn, J.; Priest, E. R. **Reconnection of magnetic fields : magnetohydrodynamics and collisionless theory and observations**. [S.l.]: Reconnection of magnetic fields : magnetohydrodynamics and collisionless theory and observations / edited by J. Birn and E. R. Priest. Cambridge : Cambridge University Press, 2007. ISBN: 9780521854207 (hbk.), 2007. 101, 121

Brown, D. S.; Parnell, C. E.; Deluca, E. E.; Golub, L.; McMullen, R. A. The Magnetic Structure of a Coronal X-Ray Bright Point. **Solar Physics**, v. 201, p. 305–321, jul. 2001. 101

Büchner, J. Locating Current Sheets in the Solar Corona. **Space Science Reviews**, v. 122, p. 149–160, fev. 2006. 101, 106

Büchner, J.; Elkina, N. Vlasov Code Simulation of Anomalous Resistivity. **Space Science Reviews**, v. 121, p. 237–252, nov. 2005. 101, 121

_____. Anomalous resistivity of current-driven isothermal plasmas due to phase space structuring. **Physics of Plasmas**, v. 13, p. 2304–+, ago. 2006. 101, 121

Büchner, J.; Nikutowski, B.; Otto, A. Coronal Heating by Transition Region Reconnection. In: Walsh, R. W.; Ireland, J.; Danesy, D.; Fleck, B. (Ed.). **SOHO 15 Coronal Heating**. [S.l.: s.n.], 2004. (ESA Special Publication, v. 575), p. 23–+. 57, 87, 101, 102

_____. Magnetic coupling of photosphere and corona: MHD simulation for multi-wavelength observations. In: Stepanov, A. V.; Benevolenskaya, E. E.; Kosovichev, A. G. (Ed.). **Multi-Wavelength Investigations of Solar Activity**. [S.l.: s.n.], 2004. (IAU Symposium, v. 223), p. 353–356. 101

Davis, J. M. X-ray bright points and the sunspot cycle - Further results and predictions. **Solar Physics**, v. 88, p. 337–342, out. 1983. 15, 37, 39

Démoulin, P.; Berger, M. A. Magnetic Energy and Helicity Fluxes at the Photospheric Level. **Solar Physics**, v. 215, p. 203–215, ago. 2003. 60, 104

Démoulin, P.; Henoux, J. C.; Priest, E. R.; Mandrini, C. H. Quasi-Separatrix layers in solar flares. I. Method. **Astronomy and Astrophysics**, v. 308, p. 643–655, abr. 1996. 106

Démoulin, P.; Priest, E. R.; Lonie, D. P. Three-dimensional magnetic reconnection without null points 2. Application to twisted flux tubes. **Journal of Geophysical Research**, v. 101, p. 7631–7646, abr. 1996. 106

Devore, C. R. Flux-corrected transport techniques for multidimensional compressible magnetohydrodynamics. **Journal of Computational Physics**, v. 92, p. 142–160, jan. 1991. 98

Georgoulis, M. K.; LaBonte, B. J. Reconstruction of an Inductive Velocity Field Vector from Doppler Motions and a Pair of Solar Vector Magnetograms. **The Astrophysical Journal**, v. 636, p. 475–495, jan. 2006. 59

Golub, L. X-ray bright points and the solar cycle. **Royal Society of London Philosophical Transactions Series A**, v. 297, p. 595–604, jul. 1980. 101

Golub, L.; Davis, J. M.; Krieger, A. S. Anticorrelation of X-ray bright points with sunspot number, 1970-1978. **The Astrophysical Journal**, v. 229, p. L145–L150, maio 1979. 15, 29, 35, 38, 39

Golub, L.; Krieger, A. S.; Harvey, J. W.; Vaiana, G. S. Magnetic properties of X-ray bright points. **Solar Physics**, v. 53, p. 111–121, jul. 1977. 29, 35, 42

Golub, L.; Krieger, A. S.; Silk, J. K.; Timothy, A. F.; Vaiana, G. S. Solar X-Ray Bright Points. **The Astrophysical Journal**, v. 189, p. L93+, abr. 1974. 15, 29, 30, 31

Golub, L.; Krieger, A. S.; Vaiana, G. S. Observation of a non-uniform component in the distribution of coronal bright points. **Solar Physics**, v. 42, p. 131–134, maio 1975. 15, 29, 31, 32, 33, 34

_____. Distribution of lifetimes for coronal soft X-ray bright points. **Solar Physics**, v. 49, p. 79–90, jul. 1976. 15, 29, 32, 34

_____. Observation of spatial and temporal variations in X-ray bright point emergence patterns. **Solar Physics**, v. 50, p. 311–327, dez. 1976. 15, 29, 35, 36, 37, 38

Gudiksen, B. V.; Nordlund, Å. An Ab Initio Approach to the Solar Coronal Heating Problem. **The Astrophysical Journal**, v. 618, p. 1020–1030, jan. 2005. 57

Habbal, S. R. Coronal energy distribution and X-ray activity in the small scale magnetic field of the quiet sun. **Annales Geophysicae**, v. 10, p. 34–46, fev. 1992. 101

Habbal, S. R.; Harvey, K. L. Simultaneous observations of 20 centimeter bright points and He I 10830 A dark points in the quiet sun. **The Astrophysical Journal**, v. 326, p. 988–996, mar. 1988. 40

Habbal, S. R.; Withbroe, G. L.; Dowdy JR., J. F. A comparison between bright points in a coronal hole and a quiet-sun region. **The Astrophysical Journal**, v. 352, p. 333–342, mar. 1990. 40

Harvey, K. L. The relationship between coronal bright points as seen in He I Lambda 10830 and the evolution of the photospheric network magnetic fields. **Australian Journal of Physics**, v. 38, p. 875–883, 1985. 40

Harvey, K. L.; Harvey, J. W.; Martin, S. F. Ephemeral active regions in 1970 and 1973. **Solar Physics**, v. 40, p. 87–102, jan. 1975. 35, 42

Harvey, K. L.; Strong, K. S.; Nitta, N.; Tsuneta, S. Are X-Ray Bright Points the Signature of Magnetic Field Reconnection? In: Balasubramaniam, K. S.; Simon, G. W. (Ed.). **Solar Active Region Evolution: Comparing Models with Observations**. [S.l.: s.n.], 1994. (Astronomical Society of the Pacific Conference Series, v. 68), p. 377–+. 40

Harvey, K. L.; Strong, K. T.; Nitta, N.; Tsuneta, S. Lifetimes and distribution of coronal bright points observed with Yohkoh. **Advances in Space Research**, v. 13, p. 27–30, set. 1993. 15, 40, 41

Krieger, A. S.; Vaiana, G. S.; van Speybroeck, L. P. The X-Ray Corona and the Photospheric Magnetic Field. In: Howard, R. (Ed.). **Solar Magnetic Fields**. [S.l.: s.n.], 1971. (IAU Symposium, v. 43), p. 397–+. 35, 42

Kusano, K.; Maeshiro, T.; Yokoyama, T.; Sakurai, T. Measurement of Magnetic Helicity Injection and Free Energy Loading into the Solar Corona. **The Astrophysical Journal**, v. 577, p. 501–512, set. 2002. 57, 61, 62, 65, 68

Leese, J.; Novak, C.; Taylor, V. The Determination of Cloud Pattern Motions from Geosynchronous Satellite Image Data. **Pattern Recognition**, v. 2, n. 4, p. 279–280, dez. 1970. 58

Leese, J. A.; Novak, C. S.; Clark, B. B. An Automated Technique for Obtaining Cloud Motion from Geosynchronous Satellite Data Using Cross Correlation. **Journal of Applied Meteorology**, v. 10, p. 118–132, fev. 1971. 58

Longcope, D. W. A Model for Current Sheets and Reconnection in X-Ray Bright Points. **The Astrophysical Journal**, v. 507, p. 433–442, nov. 1998. 16, 50, 52, 53, 55, 56, 101

_____. Inferring a Photospheric Velocity Field from a Sequence of Vector Magnetograms: The Minimum Energy Fit. **The Astrophysical Journal**, v. 612, p. 1181–1192, set. 2004. 57, 60, 67, 68, 69, 70, 71, 73, 75, 76, 79, 80

Madjarska, M. S.; Doyle, J. G.; Teriaca, L.; Banerjee, D. An EUV Bright Point as seen by SUMER, CDS, MDI and EIT on-board SoHO. **Astronomy and Astrophysics**, v. 398, p. 775–784, fev. 2003. 101

Mandrini, C. H.; Démoulin, P.; van Driel-Gesztelyi, L.; Schmieder, B.; Cauzzi, G.; Hofmann, A. 3D Magnetic Reconnection at an X-Ray Bright Point. **Solar Physics**, v. 168, p. 115–133, set. 1996. 50

Marsh, K. A.; Hurford, G. J.; Zirin, H. VLA observations of spatial structure in the quiet sun at 6 centimeters, during the 1977 October eclipse. **The Astrophysical Journal**, v. 236, p. 1017–1025, mar. 1980. 40

Mickey, D. L.; Canfield, R. C.; Labonte, B. J.; Leka, K. D.; Waterson, M. F.; Weber, H. M. The Imaging Vector Magnetograph at Haleakala. **Solar Physics**, v. 168, p. 229–250, out. 1996. 70

November, L. J.; Simon, G. W. Precise proper-motion measurement of solar granulation. **The Astrophysical Journal**, v. 333, p. 427–442, out. 1988. 57, 58, 102

Otto, A.; Büchner, J.; Nikutowski, B. Force-free magnetic field extrapolation for MHD boundary conditions in simulations of the solar atmosphere. **Astronomy and Astrophysics**, v. 468, p. 313–321, jun. 2007. 19, 91, 96

Parker, E. N. Topological Dissipation and the Small-Scale Fields in Turbulent Gases. **The Astrophysical Journal**, v. 174, p. 499–+, jun. 1972. 101

Parnell, C. E.; Priest, E. R.; Golub, L. The three-dimensional structures of X-ray bright points. **Solar Physics**, v. 151, p. 57–74, abr. 1994. 50

Parnell, C. E.; Priest, E. R.; Titov, V. S. A model for X-ray bright points due to unequal cancelling flux sources. **Solar Physics**, v. 153, p. 217–235, ago. 1994. 16, 49, 51, 52, 101

Peter, H.; Gudiksen, B. V.; Nordlund, Å. Forward Modeling of the Corona of the Sun and Solar-like Stars: From a Three-dimensional Magnetohydrodynamic Model to Synthetic Extreme-Ultraviolet Spectra. **The Astrophysical Journal**, v. 638, p. 1086–1100, fev. 2006. 57

Pohjolainen, S.; Maia, D.; Pick, M.; Vilmer, N.; Khan, J. I.; Otruba, W.; Warmuth, A.; Benz, A.; Alissandrakis, C.; Thompson, B. J. On-the-Disk Development of the Halo

Coronal Mass Ejection on 1998 May 2. **The Astrophysical Journal**, v. 556, p. 421–431, jul. 2001. 70

POTTER, D. **Computational Physics**. 1. ed. [S.l.]: John Wiley and Sons, 1973. 98

Priest, E. R.; Parnell, C. E.; Martin, S. F. A converging flux model of an X-ray bright point and an associated canceling magnetic feature. **The Astrophysical Journal**, v. 427, p. 459–474, maio 1994. 15, 16, 45, 46, 47, 48, 49, 50, 101

Régnier, S.; Canfield, R. C. Evolution of magnetic fields and energetics of flares in active region 8210. **Astronomy and Astrophysics**, v. 451, p. 319–330, maio 2006. 70

Roussev, I.; Galsgaard, K.; Judge, P. G. Physical consequences of the inclusion of anomalous resistivity in the dynamics of 2D magnetic reconnection. **Astronomy and Astrophysics**, v. 382, p. 639–649, fev. 2002. 93, 117

Sattarov, I.; Pevtsov, A. A.; Hojaev, A. S.; Sherdonov, C. T. X-Ray Bright Points and Photospheric Bipoles during Cycles 22 and 23. **The Astrophysical Journal**, v. 564, p. 1042–1047, jan. 2002. 101

Scherrer, P. H.; Bogart, R. S.; Bush, R. I.; Hoeksema, J. T.; Kosovichev, A. G.; Schou, J.; Rosenberg, W.; Springer, L.; Tarbell, T. D.; Title, A.; Wolfson, C. J.; Zayer, I.; MDI Engineering Team. The Solar Oscillations Investigation - Michelson Doppler Imager. **Solar Physics**, v. 162, p. 129–188, dez. 1995. 70

Schuck, P. W. Local Correlation Tracking and the Magnetic Induction Equation. **The Astrophysical Journal**, v. 632, p. L53–L56, out. 2005. 60

Schuessler, M. Flux tube dynamo approach to the solar cycle. **Nature**, v. 288, p. 150–152, nov. 1980. 37, 40

Seehafer, N. Determination of constant alpha force-free solar magnetic fields from magnetograph data. **Solar Physics**, v. 58, p. 215–223, jul. 1978. 91

Sheeley JR., N. R.; Golub, L. Rapid changes in the fine structure of a coronal 'bright point' and a small coronal 'active region'. **Solar Physics**, v. 63, p. 119–126, ago. 1979. 40

Sterling, A. C.; Moore, R. L. EIT Crinkles as Evidence for the Breakout Model of Solar Eruptions. **The Astrophysical Journal**, v. 560, p. 1045–1057, out. 2001. 70

_____. Internal and external reconnection in a series of homologous solar flares. **Journal of Geophysical Research**, v. 106, p. 25227–25238, nov. 2001. 70

Sterling, A. C.; Moore, R. L.; Qiu, J.; Wang, H. Hα Proxies for EIT Crinkles: Further Evidence for Preflare "Breakout"-Type Activity in an Ejective Solar Eruption. **The Astrophysical Journal**, v. 561, p. 1116–1126, nov. 2001. 70

Thompson, B. J.; Cliver, E. W.; Nitta, N.; Delannée, C.; Delaboudinière, J.-P. Coronal Dimmings and Energetic CMEs in April-May 1998. **Geophysical Research Letters**, v. 27, p. 1431–1434, maio 2000. 70

Tur, T. J.; Priest, E. R. The formation of current sheets during the emergence of new magnetic flux from below the photosphere. **Solar Physics**, v. 48, p. 89–100, maio 1976. 15, 42, 43, 44

Ugarte-Urra, I.; Doyle, J. G.; Madjarska, M. S.; O'Shea, E. Signature of oscillations in coronal bright points. **Astronomy and Astrophysics**, v. 418, p. 313–324, abr. 2004. 101

Vaiana, G. S.; Krieger, A. S.; van Speybroeck, L. P.; Zehnpfennig, T. **Bull. Am. Phys. Soc.**, v. 15, p. 611, 1970. 29

von Rekowski, B.; Parnell, C. E.; Priest, E. R. Solar coronal heating by magnetic cancellation - II. Disconnected and unequal bipoles. **Monthly Notices of the Royal Astronomical Society**, v. 369, p. 43–56, jun. 2006. 101

Wang, T.; Yan, Y.; Wang, J.; Kurokawa, H.; Shibata, K. The Large-Scale Coronal Field Structure and Source Region Features for a Halo Coronal Mass Ejection. **The Astrophysical Journal**, v. 572, p. 580–597, jun. 2002. 70

Warmuth, A.; Hanslmeier, A.; Messerotti, M.; Cacciani, A.; Moretti, P. F.; Otruba, W. NOAA AR 8210: Evolution and Flares from Multiband Diagnostics. **Solar Physics**, v. 194, p. 103–120, maio 2000. 70

Webb, D. F. Small-scale coronal structure, part 3. In: Poland, A. I. (Ed.). **Coronal and Prominence Plasmas**. [S.l.: s.n.], 1986. p. 329–342. 101

Webb, D. F.; Martin, S. F.; Moses, D.; Harvey, J. W. The correspondence between X-ray bright points and evolving magnetic features in the quiet sun. **Solar Physics**, v. 144, p. 15–35, mar. 1993. 40

Welsch, B. T.; Fisher, G. H.; Abbett, W. P.; Regnier, S. ILCT: Recovering Photospheric Velocities from Magnetograms by Combining the Induction Equation with Local Correlation Tracking. **The Astrophysical Journal**, v. 610, p. 1148–1156, ago. 2004. 57, 59, 60, 61, 65, 66, 67, 68, 70, 71, 73

Wu, S. T.; Wang, A. H.; Liu, Y.; Hoeksema, J. T. Data-driven Magnetohydrodynamic Model for Active Region Evolution. **The Astrophysical Journal**, v. 652, p. 800–811, nov. 2006. 57

Yoshimura, H. Solar cycle dynamo wave origin of sunspot intensity and X-ray bright point number variation. **Solar Physics**, v. 87, p. 251–259, set. 1983. 37

A APPENDIX A - NORMALIZATION OF THE MHD EQUATIONS

Continuity equation

$$\begin{aligned}
\frac{\partial \rho}{\partial t} &= -\vec{\nabla}\cdot\rho\vec{u} \Rightarrow \\
\frac{\rho_0}{\tau_0}\frac{\partial \rho'}{\partial t'} &= -\frac{\rho_0 u_0}{L_0}\vec{\nabla}\cdot\rho'\vec{u}' \Rightarrow \\
\frac{\partial \rho'}{\partial t'} &= -\vec{\nabla}\cdot\rho'\vec{u}'
\end{aligned} \tag{A.1}$$

Momentum equation

$$\begin{aligned}
\frac{\partial \rho\vec{u}}{\partial t} &= -\vec{\nabla}\cdot\Big[\rho\vec{u}\vec{u} + \Big(p + \frac{B^2}{2\mu_0}\Big)\underline{\underline{1}} - \frac{\vec{B}\vec{B}}{\mu_0}\Big] - \nu\rho(\vec{u}-\vec{u}_0) \Rightarrow \\
\frac{\rho_0 u_0}{\tau_0}\frac{\partial \rho'\vec{u}'}{\partial t'} &= -\frac{1}{L_0}\vec{\nabla}\cdot\Big[\rho_0 u_0^2\rho'\vec{u}'\vec{u}' + \Big(p_0 p' + \frac{B_0^2 B'^2}{2\mu_0}\Big)\underline{\underline{1}} \\
&- \frac{B_0^2\vec{B}'\vec{B}'}{\mu_0}\Big] - \frac{\rho_0 u_0}{\tau_0}\nu'\rho'(\vec{u}'-\vec{u}_0') \Rightarrow \\
\frac{\partial \rho'\vec{u}'}{\partial t'} &= -\vec{\nabla}\cdot\Big[\frac{\rho_0 u_0^2}{\rho_0 u_0^2}\rho'\vec{u}'\vec{u}' + \Big(\frac{p_0}{\rho_0 u_0^2}p' + \frac{B_0^2}{\rho_0 u_0^2}\frac{B'^2}{2\mu_0}\Big)\underline{\underline{1}} \\
&- \frac{B_0^2}{\rho_0 u_0^2}\frac{\vec{B}'\vec{B}'}{\mu_0}\Big] - \nu'\rho'(\vec{u}'-\vec{u}_0') \Rightarrow \\
\frac{\partial \rho'\vec{u}'}{\partial t'} &= -\vec{\nabla}\cdot\Big[\rho'\vec{u}'\vec{u}' + \Big(\frac{B_0^2}{2\mu_0}\frac{1}{\rho_0 u_0^2}p' + \frac{B_0^2}{2\mu_0}\frac{1}{\rho_0 u_0^2}B'^2\Big)\underline{\underline{1}} \\
&- \frac{B_0^2}{\mu_0}\frac{1}{\rho_0 u_0^2}\vec{B}'\vec{B}'\Big] - \nu'\rho'(\vec{u}'-\vec{u}_0') \Rightarrow \\
\frac{\partial \rho'\vec{u}'}{\partial t'} &= -\vec{\nabla}\cdot\Big[\rho'\vec{u}'\vec{u}' + \Big(\frac{B_0^2}{2\mu_0}\frac{\mu_0\rho_0}{\rho_0 B_0^2}p' + \frac{B_0^2}{2\mu_0}\frac{\mu_0\rho_0}{\rho_0 B_0^2}B'^2\Big)\underline{\underline{1}} \\
&- \frac{B_0^2}{\mu_0}\frac{\rho_0\mu_0}{\rho_0 B_0^2}\vec{B}'\vec{B}'\Big] - \nu'\rho'(\vec{u}'-\vec{u}_0') \Rightarrow \\
\frac{\partial \rho'\vec{u}'}{\partial t'} &= -\vec{\nabla}\cdot\Big[\rho'\vec{u}'\vec{u}' + \frac{1}{2}\Big(p' + B'^2\Big)\underline{\underline{1}} - \vec{B}'\vec{B}'\Big] \\
&- \nu'\rho'(\vec{u}'-\vec{u}_0')
\end{aligned} \tag{A.2}$$

Energy equation

$$\begin{aligned}
\frac{\partial p}{\partial t} &= -\vec{\nabla}\cdot p\vec{u} - (\gamma-1)p\vec{\nabla}\cdot\vec{u} + (\gamma-1)\eta j^2 \Rightarrow \\
\frac{p_0}{\tau_0}\frac{\partial p'}{\partial t'} &= -\frac{p_0 u_0}{L_0}\vec{\nabla}\cdot p'\vec{u}' - \frac{p_0 u_0}{L_0}(\gamma-1)p'\vec{\nabla}\cdot\vec{u}' \\
&+ \frac{\mu_0 L_0 u_0 B_0^2}{\mu_0^2 L_0^2}(\gamma-1)\eta' j'^2 \Rightarrow \\
\frac{\partial p'}{\partial t'} &= -\frac{p_0\tau_0}{p_0\tau_0}\vec{\nabla}\cdot p'\vec{u}' - \frac{p_0\tau_0}{p_0\tau_0}(\gamma-1)p'\vec{\nabla}\cdot\vec{u}' \\
&+ \frac{u_0 B_0^2}{\mu_0 L_0}\frac{\tau_0}{p_0}(\gamma-1)\eta' j'^2 \Rightarrow \\
\frac{\partial p'}{\partial t'} &= \vec{\nabla}\cdot p'\vec{u}' - (\gamma-1)p'\vec{\nabla}\cdot\vec{u}' \\
&+ \frac{u_0 B_0^2}{\mu_0 L_0}\frac{2\tau_0\mu_0}{B_0^2}(\gamma-1)\eta' j'^2 \Rightarrow \\
\frac{\partial p'}{\partial t'} &= \vec{\nabla}\cdot p'\vec{u}' - (\gamma-1)p'\vec{\nabla}\cdot\vec{u}' + 2(\gamma-1)\eta' j'^2
\end{aligned} \tag{A.3}$$

Induction equation

$$\begin{aligned}
\frac{\partial \vec{B}}{\partial t} &= \vec{\nabla}\times(\vec{u}\times\vec{B} - \eta\vec{j}) \Rightarrow \\
\frac{B_0}{\tau_0}\frac{\partial \vec{B}'}{\partial t'} &= \frac{1}{L_0}\vec{\nabla}\times(u_0 B_0\vec{u}'\times\vec{B}' - \eta_0 j_0\eta'\vec{j}') \Rightarrow \\
\frac{\partial \vec{B}'}{\partial t'} &= \frac{1}{B_0 u_0}\vec{\nabla}\times(u_0 B_0\vec{u}'\times\vec{B}' - \frac{B_0}{\mu_0 L_0}\mu_0 L_0 u_0\eta'\vec{j}') \Rightarrow \\
\frac{\partial \vec{B}'}{\partial t'} &= \vec{\nabla}\times(\vec{u}'\times\vec{B}' - \eta'\vec{j}')
\end{aligned} \tag{A.4}$$

Ohm law

$$\begin{aligned}
\vec{E} &= -\vec{u}\times\vec{B} + \eta\vec{j} \Rightarrow \\
E_0\vec{E}' &= -u_0 B_0\vec{u}'\times\vec{B}' + \eta_0 j_0\eta'\vec{j}' \Rightarrow \\
u_0 B_0\vec{E}' &= -u_0 B_0\vec{u}'\times\vec{B}' + \mu_0 L_0 u_0\frac{B_0}{\mu_0 L_0}\eta'\vec{j}' \Rightarrow \\
\vec{E}' &= -\vec{u}'\times\vec{B}' + \eta'\vec{j}'
\end{aligned} \tag{A.5}$$

Ampères law

$$\begin{aligned}
\vec{\nabla} \times \vec{B} &= \mu_0 \vec{j} \Rightarrow \\
\frac{B_0}{L_0} \vec{\nabla} \times \vec{B'} &= \mu_0 j_0 \vec{j'} \Rightarrow \\
\vec{\nabla} \times \vec{B'} &= \frac{L_0}{B_0} \mu_0 \frac{B_0}{\mu_0 L_0} \Rightarrow \\
\vec{\nabla} \times \vec{B'} &= \vec{j'}
\end{aligned} \tag{A.6}$$

B APPENDIX B - DISCRETIZATION OF THE MHD EQUATIONS USING FTCS SCHEME

Continuity equation

$$\begin{aligned}\rho^{n+1}_{i,j,k} &= \rho^{n}_{i,j,k} - \Delta t\Big[\frac{1}{2\Delta x}\Big(\rho^{n}_{i+1,j,k}u^{n}_{x_{i+1,j,k}} - \rho^{n}_{i-1,j,k}u^{n}_{x_{i-1,j,k}}\Big)\\ &+ \frac{1}{2\Delta y}\Big(\rho^{n}_{i,j+1,k}u^{n}_{y_{i,j+1,k}} - \rho^{n}_{i,j-1,k}u^{n}_{y_{i,j-1,k}}\Big)\\ &+ \frac{1}{2\Delta z}\Big(\rho_{i,j,k+1}nu^{n}_{z_{i,j,k+1}} - \rho_{i,j,k-1}nu^{n}_{z_{i,j,k-1}}\Big)\Big] \end{aligned} \tag{B.1}$$

X-component of the momentum equation

$$\begin{aligned}\rho^{n+1}_{i,j,k}u^{n+1}_{x_{i,j,k}} &= \rho^{n}_{i,j,k}u^{n}_{x_{i,j,k}} - \Delta t\Bigg\{\frac{1}{2\Delta x}\Big[\rho^{n}_{i+1,j,k}u^{n}_{x_{i+1,j,k}}u^{n}_{x_{i+1,j,k}} - \rho^{n}_{i-1,j,k}u^{n}_{x_{i-1,j,k}}u^{n}_{x_{i-1,j,k}}\\ &+ \frac{1}{2}\Big(p^{n}_{i+1,j,k} + B^{2^n}_{i+1,j,k}\Big) - \frac{1}{2}\Big(p^{n}_{i-1,j,k} + B^{2^n}_{i-1,j,k}\Big)\\ &- B^{n}_{x_{i+1,j,k}}B^{n}_{x_{i+1,j,k}} + B^{n}_{x_{i-1,j,k}}B^{n}_{x_{i-1,j,k}}\Big]\\ &+ \frac{1}{2\Delta y}\Big[\rho^{n}_{i,j+1,k}u^{n}_{y_{i,j+1,k}}u^{n}_{x_{i,j+1,k}} - \rho^{n}_{i,j-1,k}u^{n}_{y_{i,j-1,k}}u^{n}_{x_{i,j-1,k}}\\ &- B^{n}_{y_{i,j+1,k}}B^{n}_{x_{i,j+1,k}} + B^{n}_{y_{i,j-1,k}}B^{n}_{x_{i,j-1,k}}\Big]\\ &+ \frac{1}{2\Delta z}\Big[\rho^{n}_{i,j,k+1}u_{z_{i,j,k+1}}u^{n}_{x_{i,j,k+1}} - \rho^{n}_{i,j,k-1}u^{n}_{z_{i,j,k-1}}u^{n}_{x_{i,j,k-1}}\\ &- B^{n}_{z_{i,j,k+1}}B^{n}_{x_{i,j,k+1}} + B^{n}_{z_{i,j,k-1}}B^{n}_{x_{i,j,k-1}}\Big]\\ &+ \mu\rho^{n}_{i,j,k}\Big(u^{n}_{x_{i,j,k}} - u^{n}_{xN_{i,j,k}}\Big)\Bigg\} \end{aligned} \tag{B.2}$$

Y-Component of the momentum equation

$$\begin{aligned}
\rho^{n+1}_{i,j,k}u^{n+1}_{y_{i,j,k}} &= \rho^{n}_{i,j,k}u^{n}_{y_{i,j,k}} - \Delta t\Bigg\{ \frac{1}{2\Delta x}\Big[\rho^{n}_{i+1,j,k}u^{n}_{x_{i+1,j,k}}u^{n}_{y_{i+1,j,k}} - \rho^{n}_{i-1,j,k}u^{n}_{x_{i-1,j,k}}u^{n}_{y_{i-1,j,k}} \\
&- B^{n}_{x_{i+1,j,k}}B^{n}_{y_{i+1,j,k}} + B^{n}_{x_{i-1,j,k}}B^{n}_{y_{i-1,j,k}}\Big] \\
&+ \frac{1}{2\Delta y}\Big[\rho^{n}_{i,j+1,k}u^{n}_{y_{i,j+1,k}}u^{n}_{y_{i,j+1,k}} - \rho^{n}_{i,j-1,k}u^{n}_{y_{i,j-1,k}}u^{n}_{y_{i,j-1,k}} \\
&+ \frac{1}{2}\Big(p^{n}_{i,j+1,k} + B^{2^n}_{i,j+1,k}\Big) - \frac{1}{2}\Big(p^{n}_{i,j-1,k} + B^{2^n}_{i,j-1,k}\Big) \\
&- B^{n}_{y_{i,j+1,k}}B^{n}_{yi,j+1,k} + B^{n}_{y_{i,j-1,k}}B^{n}_{y_{i,j-1,k}}\Big] \\
&+ \frac{1}{2\Delta z}\Big[\rho^{n}_{i,j,k+1}u_{z_{i,j,k+1}}u^{n}_{y_{i,j,k+1}} - \rho^{n}_{i,j,k-1}u^{n}_{z_{i,j,k-1}}u^{n}_{y_{i,j,k-1}} \\
&- B^{n}_{z_{i,j,k+1}}B^{n}_{y_{i,j,k+1}} + B^{n}_{z_{i,j,k-1}}B^{n}_{y_{i,j,k-1}}\Big] \\
&+ \mu\rho^{n}_{i,j,k}\Big(u^{n}_{y_{i,j,k}} - u^{n}_{yN_{i,j,k}}\Big)\Bigg\} \qquad \text{(B.3)}
\end{aligned}$$

Z-Component of the momentum equation

$$\begin{aligned}
\rho^{n+1}_{i,j,k}u^{n+1}_{z_{i,j,k}} &= \rho^{n}_{i,j,k}u^{n}_{z_{i,j,k}} - \Delta t\Bigg\{ \frac{1}{2\Delta x}\Big[\rho^{n}_{i+1,j,k}u^{n}_{x_{i+1,j,k}}u^{n}_{z_{i+1,j,k}} - \rho^{n}_{i-1,j,k}u^{n}_{x_{i-1,j,k}}u^{n}_{z_{i-1,j,k}} \\
&- B^{n}_{x_{i+1,j,k}}B^{n}_{z_{i+1,j,k}} + B^{n}_{x_{i-1,j,k}}B^{n}_{z_{i-1,j,k}}\Big] \\
&+ \frac{1}{2\Delta y}\Big[\rho^{n}_{i,j+1,k}u^{n}_{y_{i,j+1,k}}u^{n}_{z_{i,j+1,k}} - \rho^{n}_{i,j-1,k}u^{n}_{y_{i,j-1,k}}u^{n}_{z_{i,j-1,k}} \\
&- B^{n}_{y_{i,j+1,k}}B^{n}_{zi,j+1,k} + B^{n}_{y_{i,j-1,k}}B^{n}_{z_{i,j-1,k}}\Big] \\
&+ \frac{1}{2\Delta z}\Big[\rho^{n}_{i,j,k+1}u_{z_{i,j,k+1}}u^{n}_{z_{i,j,k+1}} - \rho^{n}_{i,j,k-1}u^{n}_{z_{i,j,k-1}}u^{n}_{z_{i,j,k-1}} \\
&+ \frac{1}{2}\Big(p^{n}_{i,j,k+1} + B^{2^n}_{i,j,k+1}\Big) - \frac{1}{2}\Big(p^{n}_{i,j,k-1} + B^{2^n}_{i,j,k-1}\Big) \\
&- B^{n}_{z_{i,j,k+1}}B^{n}_{z_{i,j,k+1}} + B^{n}_{z_{i,j,k-1}}B^{n}_{z_{i,j,k-1}}\Big] \\
&+ \mu\rho^{n}_{i,j,k}\Big(u^{n}_{z_{i,j,k}} - u^{n}_{zN_{i,j,k}}\Big)\Bigg\} \qquad \text{(B.4)}
\end{aligned}$$

Energy equation

$$
\begin{aligned}
h^{n+1}_{i,j,k} &= h^n_{i,j,k} - \Delta t \Bigg\{ \\
&\quad \frac{1}{2\Delta x}\Big[h^n_{i+1,j,k} u^n_{x_{i+1,j,k}} - h^n_{i-1,j,k} u^n_{x_{i-1,j,k}}\Big] \\
&+ \frac{1}{2\Delta y}\Big[h^n_{i,j+1,k} u^n_{y_{i,j+1,k}} - h^n_{i,j-1,k} u^n_{y_{i,j-1,k}}\Big] \\
&+ \frac{1}{2\Delta z}\Big[h^n_{i,j,k+1} u^n_{z_{i,j,k+1}} - h^n_{i,j,k-1} u^n_{z_{i,j,k-1}}\Big] \\
&- \frac{(\gamma-1)}{\gamma}(h^n_{i,j,k})^{1-\gamma}\eta^n_{i,j,k}(j^n_{i,j,k})^2 \Bigg\}
\end{aligned}
\tag{B.5}
$$

X-component of the induction equation

$$
\begin{aligned}
B^{n+1}_{x_{i,j,k}} &= B^n_{x_{i,j,k}} + \Delta t \Bigg\{ \\
&\quad \frac{1}{2\Delta y}\Big(u^n_{x_{i,j+1,k}} B^n_{y_{i,j+1,k}} - u^n_{y_{i,j+1,k}} B^n_{x_{i,j+1,k}} \\
&- \eta^n_{i,j+1,k} j^n_{z_{i,j+1,k}} - u^n_{x_{i,j-1,k}} B^n_{y_{i,j-1,k}} \\
&+ u^n_{y_{i,j-1,k}} B^n_{x_{i,j-1,k}} + \eta^n_{i,j-1,k} j^n_{z_{i,j-1,k}} \Big) \\
&- \frac{1}{2\Delta z}\Big(u^n_{z_{i,j,k+1}} B^n_{x_{i,j,k+1}} - u^n_{x_{i,j,k+1}} B^n_{z_{i,j,k+1}} \\
&- \eta^n_{i,j,k+1} j^n_{y_{i,j,k+1}} - u^n_{z_{i,j,k-1}} B^n_{x_{i,j,k-1}} \\
&+ u^n_{x_{i,j,k-1}} B^n_{z_{i,j,k-1}} + \eta^n_{i,j,k-1} j^n_{y_{i,j,k-1}} \Big) \Bigg\}
\end{aligned}
\tag{B.6}
$$

Y-component of the induction equation

$$
\begin{aligned}
B^{n+1}_{y_{i,j,k}} &= B^{n}_{y_{i,j,k}} + \Delta t \Bigg\{ \\
&\quad \frac{1}{2\Delta z}\Big(u^{n}_{y_{i,j,k+1}} B^{n}_{z_{i,j,k+1}} - u^{n}_{z_{i,j,k+1}} B^{n}_{y_{i,j,k+1}} \\
&- \eta^{n}_{i,j,k+1} j^{n}_{x_{i,j,k+1}} - u^{n}_{y_{i,j,k-1}} B^{n}_{z_{i,j,k-1}} \\
&+ u^{n}_{z_{i,j,k-1}} B^{n}_{y_{i,j,k-1}} + \eta^{n}_{i,j,k-1} j^{n}_{x_{i,j,k-1}} \Big) \\
&- \frac{1}{2\Delta x}\Big(u^{n}_{x_{i+1,j,k}} B^{n}_{y_{i+1,j,k}} - u^{n}_{y_{i+1,j,k}} B^{n}_{x_{i+1,j,k}} \\
&- \eta^{n}_{i+1,j,k} j^{n}_{z_{i+1,j,k}} - u^{n}_{x_{i-1,j,k}} B^{n}_{y_{i-1,j,k}} \\
&+ u^{n}_{y_{i-1,j,k}} B^{n}_{x_{i-1,j,k}} + \eta^{n}_{i-1,j,k} j^{n}_{z_{i-1,j,k}} \Big) \Bigg\}
\end{aligned}
\tag{B.7}
$$

Z-component of the induction equation

$$
\begin{aligned}
B^{n+1}_{z_{i,j,k}} &= B^{n}_{z_{i,j,k}} + \Delta t \Bigg\{ \\
&\quad \frac{1}{2\Delta x}\Big(u^{n}_{z_{i+1,j,k}} B^{n}_{x_{i+1,j,k}} - u^{n}_{x_{i+1,j,k}} B^{n}_{z_{i+1,j,k}} \\
&- \eta^{n}_{i+1,j,k} j^{n}_{y_{i+1,j,k}} - u^{n}_{z_{i-1,j,k}} B^{n}_{x_{i-1,j,k}} \\
&+ u^{n}_{x_{i-1,j,k}} B^{n}_{z_{i-1,j,k}} + \eta^{n}_{i-1,j,k} j^{n}_{y_{i-1,j,k}} \Big) \\
&- \frac{1}{2\Delta y}\Big(u^{n}_{y_{i,j+1,k}} B^{n}_{z_{i,j+1,k}} - u^{n}_{z_{i,j+1,k}} B^{n}_{y_{i,j+1,k}} \\
&- \eta^{n}_{i,j+1,k} j^{n}_{x_{i,j+1,k}} - u^{n}_{y_{i,j-1,k}} B^{n}_{z_{i,j-1,k}} \\
&+ u^{n}_{z_{i,j-1,k}} B^{n}_{y_{i,j-1,k}} + \eta^{n}_{i,j-1,k} j^{n}_{x_{i,j-1,k}} \Big) \Bigg\}
\end{aligned}
\tag{B.8}
$$

C APPENDIX C - DISCRETIZATION OF THE MHD EQUATIONS USING LAX SCHEME

Continuity equation

$$\begin{aligned}
\rho^{n+1}_{i,j,k} &= \frac{1}{6}(\rho^n_{i+1,j,k} + \rho^n_{i-1,j,k} + \rho^n_{i,j+1,k} + \rho^n_{i,j-1,k} + \rho^n_{i,j,k+1}\rho^n_{i,j,k-1}) \\
&- \Delta t\Big[\frac{1}{2\Delta x}\Big(\rho^n_{i+1,j,k}u^n_{x_{i+1,j,k}} - \rho^n_{i-1,j,k}u^n_{x_{i-1,j,k}}\Big) \\
&+ \frac{1}{2\Delta y}\Big(\rho^n_{i,j+1,k}u^n_{y_{i,j+1,k}} - \rho^n_{i,j-1,k}u^n_{y_{i,j-1,k}}\Big) \\
&+ \frac{1}{2\Delta z}\Big(\rho_{i,j,k+1}nu^n_{z_{i,j,k+1}} - \rho_{i,j,k-1}nu^n_{z_{i,j,k-1}}\Big)\Big]
\end{aligned} \tag{C.1}$$

X-component of the momentum equation

$$\begin{aligned}
\rho^{n+1}_{i,j,k}u^{n+1}_{x_{i,j,k}} &= \frac{1}{6}(\rho^n_{i+1,j,k}u^n_{x_{i+1,j,k}} + \rho^n_{i-1,j,k}u^n_{x_{i-1,j,k}} + \rho^n_{i,j+1,k}u^n_{x_{i,j+1,k}} \\
&+ \rho^n_{i,j-1,k}u^n_{x_{i,j-1,k}} + \rho^n_{i,j,k+1}u^n_{x_{i,j,k+1}} + \rho^n_{i,j,k-1}u^n_{x_{i,j,k-1}}) \\
&- \Delta t\Bigg\{\frac{1}{2\Delta x}\Big[\rho^n_{i+1,j,k}u^n_{x_{i+1,j,k}}u^n_{x_{i+1,j,k}} - \rho^n_{i-1,j,k}u^n_{x_{i-1,j,k}}u^n_{x_{i-1,j,k}} \\
&+ \frac{1}{2}\Big(p^n_{i+1,j,k} + B^{2^n}_{i+1,j,k}\Big) - \frac{1}{2}\Big(p^n_{i-1,j,k} + B^{2^n}_{i-1,j,k}\Big) \\
&- B^n_{x_{i+1,j,k}}B^n_{x_{i+1,j,k}} + B^n_{x_{i-1,j,k}}B^n_{x_{i-1,j,k}}\Big] \\
&+ \frac{1}{2\Delta y}\Big[\rho^n_{i,j+1,k}u^n_{y_{i,j+1,k}}u^n_{x_{i,j+1,k}} - \rho^n_{i,j-1,k}u^n_{y_{i,j-1,k}}u^n_{x_{i,j-1,k}} \\
&- B^n_{y_{i,j+1,k}}B^n_{x_{i,j+1,k}} + B^n_{y_{i,j-1,k}}B^n_{x_{i,j-1,k}}\Big] \\
&+ \frac{1}{2\Delta z}\Big[\rho^n_{i,j,k+1}u_{z_{i,j,k+1}}u^n_{x_{i,j,k+1}} - \rho^n_{i,j,k-1}u^n_{z_{i,j,k-1}}u^n_{x_{i,j,k-1}} \\
&- B^n_{z_{i,j,k+1}}B^n_{x_{i,j,k+1}} + B^n_{z_{i,j,k-1}}B^n_{x_{i,j,k-1}}\Big] \\
&+ \mu\rho^n_{i,j,k}\Big(u^n_{x_{i,j,k}} - u^n_{xN_{i,j,k}}\Big)\Bigg\}
\end{aligned} \tag{C.2}$$

Y-Component of the momentum equation

$$
\begin{aligned}
\rho^{n+1}_{i,j,k}u^{n+1}_{y_{i,j,k}} &= \frac{1}{6}(\rho^n_{i+1,j,k}u^n_{y_{i+1,j,k}} + \rho^n_{i-1,j,k}u^n_{y_{i-1,j,k}} + \rho^n_{i,j+1,k}u^n_{y_{i,j+1,k}} \\
&+ \rho^n_{i,j-1,k}u^n_{y_{i,j-1,k}} + \rho^n_{i,j,k+1}u^n_{y_{i,j,k+1}} + \rho^n_{i,j,k-1}u^n_{y_{i,j,k-1}}) \\
&- \Delta t\Bigg\{ \frac{1}{2\Delta x}\Big[\rho^n_{i+1,j,k}u^n_{x_{i+1,j,k}}u^n_{y_{i+1,j,k}} - \rho^n_{i-1,j,k}u^n_{x_{i-1,j,k}}u^n_{y_{i-1,j,k}} \\
&- B^n_{x_{i+1,j,k}}B^n_{y_{i+1,j,k}} + B^n_{x_{i-1,j,k}}B^n_{y_{i-1,j,k}}\Big] \\
&+ \frac{1}{2\Delta y}\Big[\rho^n_{i,j+1,k}u^n_{y_{i,j+1,k}}u^n_{y_{i,j+1,k}} - \rho^n_{i,j-1,k}u^n_{y_{i,j-1,k}}u^n_{y_{i,j-1,k}} \\
&+ \frac{1}{2}\Big(p^n_{i,j+1,k} + B^{2^n}_{i,j+1,k}\Big) - \frac{1}{2}\Big(p^n_{i,j-1,k} + B^{2^n}_{i,j-1,k}\Big) \\
&- B^n_{y_{i,j+1,k}}B^n_{yi,j+1,k} + B^n_{y_{i,j-1,k}}B^n_{y_{i,j-1,k}}\Big] \\
&+ \frac{1}{2\Delta z}\Big[\rho^n_{i,j,k+1}u_{z_{i,j,k+1}}u^n_{y_{i,j,k+1}} - \rho^n_{i,j,k-1}u^n_{z_{i,j,k-1}}u^n_{y_{i,j,k-1}} \\
&- B^n_{z_{i,j,k+1}}B^n_{y_{i,j,k+1}} + B^n_{z_{i,j,k-1}}B^n_{y_{i,j,k-1}}\Big] \\
&+ \mu\rho^n_{i,j,k}\Big(u^n_{y_{i,j,k}} - u^n_{yN_{i,j,k}}\Big)\Bigg\}
\end{aligned}
\tag{C.3}
$$

Z-Component of the momentum equation

$$
\begin{aligned}
\rho^{n+1}_{i,j,k}u^{n+1}_{z_{i,j,k}} &= \frac{1}{6}(\rho^n_{i+1,j,k}u^n_{z_{i+1,j,k}} + \rho^n_{i-1,j,k}u^n_{z_{i-1,j,k}} + \rho^n_{i,j+1,k}u^n_{z_{i,j+1,k}} \\
&+ \rho^n_{i,j-1,k}u^n_{z_{i,j-1,k}} + \rho^n_{i,j,k+1}u^n_{z_{i,j,k+1}} + \rho^n_{i,j,k-1}u^n_{z_{i,j,k-1}}) \\
&- \Delta t\Bigg\{ \frac{1}{2\Delta x}\Big[\rho^n_{i+1,j,k}u^n_{x_{i+1,j,k}}u^n_{z_{i+1,j,k}} - \rho^n_{i-1,j,k}u^n_{x_{i-1,j,k}}u^n_{z_{i-1,j,k}} \\
&- B^n_{x_{i+1,j,k}}B^n_{z_{i+1,j,k}} + B^n_{x_{i-1,j,k}}B^n_{z_{i-1,j,k}}\Big] \\
&+ \frac{1}{2\Delta y}\Big[\rho^n_{i,j+1,k}u^n_{y_{i,j+1,k}}u^n_{z_{i,j+1,k}} - \rho^n_{i,j-1,k}u^n_{y_{i,j-1,k}}u^n_{z_{i,j-1,k}} \\
&- B^n_{y_{i,j+1,k}}B^n_{zi,j+1,k} + B^n_{y_{i,j-1,k}}B^n_{z_{i,j-1,k}}\Big] \\
&+ \frac{1}{2\Delta z}\Big[\rho^n_{i,j,k+1}u_{z_{i,j,k+1}}u^n_{z_{i,j,k+1}} - \rho^n_{i,j,k-1}u^n_{z_{i,j,k-1}}u^n_{z_{i,j,k-1}} \\
&+ \frac{1}{2}\Big(p^n_{i,j,k+1} + B^{2^n}_{i,j,k+1}\Big) - \frac{1}{2}\Big(p^n_{i,j,k-1} + B^{2^n}_{i,j,k-1}\Big) \\
&- B^n_{z_{i,j,k+1}}B^n_{z_{i,j,k+1}} + B^n_{z_{i,j,k-1}}B^n_{z_{i,j,k-1}}\Big] \\
&+ \mu\rho^n_{i,j,k}\Big(u^n_{z_{i,j,k}} - u^n_{zN_{i,j,k}}\Big)\Bigg\}
\end{aligned}
\tag{C.4}
$$

Energy equation

$$
\begin{aligned}
h^{n+1}_{i,j,k} &= \frac{1}{6}(h^n_{i+1,j,k} + h^n_{i-1,j,k} + h^n_{i,j+1,k} \\
&+ h^n_{i,j-1,k} + h^n_{i,j,k+1} + h^n_{i,j,k-1}) - \Delta t \Bigg\{ \\
&\frac{1}{2\Delta x}\left[h^n_{i+1,j,k} u^n_{x_{i+1,j,k}} - h^n_{i-1,j,k} u^n_{x_{i-1,j,k}}\right] \\
&+ \frac{1}{2\Delta y}\left[h^n_{i,j+1,k} u^n_{y_{i,j+1,k}} - h^n_{i,j-1,k} u^n_{y_{i,j-1,k}}\right] \\
&+ \frac{1}{2\Delta z}\left[h^n_{i,j,k+1} u^n_{z_{i,j,k+1}} - h^n_{i,j,k-1} u^n_{z_{i,j,k-1}}\right] \\
&- \frac{(\gamma-1)}{\gamma}(h^n_{i,j,k})^{1-\gamma} \eta^n_{i,j,k} (j^n_{i,j,k})^2 \Bigg\}
\end{aligned}
\tag{C.5}
$$

X-component of the induction equation

$$
\begin{aligned}
B^{n+1}_{x_{i,j,k}} &= \frac{1}{6}(B^n_{x_{i+1,j,k}} + B^n_{x_{i-1,j,k}} + B^n_{x_{i,j+1,k}} \\
&+ B^n_{x_{i,j-1,k}} + B^n_{x_{i,j,k+1}} + B^n_{x_{i,j,k-1}}) + \Delta t \Bigg\{ \\
&\frac{1}{2\Delta y}\Big(u^n_{x_{i,j+1,k}} B^n_{y_{i,j+1,k}} - u^n_{y_{i,j+1,k}} B^n_{x_{i,j+1,k}} \\
&- \eta^n_{i,j+1,k} j^n_{z_{i,j+1,k}} - u^n_{x_{i,j-1,k}} B^n_{y_{i,j-1,k}} \\
&+ u^n_{y_{i,j-1,k}} B^n_{x_{i,j-1,k}} + \eta^n_{i,j-1,k} j^n_{z_{i,j-1,k}} \Big) \\
&- \frac{1}{2\Delta z}\Big(u^n_{z_{i,j,k+1}} B^n_{x_{i,j,k+1}} - u^n_{x_{i,j,k+1}} B^n_{z_{i,j,k+1}} \\
&- \eta^n_{i,j,k+1} j^n_{y_{i,j,k+1}} - u^n_{z_{i,j,k-1}} B^n_{x_{i,j,k-1}} \\
&+ u^n_{x_{i,j,k-1}} B^n_{z_{i,j,k-1}} + \eta^n_{i,j,k-1} j^n_{y_{i,j,k-1}} \Big) \Bigg\}
\end{aligned}
\tag{C.6}
$$

Y-component of the induction equation

$$
\begin{aligned}
B^{n+1}_{y_{i,j,k}} &= \frac{1}{6}(B^n_{y_{i+1,j,k}} + B^n_{y_{i-1,j,k}} + B^n_{y_{i,j+1,k}} \\
&+ B^n_{y_{i,j-1,k}} + B^n_{y_{i,j,k+1}} + B^n_{y_{i,j,k-1}}) + \Delta t \Bigg\{ \\
&\frac{1}{2\Delta z}\Big(u^n_{y_{i,j,k+1}} B^n_{z_{i,j,k+1}} - u^n_{z_{i,j,k+1}} B^n_{y_{i,j,k+1}} \\
&- \eta^n_{i,j,k+1} j^n_{x_{i,j,k+1}} - u^n_{y_{i,j,k-1}} B^n_{z_{i,j,k-1}} \\
&+ u^n_{z_{i,j,k-1}} B^n_{y_{i,j,k-1}} + \eta^n_{i,j,k-1} j^n_{x_{i,j,k-1}}\Big) \\
&- \frac{1}{2\Delta x}\Big(u^n_{x_{i+1,j,k}} B^n_{y_{i+1,j,k}} - u^n_{y_{i+1,j,k}} B^n_{x_{i+1,j,k}} \\
&- \eta^n_{i+1,j,k} j^n_{z_{i+1,j,k}} - u^n_{x_{i-1,j,k}} B^n_{y_{i-1,j,k}} \\
&+ u^n_{y_{i-1,j,k}} B^n_{x_{i-1,j,k}} + \eta^n_{i-1,j,k} j^n_{z_{i-1,j,k}}\Big)\Bigg\}
\end{aligned}
\tag{C.7}
$$

Z-component of the induction equation

$$
\begin{aligned}
B^{n+1}_{z_{i,j,k}} &= \frac{1}{6}(B^n_{z_{i+1,j,k}} + B^n_{z_{i-1,j,k}} + B^n_{z_{i,j+1,k}} \\
&+ B^n_{z_{i,j-1,k}} + B^n_{z_{i,j,k+1}} + B^n_{z_{i,j,k-1}}) + \Delta t \Bigg\{ \\
&\frac{1}{2\Delta x}\Big(u^n_{z_{i+1,j,k}} B^n_{x_{i+1,j,k}} - u^n_{x_{i+1,j,k}} B^n_{z_{i+1,j,k}} \\
&- \eta^n_{i+1,j,k} j^n_{y_{i+1,j,k}} - u^n_{z_{i-1,j,k}} B^n_{x_{i-1,j,k}} \\
&+ u^n_{x_{i-1,j,k}} B^n_{z_{i-1,j,k}} + \eta^n_{i-1,j,k} j^n_{y_{i-1,j,k}}\Big) \\
&- \frac{1}{2\Delta y}\Big(u^n_{y_{i,j+1,k}} B^n_{z_{i,j+1,k}} - u^n_{z_{i,j+1,k}} B^n_{y_{i,j+1,k}} \\
&- \eta^n_{i,j+1,k} j^n_{x_{i,j+1,k}} - u^n_{y_{i,j-1,k}} B^n_{z_{i,j-1,k}} \\
&+ u^n_{z_{i,j-1,k}} B^n_{y_{i,j-1,k}} + \eta^n_{i,j-1,k} j^n_{x_{i,j-1,k}}\Big)\Bigg\}
\end{aligned}
\tag{C.8}
$$

D APPENDIX D - DISCRETIZATION OF THE MHD EQUATIONS USING LEAPFROG SCHEME

Continuity equation

$$\begin{aligned}\rho_{i,j,k}^{n+1} &= \rho_{i,j,k}^{n-1} - \Delta t\Big[\frac{1}{\Delta x}\Big(\rho_{i+1,j,k}^{n} u_{x_{i+1,j,k}}^{n} - \rho_{i-1,j,k}^{n} u_{x_{i-1,j,k}}^{n}\Big) \\ &+ \frac{1}{\Delta y}\Big(\rho_{i,j+1,k}^{n} u_{y_{i,j+1,k}}^{n} - \rho_{i,j-1,k}^{n} u_{y_{i,j-1,k}}^{n}\Big) \\ &+ \frac{1}{\Delta z}\Big(\rho_{i,j,k+1} n u_{z_{i,j,k+1}}^{n} - \rho_{i,j,k-1} n u_{z_{i,j,k-1}}^{n}\Big)\Big] \end{aligned} \tag{D.1}$$

X-component of the momentum equation

$$\begin{aligned}\rho_{i,j,k}^{n+1} u_{x_{i,j,k}}^{n+1} &= \rho_{i,j,k}^{n-1} u_{x_{i,j,k}}^{n-1} - \Delta t\Bigg\{ \\ &\frac{1}{\Delta x}\Big[\rho_{i+1,j,k}^{n} u_{x_{i+1,j,k}}^{n} u_{x_{i+1,j,k}}^{n} - \rho_{i-1,j,k}^{n} u_{x_{i-1,j,k}}^{n} u_{x_{i-1,j,k}}^{n} \\ &+ \frac{1}{2}\Big(p_{i+1,j,k}^{n} + B_{i+1,j,k}^{2^n}\Big) - \frac{1}{2}\Big(p_{i-1,j,k}^{n} + B_{i-1,j,k}^{2^n}\Big) \\ &- B_{x_{i+1,j,k}}^{n} B_{x_{i+1,j,k}}^{n} + B_{x_{i-1,j,k}}^{n} B_{x_{i-1,j,k}}^{n}\Big] \\ &+ \frac{1}{\Delta y}\Big[\rho_{i,j+1,k}^{n} u_{y_{i,j+1,k}}^{n} u_{x_{i,j+1,k}}^{n} - \rho_{i,j-1,k}^{n} u_{y_{i,j-1,k}}^{n} u_{x_{i,j-1,k}}^{n} \\ &+ \frac{1}{2}\Big(p_{i,j+1,k}^{n} + B_{i,j+1,k}^{2^n}\Big) - \frac{1}{2}\Big(p_{i,j-1,k}^{n} + B_{i,j-1,k}^{2^n}\Big) \\ &- B_{y_{i,j+1,k}}^{n} B_{x_{i,j+1,k}}^{n} + B_{y_{i,j-1,k}}^{n} B_{x_{i,j-1,k}}^{n}\Big] \\ &+ \frac{1}{\Delta z}\Big[\rho_{i,j,k+1}^{n} u_{z_{i,j,k+1}} u_{x_{i,j,k+1}}^{n} - \rho_{i,j,k-1}^{n} u_{z_{i,j,k-1}}^{n} u_{x_{i,j,k-1}}^{n} \\ &+ \frac{1}{2}\Big(p_{i,j,k+1}^{n} + B_{i,j,k+1}^{2^n}\Big) - \frac{1}{2}\Big(p_{i,j,k-1}^{n} + B_{i,j,k-1}^{2^n}\Big) \\ &- B_{z_{i,j,k+1}}^{n} B_{x_{i,j,k+1}}^{n} + B_{z_{i,j,k-1}}^{n} B_{x_{i,j,k-1}}^{n}\Big] \\ &+ 2\mu\rho_{i,j,k}^{n}\Big(u_{x_{i,j,k}}^{n} - u_{xN_{i,j,k}}^{n}\Big)\Bigg\} \end{aligned} \tag{D.2}$$

Y-Component of the momentum equation

$$
\begin{aligned}
\rho^{n+1}_{i,j,k} u^{n+1}_{y_{i,j,k}} &= \rho^{n-1}_{i,j,k} u^{n-1}_{y_{i,j,k}} - \Delta t \Bigg\{ \\
& \frac{1}{\Delta x}\Big[\rho^{n}_{i+1,j,k} u^{n}_{x_{i+1,j,k}} u^{n}_{y_{i+1,j,k}} - \rho^{n}_{i-1,j,k} u^{n}_{x_{i-1,j,k}} u^{n}_{y_{i-1,j,k}} \\
+ & \frac{1}{2}\Big(p^{n}_{i+1,j,k} + B^{2^n}_{i+1,j,k}\Big) - \frac{1}{2}\Big(p^{n}_{i-1,j,k} + B^{2^n}_{i-1,j,k}\Big) \\
- & B^{n}_{x_{i+1,j,k}} B^{n}_{y_{i+1,j,k}} + B^{n}_{x_{i-1,j,k}} B^{n}_{y_{i-1,j,k}}\Big] \\
+ & \frac{1}{\Delta y}\Big[\rho^{n}_{i,j+1,k} u^{n}_{y_{i,j+1,k}} u^{n}_{y_{i,j+1,k}} - \rho^{n}_{i,j-1,k} u^{n}_{y_{i,j-1,k}} u^{n}_{y_{i,j-1,k}} \\
+ & \frac{1}{2}\Big(p^{n}_{i,j+1,k} + B^{2^n}_{i,j+1,k}\Big) - \frac{1}{2}\Big(p^{n}_{i,j-1,k} + B^{2^n}_{i,j-1,k}\Big) \\
- & B^{n}_{y_{i,j+1,k}} B^{n}_{yi,j+1,k} + B^{n}_{y_{i,j-1,k}} B^{n}_{y_{i,j-1,k}}\Big] \\
+ & \frac{1}{\Delta z}\Big[\rho^{n}_{i,j,k+1} u_{z_{i,j,k+1}} u^{n}_{y_{i,j,k+1}} - \rho^{n}_{i,j,k-1} u^{n}_{z_{i,j,k-1}} u^{n}_{y_{i,j,k-1}} \\
+ & \frac{1}{2}\Big(p^{n}_{i,j,k+1} + B^{2^n}_{i,j,k+1}\Big) - \frac{1}{2}\Big(p^{n}_{i,j,k-1} + B^{2^n}_{i,j,k-1}\Big) \\
- & B^{n}_{z_{i,j,k+1}} B^{n}_{y_{i,j,k+1}} + B^{n}_{z_{i,j,k-1}} B^{n}_{y_{i,j,k-1}}\Big] \\
+ & 2\mu\rho^{n}_{i,j,k}\Big(u^{n}_{y_{i,j,k}} - u^{n}_{yN_{i,j,k}}\Big)\Bigg\}
\end{aligned}
\tag{D.3}
$$

Z-Component of the momentum equation

$$
\begin{aligned}
\rho^{n+1}_{i,j,k}u^{n+1}_{z_{i,j,k}} &= \rho^{n-1}_{i,j,k}u^{n-1}_{z_{i,j,k}} - \Delta t\Bigg\{ \\
&\quad \frac{1}{\Delta x}\Big[\rho^{n}_{i+1,j,k}u^{n}_{x_{i+1,j,k}}u^{n}_{z_{i+1,j,k}} - \rho^{n}_{i-1,j,k}u^{n}_{x_{i-1,j,k}}u^{n}_{z_{i-1,j,k}} \\
&+ \frac{1}{2}\Big(p^{n}_{i+1,j,k} + B^{2^n}_{i+1,j,k}\Big) - \frac{1}{2}\Big(p^{n}_{i-1,j,k} + B^{2^n}_{i-1,j,k}\Big) \\
&- B^{n}_{x_{i+1,j,k}}B^{n}_{z_{i+1,j,k}} + B^{n}_{x_{i-1,j,k}}B^{n}_{z_{i-1,j,k}}\Big] \\
&+ \frac{1}{\Delta y}\Big[\rho^{n}_{i,j+1,k}u^{n}_{y_{i,j+1,k}}u^{n}_{z_{i,j+1,k}} - \rho^{n}_{i,j-1,k}u^{n}_{y_{i,j-1,k}}u^{n}_{z_{i,j-1,k}} \\
&+ \frac{1}{2}\Big(p^{n}_{i,j+1,k} + B^{2^n}_{i,j+1,k}\Big) - \frac{1}{2}\Big(p^{n}_{i,j-1,k} + B^{2^n}_{i,j-1,k}\Big) \\
&- B^{n}_{y_{i,j+1,k}}B^{n}_{zi,j+1,k} + B^{n}_{y_{i,j-1,k}}B^{n}_{z_{i,j-1,k}}\Big] \\
&+ \frac{1}{\Delta z}\Big[\rho^{n}_{i,j,k+1}u_{z_{i,j,k+1}}u^{n}_{z_{i,j,k+1}} - \rho^{n}_{i,j,k-1}u^{n}_{z_{i,j,k-1}}u^{n}_{z_{i,j,k-1}} \\
&+ \frac{1}{2}\Big(p^{n}_{i,j,k+1} + B^{2^n}_{i,j,k+1}\Big) - \frac{1}{2}\Big(p^{n}_{i,j,k-1} + B^{2^n}_{i,j,k-1}\Big) \\
&- B^{n}_{z_{i,j,k+1}}B^{n}_{z_{i,j,k+1}} + B^{n}_{z_{i,j,k-1}}B^{n}_{z_{i,j,k-1}}\Big] \\
&+ 2\mu\rho^{n}_{i,j,k}\Big(u^{n}_{z_{i,j,k}} - u^{n}_{zN_{i,j,k}}\Big)\Bigg\}
\end{aligned}
\tag{D.4}
$$

Energy equation

$$
\begin{aligned}
h^{n+1}_{i,j,k} &= h^{n-1}_{i,j,k} - \Delta t\Bigg\{ \\
&\quad \frac{1}{\Delta x}\Big[h^{n}_{i+1,j,k}u^{n}_{x_{i+1,j,k}} - h^{n}_{i-1,j,k}u^{n}_{x_{i-1,j,k}}\Big] \\
&+ \frac{1}{\Delta y}\Big[h^{n}_{i,j+1,k}u^{n}_{y_{i,j+1,k}} - h^{n}_{i,j-1,k}u^{n}_{y_{i,j-1,k}}\Big] \\
&+ \frac{1}{\Delta z}\Big[h^{n}_{i,j,k+1}u^{n}_{z_{i,j,k+1}} - h^{n}_{i,j,k-1}u^{n}_{z_{i,j,k-1}}\Big] \\
&- 2\frac{(\gamma-1)}{\gamma}(h^{n}_{i,j,k})^{1-\gamma}\eta^{n}_{i,j,k}(j^{n}_{i,j,k})^2\Bigg\}
\end{aligned}
\tag{D.5}
$$

X-component of the induction equation

$$
\begin{aligned}
B^{n+1}_{x_{i,j,k}} &= B^{n-1}_{x_{i,j,k}} + \Delta t \Bigg\{ \\
&\quad \frac{1}{\Delta y}\Big(u^n_{x_{i,j+1,k}} B^n_{y_{i,j+1,k}} - u^n_{y_{i,j+1,k}} B^n_{x_{i,j+1,k}} \\
&- \eta^n_{i,j+1,k} j^n_{z_{i,j+1,k}} - u^n_{x_{i,j-1,k}} B^n_{y_{i,j-1,k}} \\
&+ u^n_{y_{i,j-1,k}} B^n_{x_{i,j-1,k}} + \eta^n_{i,j-1,k} j^n_{z_{i,j-1,k}} \Big) \\
&- \frac{1}{\Delta z}\Big(u^n_{z_{i,j,k+1}} B^n_{x_{i,j,k+1}} - u^n_{x_{i,j,k+1}} B^n_{z_{i,j,k+1}} \\
&- \eta^n_{i,j,k+1} j^n_{y_{i,j,k+1}} - u^n_{z_{i,j,k-1}} B^n_{x_{i,j,k-1}} \\
&+ u^n_{x_{i,j,k-1}} B^n_{z_{i,j,k-1}} + \eta^n_{i,j,k-1} j^n_{y_{i,j,k-1}} \Big) \Bigg\}
\end{aligned}
\tag{D.6}
$$

Y-component of the induction equation

$$
\begin{aligned}
B^{n+1}_{y_{i,j,k}} &= B^{n-1}_{y_{i,j,k}} + \Delta t \Bigg\{ \\
&\quad \frac{1}{\Delta z}\Big(u^n_{y_{i,j,k+1}} B^n_{z_{i,j,k+1}} - u^n_{z_{i,j,k+1}} B^n_{y_{i,j,k+1}} \\
&- \eta^n_{i,j,k+1} j^n_{x_{i,j,k+1}} - u^n_{y_{i,j,k-1}} B^n_{z_{i,j,k-1}} \\
&+ u^n_{z_{i,j,k-1}} B^n_{y_{i,j,k-1}} + \eta^n_{i,j,k-1} j^n_{x_{i,j,k-1}} \Big) \\
&- \frac{1}{\Delta x}\Big(u^n_{x_{i+1,j,k}} B^n_{y_{i+1,j,k}} - u^n_{y_{i+1,j,k}} B^n_{x_{i+1,j,k}} \\
&- \eta^n_{i+1,j,k} j^n_{z_{i+1,j,k}} - u^n_{x_{i-1,j,k}} B^n_{y_{i-1,j,k}} \\
&+ u^n_{y_{i-1,j,k}} B^n_{x_{i-1,j,k}} + \eta^n_{i-1,j,k} j^n_{z_{i-1,j,k}} \Big) \Bigg\}
\end{aligned}
\tag{D.7}
$$

Z-component of the induction equation

$$
\begin{aligned}
B^{n+1}_{z_{i,j,k}} &= B^{n-1}_{z_{i,j,k}} + \Delta t \Bigg\{ \\
&\quad \frac{1}{\Delta x}\Big(u^n_{z_{i+1,j,k}} B^n_{x_{i+1,j,k}} - u^n_{x_{i+1,j,k}} B^n_{z_{i+1,j,k}} \\
&- \eta^n_{i+1,j,k} j^n_{y_{i+1,j,k}} - u^n_{z_{i-1,j,k}} B^n_{x_{i-1,j,k}} \\
&+ u^n_{x_{i-1,j,k}} B^n_{z_{i-1,j,k}} + \eta^n_{i-1,j,k} j^n_{y_{i-1,j,k}} \Big) \\
&- \frac{1}{\Delta y}\Big(u^n_{y_{i,j+1,k}} B^n_{z_{i,j+1,k}} - u^n_{z_{i,j+1,k}} B^n_{y_{i,j+1,k}} \\
&- \eta^n_{i,j+1,k} j^n_{x_{i,j+1,k}} - u^n_{y_{i,j-1,k}} B^n_{z_{i,j-1,k}} \\
&+ u^n_{z_{i,j-1,k}} B^n_{y_{i,j-1,k}} + \eta^n_{i,j-1,k} j^n_{x_{i,j-1,k}} \Big) \Bigg\}
\end{aligned}
\tag{D.8}
$$

E APPENDIX E - PARTICULAR ASPECTS OF THE MODEL

E.1 Divergence of $\vec{B}$ cleaning

The Ampère-Maxwell law ensures that if $\vec{\nabla} \cdot \vec{B}$ is zero at the beginning of the simulation it will continue to be zero

$$\begin{aligned} -\frac{\partial \vec{B}}{\partial t} &= \vec{\nabla} \times \vec{E} \\ -\frac{\partial \vec{\nabla} \cdot \vec{B}}{\partial t} &= \vec{\nabla} \cdot (\vec{\nabla} \times \vec{E}) \\ \frac{\partial \vec{\nabla} \cdot \vec{B}}{\partial t} &= 0. \end{aligned} \tag{E.1}$$

However, this initial condition may not be fulfilled or the difference form of the equations may not guarantee the invariance of the divergence of $\vec{B}$ with time, allowing its values to increase.

The problem of the divergence of $\vec{B}$ being different from zero appears in numerical simulations because of the fact the all the quantities are evaluated in a discrete space and not in a continuous space anymore. When space derivatives are calculate the problem is even worst, since the neighboring points on the grid are used and if the space resolution is not enough steep variations can appear in the variables. This problem is present even when the magnetic field is not so strong (quiet sun), but becomes more serious when the simulations deal with strong and complex magnetic field regions (active regions). In MHD simulations the violation of the divergence constraint causes severe instability and should be avoided.

To ensure that the initial values of the divergence of $\vec{B}$ are as close to zero as possible, a 'cleaning' procedure is applied at the beginning of the simulation. The method used for 'cleaning' the divergence of $\vec{B}$ is called projection method. This method consists in calculating a new magnetic field ($\vec{B'}$), which is subtracted from the initial magnetic field ($\vec{B}$) to produce values of the divergence of $\vec{B}$ closer to zero. The magnetic field $\vec{B'}$ is calculated from a scalar function ϕ obtained solving the Poisson equation

$$\nabla^2 \phi = \vec{\nabla} \cdot \vec{B} \tag{E.2}$$

After ϕ is computed it can be used to calculate the new magnetic field, which is subtracted

from the original magnetic field to produce $\vec{\nabla} \cdot \vec{B}$ values closer to zero

$$\begin{aligned} \vec{\nabla} \cdot (\vec{B} - \vec{B}') &= \vec{\nabla} \cdot (\vec{B} - \vec{\nabla}\phi) \\ &= \vec{\nabla} \cdot \vec{B} - \vec{\nabla} \cdot \vec{\nabla}\phi \\ &= \vec{\nabla} \cdot \vec{B} - \nabla^2\phi \\ &= \vec{\nabla} \cdot \vec{B} - \vec{\nabla} \cdot \vec{B} = 0 \end{aligned} \tag{E.3}$$

Therefore, the equation that has to be solved to correct the divergence of $\vec{B}$ problem is

$$\frac{\partial^2\phi}{\partial x^2} + \frac{\partial^2\phi}{\partial y^2} + \frac{\partial^2\phi}{\partial z^2} = \vec{\nabla} \cdot B \tag{E.4}$$

However, the method adopted to obtain ϕ will not solve directly the Poisson equation, but an equation of the form

$$\frac{\partial\phi}{\partial t} = \nabla^2\phi - r, \tag{E.5}$$

where r is the divergence of $\vec{B}$. Before to obtain the difference form for this equation some points have still to be discussed.

The finite difference form of $\nabla^2\phi$ and $\vec{\nabla} \cdot \vec{B}$ are not equivalent. To solve this problem it is necessary the use of a staggered mesh for ϕ and $\vec{B}$. In one dimension the grid is constructed using $x_i = x_1 + \sum_i (i-1)\Delta x$, where $i = 1...nx$. The scalar function in the point x_i is given by $\phi_i = \phi(x_i)$. The laplacian operator is described as a second derivative and its finite difference form is given by

$$\begin{aligned} \left(\frac{\partial^2\phi}{\partial x^2}\right)_i &= \frac{\phi_{i+1} - 2\phi_i + \phi_{i-1}}{\Delta x^2} \\ &= \frac{\left(\frac{\phi_{i+1}-\phi_i}{\Delta x}\right) - \left(\frac{\phi_i - \phi_{i-1}}{\Delta x}\right)}{\Delta x} \end{aligned} \tag{E.6}$$

The numerator represents the gradient of ϕ in the points $i + \frac{1}{2}$ and $i - \frac{1}{2}$, and they are related to the magnetic field by

$$B_{i+\frac{1}{2}} = \frac{\phi_{i+1} - \phi_i}{\Delta x} \tag{E.7}$$

$$B_{i-\frac{1}{2}} = \frac{\phi_i - \phi_{i-1}}{\Delta x}. \tag{E.8}$$

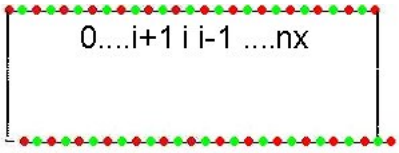

FIGURE E.1 - One dimensional staggered mesh used to calculate the scalar function ϕ applied in the computation of the new magnetic field in the divergence cleanning procedure. The red dots represent the mesh grids where the magnetic field values are known and the green dots are the points where the function ϕ is evaluated.

The laplacian of ϕ can then be rewritten as

$$\left(\frac{\partial^2 \phi}{\partial x^2}\right)_i = \frac{B_{i+\frac{1}{2}} - B_{i-\frac{1}{2}}}{\Delta x}, \tag{E.9}$$

with the right hand side representing the source term in the Poisson equation given by

$$r_i = \frac{B_{i+\frac{1}{2}} - B_{i-\frac{1}{2}}}{\Delta x}. \tag{E.10}$$

The total number of grid points is given by nx, where nx is an odd number. The magnetic field values are given at the grid points, with no intermediary grid values. In this way, to calculate ϕ in the odd points of the grid we need to use the magnetic field in the even points. The values of ϕ in the even points of the grid are computed using the values of $\vec{B}$ in the odd grid points. In this way there are two new grids, one for the even and other for the odd points, with a total number of points given by $n_{xm} = \frac{nx+1}{2}$. With the values obtained for ϕ a correction to the magnetic field is computed. This procedure requires that equation E.5 is solved twice, one for the odd points and the other for the even points.

Figure E.1 presents a sketch showing how the method works in one dimension. In the upper panel the magnetic field values in the odd points are used to calculate the values of ϕ in the even points. In the bottom panel the grid is shifted one point to the right and the values of the magnetic field in the even points are used to calculate ϕ in the odd points. When the grid is shifted is necessary to extend it using the boundary conditions applied in the model.

In two dimensions the same procedure is used. Figure E.2 shows the 4 combinations used to obtain ϕ in the two dimensional grid, using the values of $\vec{B}$ on the grid. Figure E.2a shows the case where no displacement is applied to the grid. The values of $\vec{B}$ in the odd points of the grid are used to calculate ϕ in the even points. In Figure E.2b the grid was

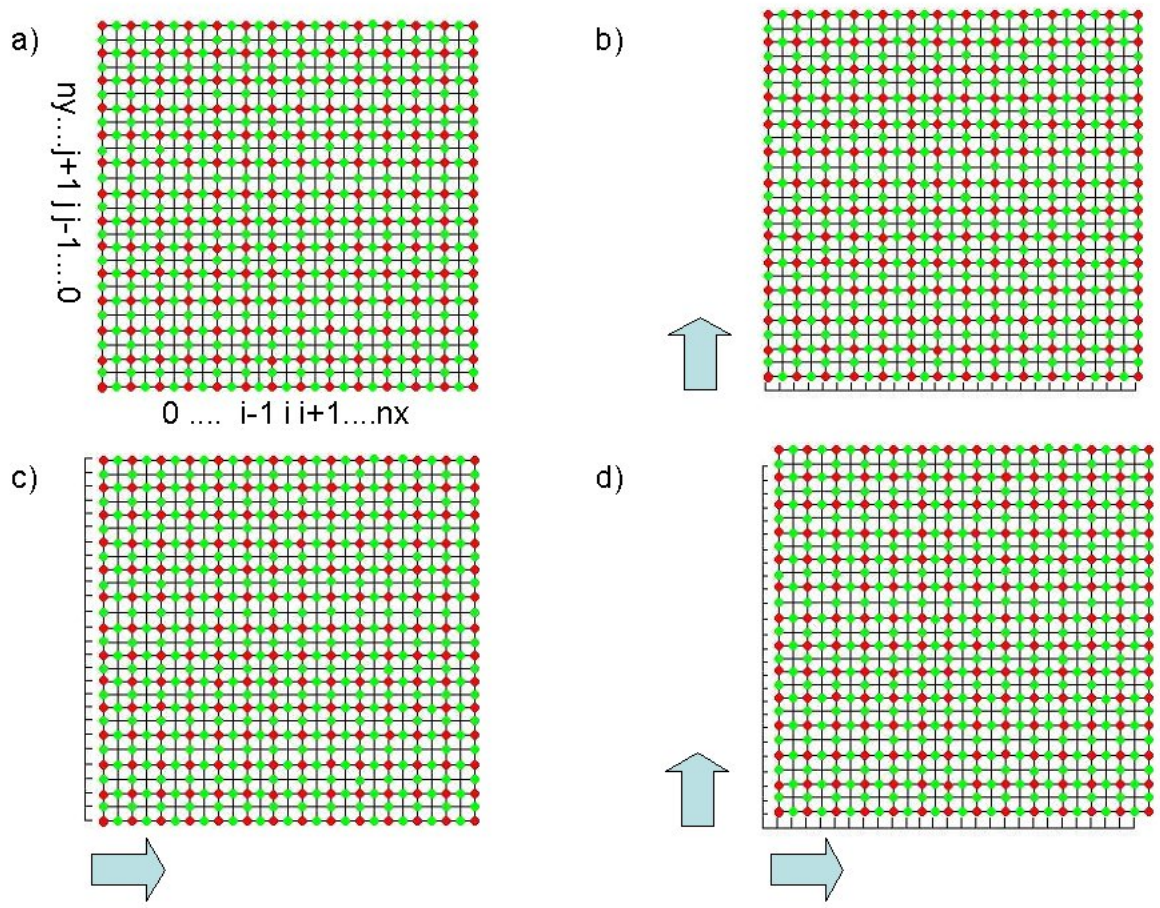

FIGURE E.2 - Two dimensional staggered mesh used to calculate the scalar function ϕ applied in the computation of the new magnetic field in the divergence cleanning procedure. The red dots represent the mesh grids where the magnetic field values are known and the green dots are the points where the function ϕ is evaluated.

displaced one point in the direction of the positive X axis. In this case the values of $\vec{B}$ in the even grid points in the X direction and in the odd grid points in the Y direction are used to calculate ϕ in the odd points of the grid in the X direction and in the even points of the grid in the Y direction. Figure E.2c shows the case when the grid was displaced one point in the direction of the positive Y axis. The values of $\vec{B}$ in the odd grid points in the X direction and in the even grid points in the Y direction are used to calculate ϕ in the even points of the grid in the X direction and in the odd points of the grid in the Y direction. Finally, in Figure E.2d the grid was displaced one point in the direction of the positive X axis and one point in the direction of the positive Y axis. The values of $\vec{B}$ in the even grid points in both directions are used to calculate ϕ in the odd points in both directions.

The three dimensional case will not be presented here, but it is equal to the case in one

and two dimensions. To obtain the values of ϕ in all the points of the grid it is necessary to solve equation E.5 eight times.

The next step is to find the difference form of E.5. Since the MHD model allows the use of a non-equidistant grid, this task is not so simple. It is necessary to rewrite the derivatives in a way that they are performed in an equidistant grid. For simplicity, this task will be executed here for the one-dimensional case. The extension to the three-dimensional case is direct.

Let $z = f(k)$ be the function that maps the physical coordinates in the non-equidistant grid to the k index. The first derivative of a function $\phi(z)$ in relation to z can be rewritten as a derivative in relation to k, around k_0, as follows

$$\begin{aligned} \frac{d\phi}{dz} &= \left(\frac{df}{dk}\right)^{-1}_{k_0}\left(\frac{d\phi}{dk}\right)_{k_0} \\ &= \frac{1}{2}\left(\frac{df}{dk}\right)^{-1}_{k_0}(h_{k_0+1} - h_{k_0-1}) \end{aligned} \tag{E.11}$$

Using the same procedure the second derivative can be rewritten, after some algebra, as

$$\begin{aligned} \frac{d^2\phi}{dz^2} &= \frac{d}{dz}\left(\frac{d\phi}{dz}\right) \\ &= \left(\frac{df}{dk}\right)^{-1}_{k_0}\frac{d}{dk}\left(\frac{d\phi}{dz}\right)\Big|_{k_0} \\ &= \left(\frac{df}{dk}\right)^{-1}_{k_0}\left[\left(\frac{d\phi}{dz}\right)_{k_0+\frac{1}{2}} - \left(\frac{d\phi}{dz}\right)_{k_0-\frac{1}{2}}\right] \\ &= \left(\frac{df}{dk}\right)^{-1}_{k_0}\left[\left(\frac{df}{dk}\right)^{-1}_{k_0+\frac{1}{2}}(\phi_{k_0+1} - \phi_{k_0}) - \left(\frac{df}{dk}\right)^{-1}_{k_0-\frac{1}{2}}(\phi_{k_0} - \phi_{k_0-1})\right] \\ &= \left(\frac{df}{dk}\right)^{-1}_{k_0}\left[\left(\frac{df}{dk}\right)^{-1}_{k_0+\frac{1}{2}}\phi_{k_0+1} - \left(\frac{df}{dk}\right)^{-1}_{k_0+\frac{1}{2}}\phi_{k_0} - \left(\frac{df}{dk}\right)^{-1}_{k_0-\frac{1}{2}}\phi_{k_0}\right. \\ &\quad \left. + \left(\frac{df}{dk}\right)^{-1}_{k_0-\frac{1}{2}}\phi_{k_0-1}\right] \\ &= \left(\frac{df}{dk}\right)^{-1}_{k_0}\left[\left(\frac{df}{dk}\right)^{-1}_{k_0+\frac{1}{2}}\phi_{k_0+1} - \left[\left(\frac{df}{dk}\right)^{-1}_{k_0+\frac{1}{2}} + \left(\frac{df}{dk}\right)^{-1}_{k_0-\frac{1}{2}}\right]\phi_{k_0}\right. \\ &\quad \left. + \left(\frac{df}{dk}\right)^{-1}_{k_0-\frac{1}{2}}\phi_{k_0-1}\right] \end{aligned} \tag{E.12}$$

Using the Dufort-Frankel method

$$\phi_{k_0} = \frac{1}{2}(\phi_{k_0}^{t+1} + \phi_{k_0}^{t-1}) \tag{E.13}$$

the equation E.12 can be rewritten as

$$\begin{aligned}
\frac{\partial^2\phi}{\partial z^2} &= \left(\frac{df}{dk}\right)_{k_0}^{-1}\Big[\left(\frac{df}{dk}\right)_{k_0+\frac{1}{2}}^{-1}\phi_{k_0+1} - \Big[\left(\frac{df}{dk}\right)_{k_0+\frac{1}{2}}^{-1} + \\
&\quad + \left(\frac{df}{dk}\right)_{k_0-\frac{1}{2}}^{-1}\Big]\frac{1}{2}(\phi_{k_0}^{t+1} + \phi_{k_0}^{t-1}) + \left(\frac{df}{dk}\right)_{k_0-\frac{1}{2}}^{-1}\phi_{k_0-1}\Big] \\
&= \left(\frac{df}{dk}\right)_{k_0}^{-1}\Big[\left(\frac{df}{dk}\right)_{k_0+\frac{1}{2}}^{-1}\phi_{k_0+1} - \frac{1}{2}\phi_{k_0}^{t+1}\Big[\left(\frac{df}{dk}\right)_{k_0+\frac{1}{2}}^{-1} + \left(\frac{df}{dk}\right)_{k_0-\frac{1}{2}}^{-1}\Big] + \\
&\quad - \frac{1}{2}\phi_{k_0}^{t-1}\Big[\left(\frac{df}{dk}\right)_{k_0+\frac{1}{2}}^{-1} + \left(\frac{df}{dk}\right)_{k_0-\frac{1}{2}}^{-1}\Big] + \left(\frac{df}{dk}\right)_{k_0-\frac{1}{2}}^{-1}\phi_{k_0-1}\Big]
\end{aligned} \tag{E.14}$$

To simplify the algebra it is convenient to use some definitions

$$\begin{aligned}
dd_+ &= \left(\frac{df}{dk}\right)_{k_0}^{-1}\left(\frac{df}{dk}\right)_{k_0+\frac{1}{2}}^{-1} \\
dd &= \frac{1}{2}\left(\frac{df}{dk}\right)_{k_0}^{-1}\Big[\left(\frac{df}{dk}\right)_{k_0+\frac{1}{2}}^{-1} + \left(\frac{df}{dk}\right)_{k_0-\frac{1}{2}}^{-1}\Big] \\
dd_- &= \left(\frac{df}{dk}\right)_{k_0}^{-1}\left(\frac{df}{dk}\right)_{k_0-\frac{1}{2}}^{-1}
\end{aligned}$$

Then, the second derivative can be finally writhen as

$$\frac{\partial^2\phi}{\partial z^2} = dd_+\phi_{k_0+1} - dd\phi_{k_0}^{t+1} - dd\phi_{k_0}^{t-1} + dd_-\phi_{k_0-1} \tag{E.15}$$

Using equation E.15 to write the second derivative and the Leapfrog scheme, the difference

form of equation E.5, after some algebra, can be written as

$$\begin{aligned}
\frac{\phi_{k0}^{t+1}-\phi_{k_0}^{t-1}}{2\Delta t} &= dd_+\phi_{k_0+1} - dd\phi_{k_0}^{t+1} - dd\phi_{k_0}^{t-1} + dd_-\phi_{k_0-1} - r_{k_0} \\
\phi_{k0}^{t+1}-\phi_{k_0}^{t-1} &= 2\Delta t\Big(dd_+\phi_{k_0+1} - dd\phi_{k_0}^{t+1} - dd\phi_{k_0}^{t-1} + dd_-\phi_{k_0-1} - r_{k_0}\Big) \\
(1+2dd\Delta t)\phi_{k_0}^{t+1} &= (1-2dd\Delta t)\phi_{k_0}^{t+1} + 2\Delta t\Big(dd_+\phi_{k_0+1} + dd_-\phi_{k_0-1} - r_{k_0}\Big) \\
\phi_{k_0}^{t+1} &= \frac{(1-2dd\Delta t)}{(1+2dd\Delta t)}\phi_{k_0}^{t-1} + \frac{2\Delta t}{(1+2dd\Delta t)}\Big(dd_+\phi_{k_0+1} + dd_-\phi_{k_0-1} - r_{k_0}\Big) \\
\phi_{k_0}^{t+1} &= \phi_{k_0}^{t-1} + \frac{(1-2dd\Delta t)-(1+2dd\Delta t)}{(1+2dd\Delta t)}\phi_{k_0}^{t-1} + \\
&\quad + \frac{2\Delta t}{(1+2dd\Delta t)}\Big(dd_+\phi_{k_0+1} + dd_-\phi_{k_0-1} - r_{k_0}\Big) \\
\phi_{k_0}^{t+1} &= \phi_{k_0}^{t-1} + \frac{2\Delta t}{(1+2dd\Delta t)}\Big(dd_+\phi_{k_0+1} - 2dd\phi_{k_0}^{t-1} \\
&\quad + dd_-\phi_{k_0-1} - r_{k_0}\Big)
\end{aligned} \tag{E.16}$$

This equation is solved recursively until the value of ϕ does not change anymore.

E.2 Step size in z direction

z	Δz (L_0)	Δz (km)	z	Δz (L_0)	Δz (km)
0	0.300001	150.000	35	0.394803	197.401
1	0.300000	150.000	36	0.396865	198.432
2	0.300001	150.000	37	0.400345	200.172
3	0.300015	150.007	38	0.405627	202.813
4	0.300073	150.037	39	0.413078	206.539
5	0.300228	150.114	40	0.423035	211.517
6	0.300547	150.273	41	0.435790	217.895
7	0.301107	150.554	42	0.451577	225.788
8	0.301995	150.997	43	0.470556	235.278
9	0.303294	151.647	44	0.492808	246.404
10	0.305084	152.542	45	0.518319	259.160
11	0.307432	153.716	46	0.546983	273.492
12	0.310390	155.195	47	0.578591	289.295
13	0.313984	156.992	48	0.612836	306.418
14	0.318217	159.108	49	0.649315	324.658
15	0.323062	161.531	50	0.687538	343.769
16	0.328464	164.232	51	0.726935	363.467
17	0.334338	167.169	52	0.766869	383.435
18	0.340572	170.286	53	0.806656	403.328
19	0.347032	173.516	54	0.845576	422.788
20	0.353567	176.784	55	0.882897	441.449
21	0.360015	180.008	56	0.917892	458.946
22	0.366211	183.106	57	0.949861	474.930
23	0.371998	185.999	58	0.978148	489.074
24	0.377230	188.615	59	1.00216	501.082
25	0.381790	190.895	60	1.02140	510.701
26	0.385589	192.795	61	1.03545	517.723
27	0.388583	194.292	62	1.04400	521.999
28	0.390772	195.386	63	1.04687	523.435
29	0.392209	196.105	64	1.04400	521.999
30	0.393001	196.501			
31	0.393312	196.656			
32	0.393359	196.679			
33	0.393409	196.705			
34	0.393775	196.887			

PUBLICAÇÕES TÉCNICO-CIENTÍFICAS EDITADAS PELO INPE

Teses e Dissertações (TDI)

Teses e Dissertações apresentadas nos Cursos de Pós-Graduação do INPE.

Notas Técnico-Científicas (NTC)

Incluem resultados preliminares de pesquisa, descrição de equipamentos, descrição e ou documentação de programas de computador, descrição de sistemas e experimentos, apresentação de testes, dados, atlas, e documentação de projetos de engenharia.

Propostas e Relatórios de Projetos (PRP)

São propostas de projetos técnico-científicos e relatórios de acompanhamento de projetos, atividades e convênios.

Publicações Seriadas

São os seriados técnico-científicos: boletins, periódicos, anuários e anais de eventos (simpósios e congressos). Constam destas publicações o Internacional Standard Serial Number (ISSN), que é um código único e definitivo para identificação de títulos de seriados.

Pré-publicações (PRE)

Todos os artigos publicados em periódicos, anais e como capítulos de livros.

Manuais Técnicos (MAN)

São publicações de caráter técnico que incluem normas, procedimentos, instruções e orientações.

Relatórios de Pesquisa (RPQ)

Reportam resultados ou progressos de pesquisas tanto de natureza técnica quanto científica, cujo nível seja compatível com o de uma publicação em periódico nacional ou internacional.

Publicações Didáticas (PUD)

Incluem apostilas, notas de aula e manuais didáticos.

Programas de Computador (PDC)

São a seqüência de instruções ou códigos, expressos em uma linguagem de programação compilada ou interpretada, a ser executada por um computador para alcançar um determinado objetivo. Aceitam-se tanto programas fonte quanto os executáveis.